1. Award Information

Award Number: DE-FC36-02ID14427

Project Title: Microchannel Reactor System Design & Demonstration For On-Site H_2O_2 Production by Controlled H_2/O_2 Reaction

Project Period: 09/30/02 – 09/29/07 ***(No-cost Extension to 09/29/08)***

Recipient:
Stevens Institute of Technology
Castle Point on Hudson
Hoboken, NJ 07030
13th Congressional District

Partners:
FMC Corporation
Chemical Products Group
Bldg. 1C-105, US 1 & Plainsboro Road
Princeton, NJ 08543
Emmanuel A. Dada
(609) 951-3847
12th Congressional District

New Jersey Commission on Science & Technology,
Ms. Jennifer W. Posda, Associate Director of R&D Excellence Program
28 West State Street, P.O. Box 83 Trenton, NJ 08625,
(609) 984-1979, jen@scitech.state.nj.us

Environmental Resources Management
Princeton Crossroads, 250 Phillips Blvd., Suite 280
Ewing, NJ 08618
Richard A. Brown
(609) 895-0050
12th Congressional District

Geo-Cleanse International, Inc.
4 Mark Road, Suite C
Kenilworth, NJ 07033
Robert Glaser
(908) 206-1250
7th Congressional District

PanAmerican Enterprises Inc.
304-B Avondale
Houston, TX 77006
William Podorzer
(713) 956-9561

18th Congressional District

Alliance Technologies, LLC, $5,000/yr. (in-kind)
P.O. Box 8 Rt. 1 & Plainsboro Rd.
Princeton, NJ 08543
Jonathan Chun
(609) 951-3145
12th Congressional District

Technical Contact: Adeniyi Lawal (PI, Stevens), (201) 216-8241, alawal@stevens.edu
Woo Lee (Co-PI, Stevens), (201) 216-8307, wlee@stevens.edu
Emmanuel Dada (Co-PI, FMC), (609) 951-3847,
EMMANUEL_DADA@fmc.com

2. No distribution limitations

3. Executive Summary

We successfully demonstrated an innovative hydrogen peroxide (H_2O_2) production concept which involved the development of flame- and explosion-resistant microchannel reactor system for energy efficient, cost-saving, on-site H_2O_2 production. We designed, fabricated, evaluated, and optimized a laboratory-scale microchannel reactor system for controlled direct combination of H_2 and O_2 in all proportions including explosive regime, at a low pressure and a low temperature to produce about 1.5 wt% H_2O_2 as proposed. In the second phase of the program, as a prelude to full-scale commercialization, we demonstrated our H_2O_2 production approach by 'numbering up' the channels in a multi-channel microreactor-based pilot plant to produce 1 kg/h of H_2O_2 at 1.5 wt% as demanded by end-users of the developed technology. To our knowledge, we are the first group to accomplish this significant milestone.

We identified the reaction pathways that comprise the process, and implemented rigorous mechanistic kinetic studies to obtain the kinetics of the three main dominant reactions. We are not aware of any such comprehensive kinetic studies for the direct combination process, either in a microreactor or any other reactor system. We showed that the mass transfer parameter in our microreactor system is several orders of magnitude higher than what obtains in the macroreactor, attesting to the superior performance of microreactor. A one-dimensional reactor model incorporating the kinetics information enabled us to clarify certain important aspects of the chemistry of the direct combination process as detailed in section 5 of this report. Also, through mathematical modeling and simulation using sophisticated and robust commercial software packages, we were able to elucidate the hydrodynamics of the complex multiphase flows that take place in the microchannel. In conjunction with the kinetics information, we were able to validate the experimental data.

If fully implemented across the whole industry as a result of our technology demonstration, our production concept is expected to save >5 trillion Btu/year of steam usage and >3 trillion Btu/year in electric power consumption. Our analysis also indicates >50 % reduction in waste disposal cost and ~10% reduction in feedstock energy. These savings translate to ~30% reduction in overall production and transportation costs for the $1B annual H_2O_2 market.

4. Project Accomplishments

The following are considered the major accomplishments of this project:

- Designed, and evaluated a laboratory microreactor system for controlled, safe direct combination of H_2 and O_2 in various compositions including explosive regime for the production of H_2O_2.
- Development and formulation of in-house catalyst, and rapid screening of different catalysts, both commercial and in-house to identify the right combination of catalyst/support for the direct combination reaction.
- Demonstrated the achievement of extremely fast direct combination reaction with a residence time that is almost two orders of magnitude less than that for microreactors.
- Established theoretically and confirmed experimentally the importance of mixing in H_2O_2 production.
- Determination of optimum process conditions including temperature, pressure, residence time and O_2/H_2 ratio for the direct combination process in a microreactor.
- Production of H_2O_2 in concentrations of significant commercial interest with acid (~1.5 wt%, exceeding the 1 wt% criterion for phase II) and without acid (~1500ppm) at moderate pressure and temperature conditions using our in-house catalyst in particulate form.
- Elucidation of the important reactions in direct combination process and determination of the kinetics of the H_2O_2 synthesis, reduction, and decomposition reactions.
- Modeling and simulation of the flow and mass transfer in microreactor, and determination of the gas to liquid mass transfer parameter.
- Development of an optimized ASPEN model for the production of 1 – 10kg/h of 1.5wt% H_2O_2.
- Design and fabrication of multi-layer and multi-channel microreactor from SS 316L comprising about 500 channels of dimension 800 μm by 800 μm for the pilot-plant unit.
- Demonstrated scale-up from lab set-up to pilot plant at FMC for production of 1.5 wt% H_2O_2 at 1 kg/h.
- Development of closed-channel flow coating, open-channel surface-selective and dip coating methods to deposit sol-gel-based thin-film catalysts into microchannels, and cellular structures.
- Successful infiltration of in-house formulated catalysts into microreactor in thin-film form and evaluation of their activity in thin-film form as well as particulates.
- Determination of residence time distribution in a micromixer.

5. Project Activities

Task 1: Model-based Microchannel Reactor Design

Multiphase reactions in microchannels find applications in many industrially important chemical processes such as the direct synthesis of hydrogen peroxide, hydrogenation of liquid substrates, and immiscible liquid-liquid nitration. The hydrodynamic characteristics of the flow play a very important role in reactor design. Since the flow in a microchannel is typically laminar, the mass transfer between the phases is mainly dominated by diffusion, and turbulent convective flow normally relied upon for rapid and effective mixing in macroreactors is non-existent. Mixing is therefore a critical issue in the design of multiphase microreactors. Many investigators have

characterized gas-liquid flows in a microchannel (Chen et al. 2002, Chung & Kawaji 2004, Triplett et al. 1999, Yang & Shieh 2001, Fukano & Kariyasaki 1993, Coleman & Garimella 1999, Akbar et al. 2003). Bubbly, slug, churn and annular flow are among the observed flow regimes. However, over a wide range of operating conditions, the flow in a multiphase microchannel is typically the so-called Taylor flow regime (Heiszwolf et al. 2001). The Taylor flow is a special case of slug flow where the bullet-shaped bubbles (Taylor bubbles) are separated by free-gas-entrained liquid slugs. The elongated bubble has a characteristic capsular shape with equivalent diameter larger than the channel width. There is a very thin film between the gas bubble and the channel wall. Taylor slug flow has been shown to increase transverse heat and mass transfer compared to single phase laminar flow because of the recirculation within the liquid slugs and the reduction of axial mixing between the liquid slugs (Bercic & Pintar 1997, Kreutzer et al. 2001, Irandoust & Andersson 1989, Thulasidas et al. 1997).

All the results available in the literature indicate that mass transfer, pressure drop and residence time distribution for slug flows in microchannels are highly dependent on the thin liquid film and slug length. Unlike other flow parameters such as superficial velocities and fluid properties, the liquid film thickness and the slug length cannot be determined a priori. Flow visualization, conductivity, or other advanced tomography techniques like magnetic resonance imaging are commonly used to determine these quantities. While the film thickness has been extensively studied experimentally and numerically, there are limited studies on the slug length, an important parameter for Taylor flows. However, there is significant inconsistency in the literature studies, therefore, a systematic study on the gas and liquid slug lengths in microchannels is warranted. As Kreutzer et al. (2005a) pointed out in their review, CFD studies will provide the mechanistic insight for the slug flow in microchannels. Current CFD studies mainly focus on one unit slug cell, which presume that the gas and liquid slug lengths are known. Researchers either used single phase model with void gas (van Baten & Krishna 2004, van Baten & Krishna 2005, Kreutzer et al. 2005b, Irandoust & Andersson 1989a) or implemented two phase VOF model (Taha & Cui 2004, 2006a, 2006b) to investigate bubble shape, bubble velocity, film thickness, mass transfer, pressure drop and velocity profile inside the liquid slug. Some commercial CFD packages such as FLUENT, FIDAP and CFX have proven to be appropriate to perform these studies. The most important objective of this task was to study numerically the gas and liquid slugs for Taylor flow in microchannels. A T-junction microchannel serves as model geometry. The development of the gas and liquid slugs in the geometry with different inlet configurations at various operating and fluid conditions was investigated.

The hydrodynamic characteristics of the flow in microchannels are different from those encountered in ordinarily large-size channels. The threshold of hydraulic channel diameter is about 1mm with fluid properties similar to air and water (Akbar et al. 2003). In microchannels, the buoyancy effect is negligible in comparison to surface tension, which in effect renders the flow characteristic independent of channel orientation with respect to gravity (Triplett et al. 1999). In the studies of chemical reaction in microchannels, a T-junction microreactor with millimeter to submillimeter range is typically chosen to investigate the hydrodynamics or kinetics for multiphase reactions. We consider an empty T-junction microchannel reactor (not packed with catalyst) with cross-sectional width of 0.25, 0.5, 0.75, 1, 2 and 3 mm for the studies of gas-liquid hydrodynamics. This type of reactor is applicable to homogeneous reaction or surface reaction with thin-film catalyst coated on the wall.

Figure 1.1 is the model T-junction microchannel reactor used in our simulation. The microchannel reactor comprises a vertical inlet mixing zone and a horizontal reaction zone. A stream of water and a stream of air are fed separately into the two inlets of the mixing zone, and then enter the reaction zone. The cross-sectional dimensions of the channel are the same, which are represented by d. The mixing zone has a length of 6d while the reactor zone has a length of 60d. "Cold" flow without any chemical reaction is considered. The whole system is maintained at room temperature, and the pressure is atmospheric at the exit. The superficial gas velocity as well as superficial liquid velocity varies from 0.01 to 0.25 m/s. According to the flow regime maps by Chung & Kawaji (2004), Triplett et al. (1999), Yang & Shieh (2001), Fukano & Kariyasaki (1993), Coleman & Garimella (1999) and Akbar et al. (2003), at these operating conditions, the flow falls within the Taylor slug regime in microchannels.

A finite volume based commercial CFD package, FLUENT (Release 6.1.22, 2003), was used to perform the numerical simulations, and typical results are presented in Figs. 1.2 – 1.12. The results show that the slug length is not uniform throughout the channel especially for channel cross-sectional dimensions exceeding 1 mm. When the gas or liquid flow rate increases, the slug non-uniformity becomes more pronounced. The slug length is also highly dependent on the inlet configuration. From the studies of gas and liquid slugs in a T-junction microchannel at various operating conditions, the following conclusions are drawn:

- The gas slug length increases with increase in superficial gas velocity, and decrease in superficial liquid velocity.
- The liquid slug length increases with increase of superficial liquid velocity, and decrease of superficial gas velocity.
- The dimensionless slug length is mainly determined by the phase hold-up, with a slight effect of Re and Ca. Therefore, wider channels have longer slug length at the same superficial gas and liquid velocities.
- Gravitational effects can be ignored in microchannels.
- The effects of fluid density and viscosity are also negligible.
- The surface tension and wall surface adhesion moderately impact the slug lengths.

Based on the equations of conservation of mass and momentum, the associated boundary conditions, and simplifying assumptions, the dimensionless slug length will have the following dependence:

$$L^* = L^*(\mathrm{Re}, Ca, \varepsilon_G) \tag{1.1}$$

Regression of the simulation data provides the following correlations for the dimensionless slug length:

$$(L_G + L_L)/d = 1.637\varepsilon_G^{-0.893}(1-\varepsilon_G)^{-1.05}\,\mathrm{Re}^{-0.075}\,Ca^{-0.0687} \tag{1.2}$$

$$L_G/d = 1.637\varepsilon_G^{0.107}(1-\varepsilon_G)^{-1.05}\,\mathrm{Re}^{-0.075}\,Ca^{-0.0687} \tag{1.3}$$

$$L_L/d = 1.637\varepsilon_G^{-0.893}(1-\varepsilon_G)^{-0.05}\,\mathrm{Re}^{-0.075}\,Ca^{-0.0687} \tag{1.4}$$

A total of 148 sets of numerical simulation data were correlated with channel width 1 mm and less for parameter values in the range: $0.09 < \varepsilon_G < 0.91$, $15 < \mathrm{Re} < 1500$, $0.000278 < Ca < 0.01$.

Eq. (1.3) is obtained by multiplying Eq. (1.2) by ε_G, while Eq. (1.4) is obtained by multiplying Eq. (1.2) by $1-\varepsilon_G$, for $L_G/(L_G+L_L) \approx \varepsilon_G$ and $L_L/(L_G+L_L) \approx 1-\varepsilon_G$ in our simulation conditions. The average difference between the correlated data and the simulated data is about 10%. These correlations show that the dimensionless slug length is mainly determined by the phase hold-up, while the Re and Ca have a slight effect. This result can explain why the dimensionless slug length falls within a narrow range even for wide operating conditions.

These correlations can be used to predict the slug length based on the operating conditions, and subsequently some important transport parameters such as pressure drop, heat transfer and mass transfer coefficients can be estimated. Based on this numerical study of Taylor flow in microchannels, we can begin to understand, and quantify heat and mass transfer enhancement in microchannels. Further details about this activity can be found in Qian and Lawal (2006).

Finally we investigated the two phase flow in a packed bed. In our simulation region, the gas-liquid flow in a microchannel is also a slug flow. This was confirmed by our flow visualization experiments. Figure 1.13 shows the simulation results of the gas and liquid slug lengths in 0.25, 0.50, and 0.75 mm packed bed with 50 micron particles at different void fraction values. Here the gas and liquid velocities were based on real void volume (physical velocity). We can see that as the particles become more densely packed, the slug length decreases.

Notation

d	internal channel width, m
f	apparent friction factor
L	mean slug length, m
t	time, s
U	superficial velocity, m/s
U_{TP}	unit cell velocity ($=U_G+U_L$), m/s
v	velocity, m/s
V_b	gas slug velocity ($\approx U_G+U_L$), m/s

Greek letters

ε	hold-up
μ	molecular viscosity, kg/m s
θ	contact angle, ^{o}
ρ	density, kg/m^3
σ	surface tension, N/m

Dimensionless numbers

Ca	Capillary number ($=\mu U/\sigma$)
Re	Reynolds number ($=\rho Ud/\mu$)

Subscripts & superscripts

G	gas
L	liquid
*	dimensionless value

REFERENCES

Akbar, M.K., Plummer, D. A., Ghiaasiaan, S.M., 2003. On gas-liquid two-phase flow regimes in microchannels. International Journal of Multiphase Flow. 29, 855-865.

Bercic, G., Pintar, A., 1997. The role of gas bubbles and liquid slug lengths on mass transport in the Taylor flow through capillaries, Chemical Engineering Science 52(21/22), 3709-3719.

Chen, W.L., Twu, M.C., Pan, C., 2002. Gas-liquid two-phase flow in micro-channels. International Journal of Multiphase Flow 28, 1235-1247.

Chung, P.M.-Y., Kawaji, M. 2004. The effect of channel diameter on adiabatic two-phases flow characteristics in microchannels. International Journal of Multiphase Flow 30, 735-761.

Coleman, J. W., Garimella S., 1999. Characterization of two-phase flow patterns in small diameter round and rectangular tubes. International Journal of Heat and Mass Transfer 42, 2869-2881.

FLUENT 6.1 documentation, 2003. Fluent Incorporated, Lebanon, New Hampshire.

Heiszwolf, J.J., Kreutzer, M.T., van den Eijnden, M.G., Kapteijn, F., Moulijn, J.A., 2001. Gas-liquid mass transfer of aqueous Taylor flow in monoliths. Catalysis Today 69, 51-55.

Fukano, T., Kariyasaki, A., 1993. Characteristics of gas-liquid two-phase flow in a capillary tube. Nuclear Engineering and Design 141, 59-68.

Irandoust, S. , Andersson, B., 1989. Simulation of flow and mass-transfer in Taylor flow through a capillary. Computers Chemical Engineering 13(4/5), 519-526.

Jensen, K.F., 2001. Microreaction engineering — is small better? Chemical Engineering Science 56, 293-303.

Kreutzer, M.T., Du, P., Heiszwolf, J.J., Kapteijn F., Moulijn J. A., 2001. Mass transfer characteristics of three-phase monolith reactors. Chemical Engineering Science 56, 6015-6023.

Kreutzer, M.T., Kapteijn F., Moulijn J. A., Heiszwolf, J.J., 2005a. Multiphase monolith reactors: Chemical reaction engineering of segmented flow in microchannels. Chemical Engineering Science 60, 5895-5916.

Kreutzer, M.T., Kapteijn F., Moulijn J. A., Kleijn C. R., Heiszwolf J. J. 2005b. Inertial and interfacial effects on pressure drop of Taylor flow in capillaries. AIChE Journal 51(9), 2428-2440.

Qian, D., Lawal, A., 2006 Numerical Study on Gas and Liquid Slugs for Taylor Flow in a T-junction Microchannel. Chemical Engineering Science 61, 7609-7625.

Tata, T., Cui, Z.F., 2004. Hydrodynamics of slug flow inside capillaries. Chemical Engineering Science 59, 1181-1190.

Tata, T., Cui, Z.F., 2006 (a). CFD modelling of slug flow in vertical tubes. Chemical Engineering Science 61 (2006) 676 – 687.

Tata, T., Cui, Z.F., 2006(b).CFD modelling of slug flowinside square capillaries. Chemical Engineering Science 61 (2006) 665 – 675.

Thulasidas, T.C., Abraham, M.A., Cerro, R.L., 1997. Flow patterns in liquid slugs during bubble-train flow inside capillaries. Chemical Engineering Science 52 (17), 2947–2962.

Triplett, K.A., Ghiaasiaan, S.M., Abdel-Khalik, S.I., Sadowski, D.L., 1999. Gas-liquid two-phase flow in microchannels Part I: two-phase flow patterns. 25, 377-394.

Van Baten, J.M., Krishna, R., 2004. CFD simulation of mass transfer from Taylor bubbles rising in circular capillaries. Chemical Engineering Science 59, 2535-2545.

Van Baten, J.M., Krishna, R., 2005. CFD simulation of wall mass transfer for Taylor flow in circular capillaries. Chemical Engineering Science 60, 1117-1126.

Yang, C.-Y., Shieh, C.-C., 2001, Flow pattern of air-water and two-phase R-134a in small circular tubes. International Journal of Multiphase Flow 27, 1163-1177.

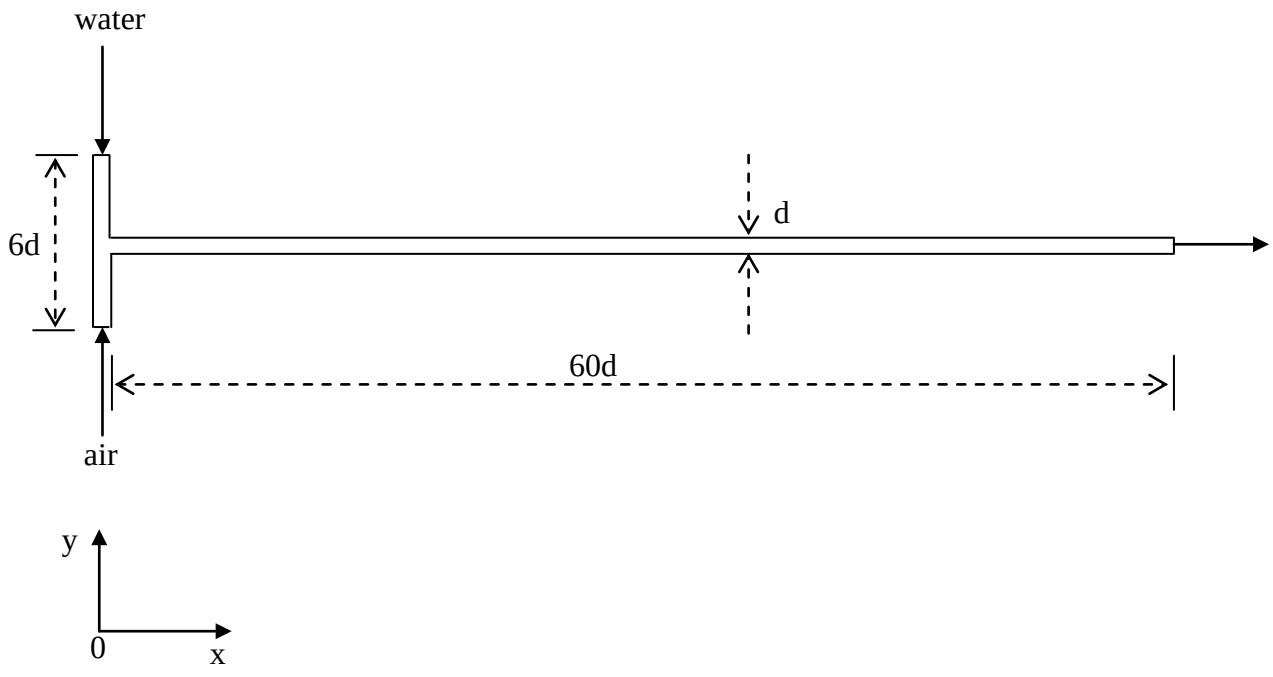

Figure 1.1: Model T-junction microreactor used in the simulation.

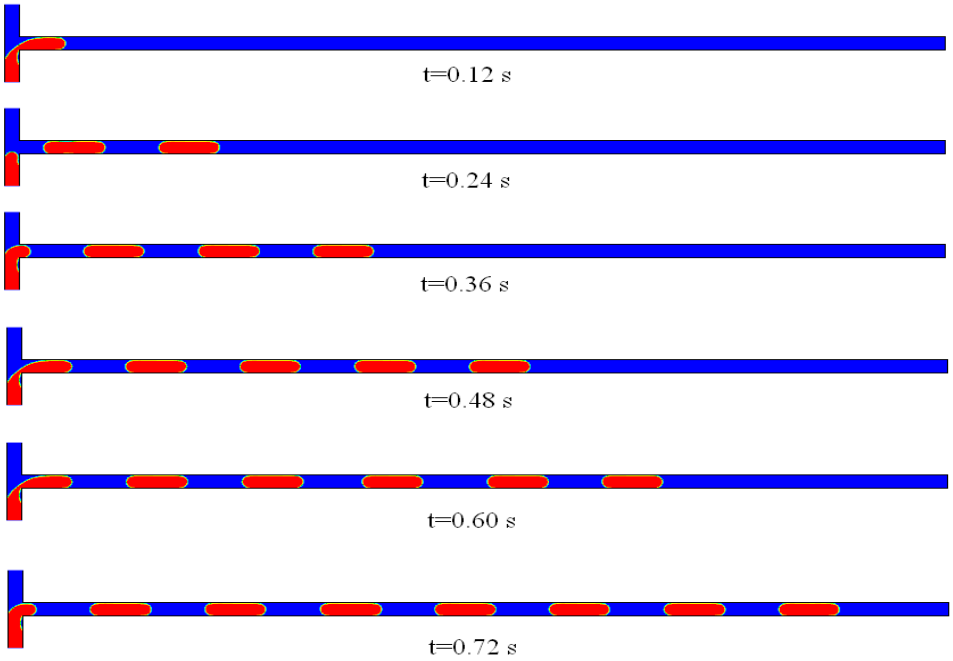

Figure 1.2: Slug flow development in the model geometry. (red —— gas slug, blue —— liquid slug d=0.5 mm, U_G=U_L=0.02 m/s).

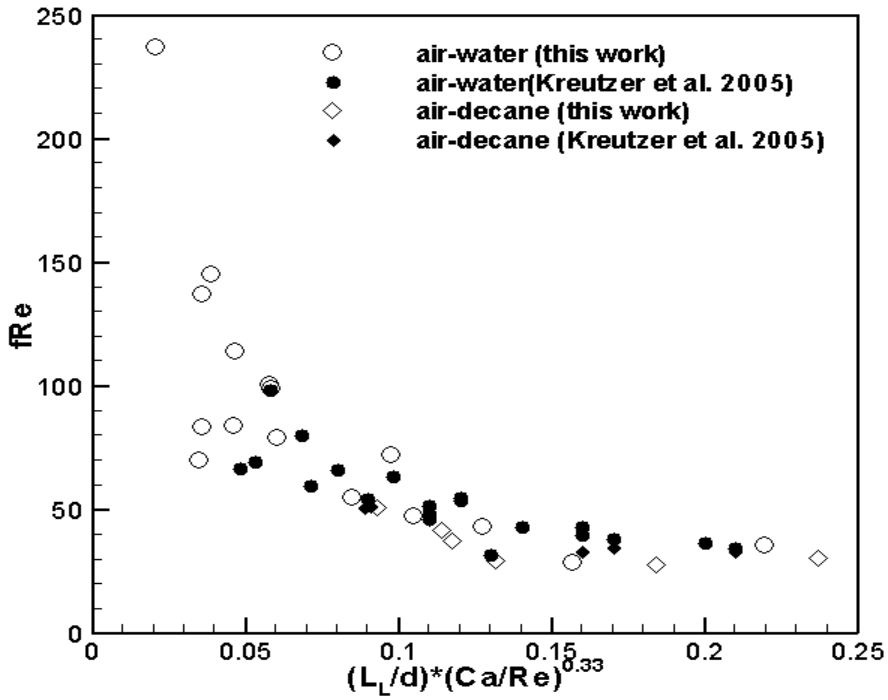

Figure 1.3: (f Re) as a function of the dimensionless group $(L_L/d)*(Ca/Re)^{0.33}$.

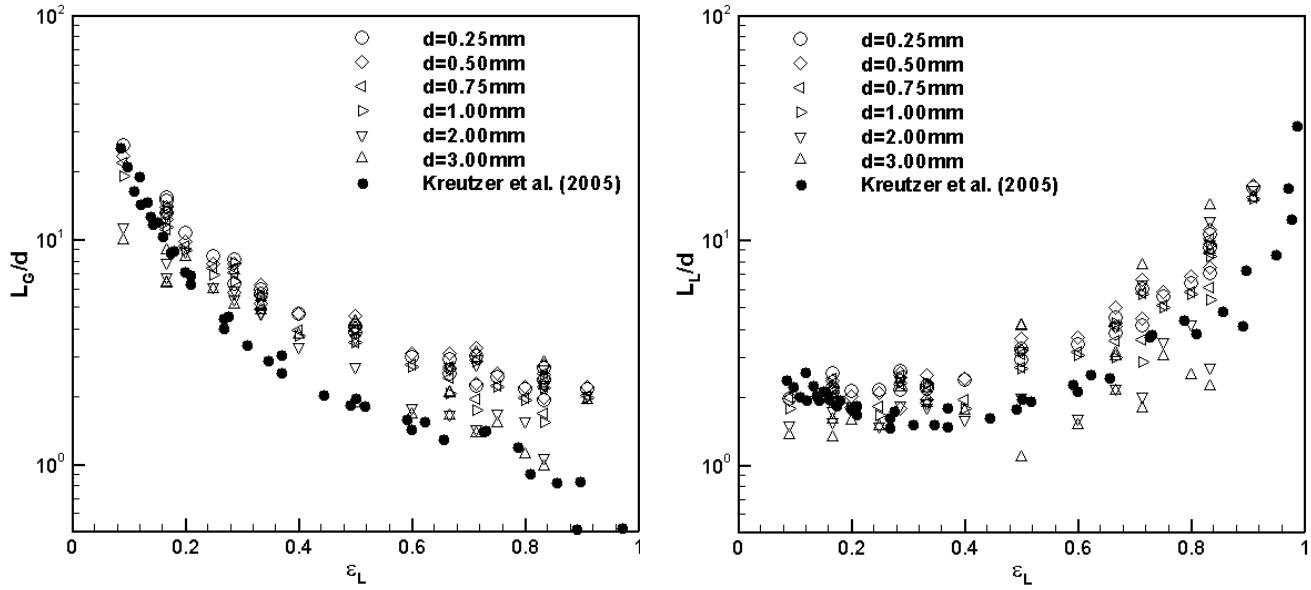

Figure 1.4: Dimensionless slug length against liquid hold-up.

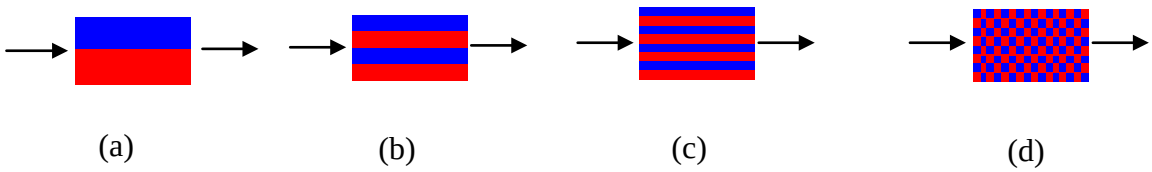

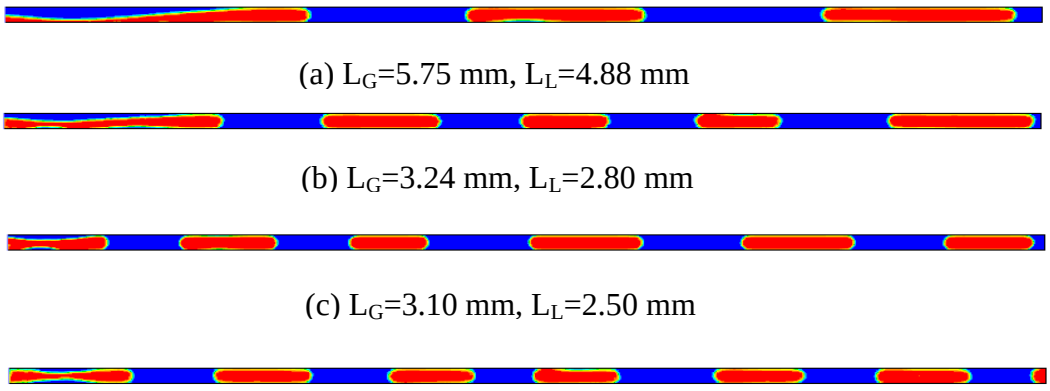

(a) L_G=5.75 mm, L_L=4.88 mm

(b) L_G=3.24 mm, L_L=2.80 mm

(c) L_G=3.10 mm, L_L=2.50 mm

(d) L_G=2.61 mm, L_L=2.11 mm

Figure 1.5: Gas and liquid slugs at different inlet mixing levels. (d= 0.5 mm, U_G=U_L=0.02 m/s)

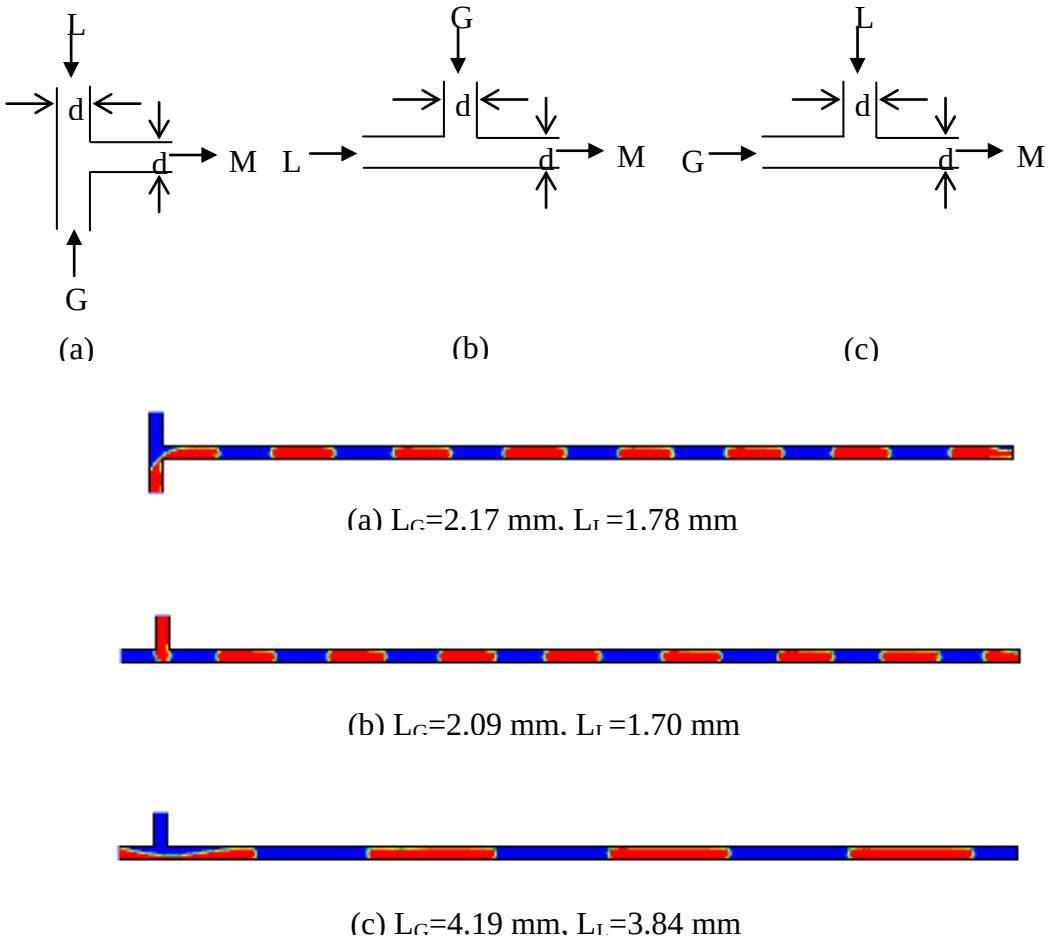

Figure 1.6: Gas and liquid slugs at different tee orientations. (d= 0.5 mm, U_G=U_L=0.02 m/s)

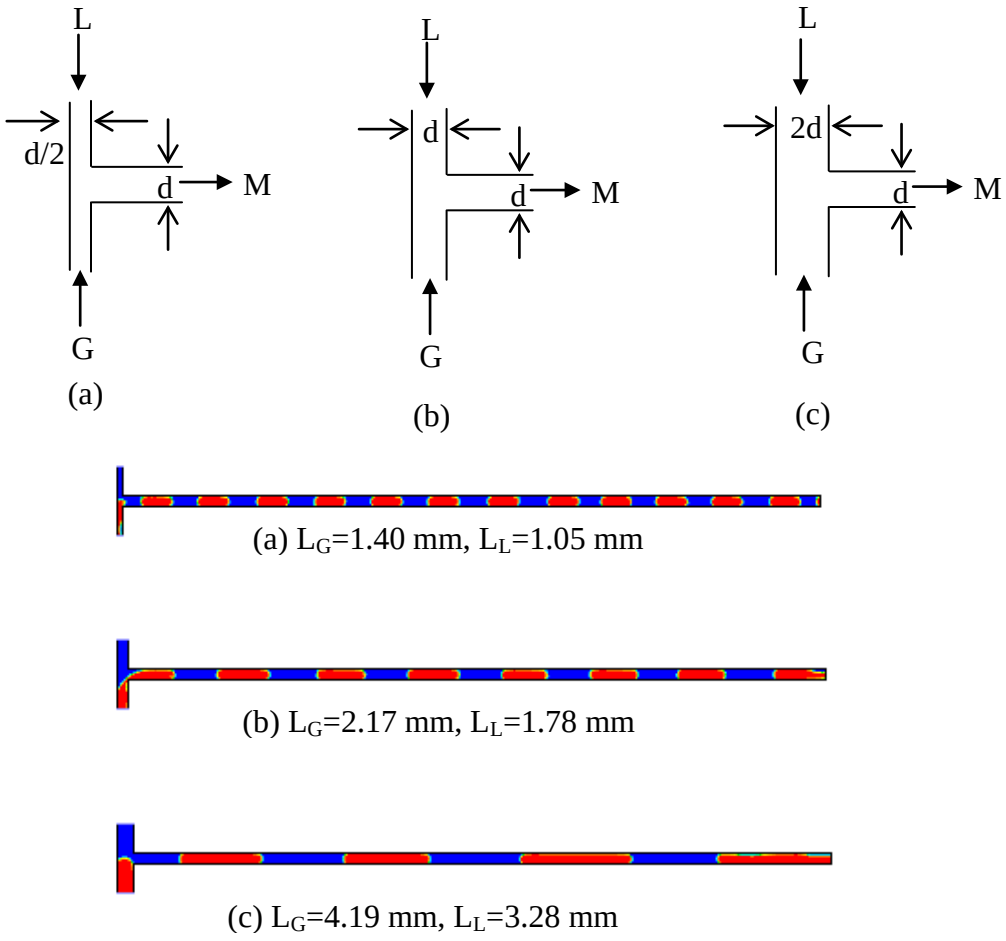

Figure 1.7: Gas and liquid slugs at different inlet tee sizes. (d=0.5mm, U_G=U_L = 0.02 m/s)

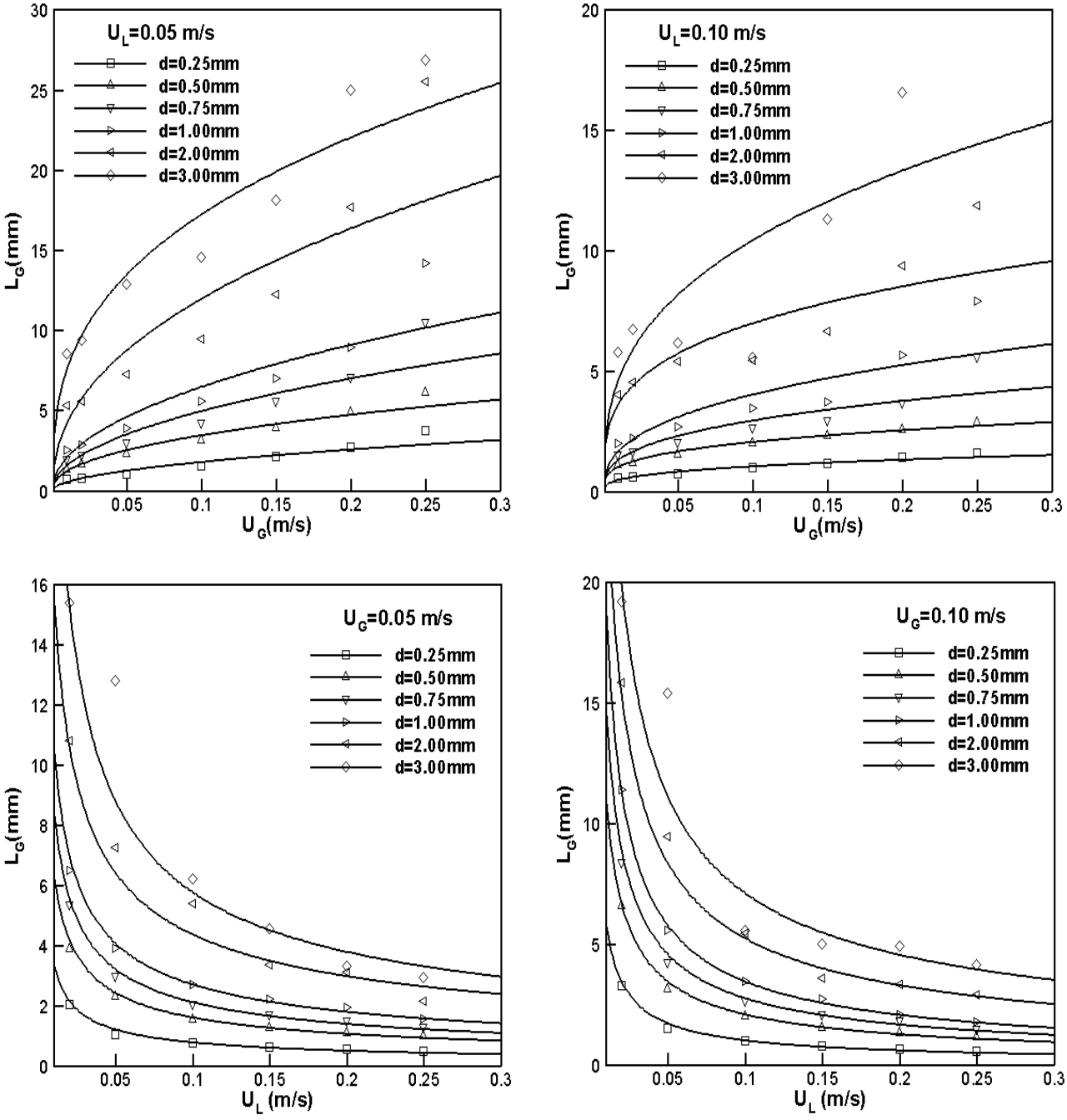

Figure 1.8: Influence of gas and liquid superficial velocities on gas slug length.

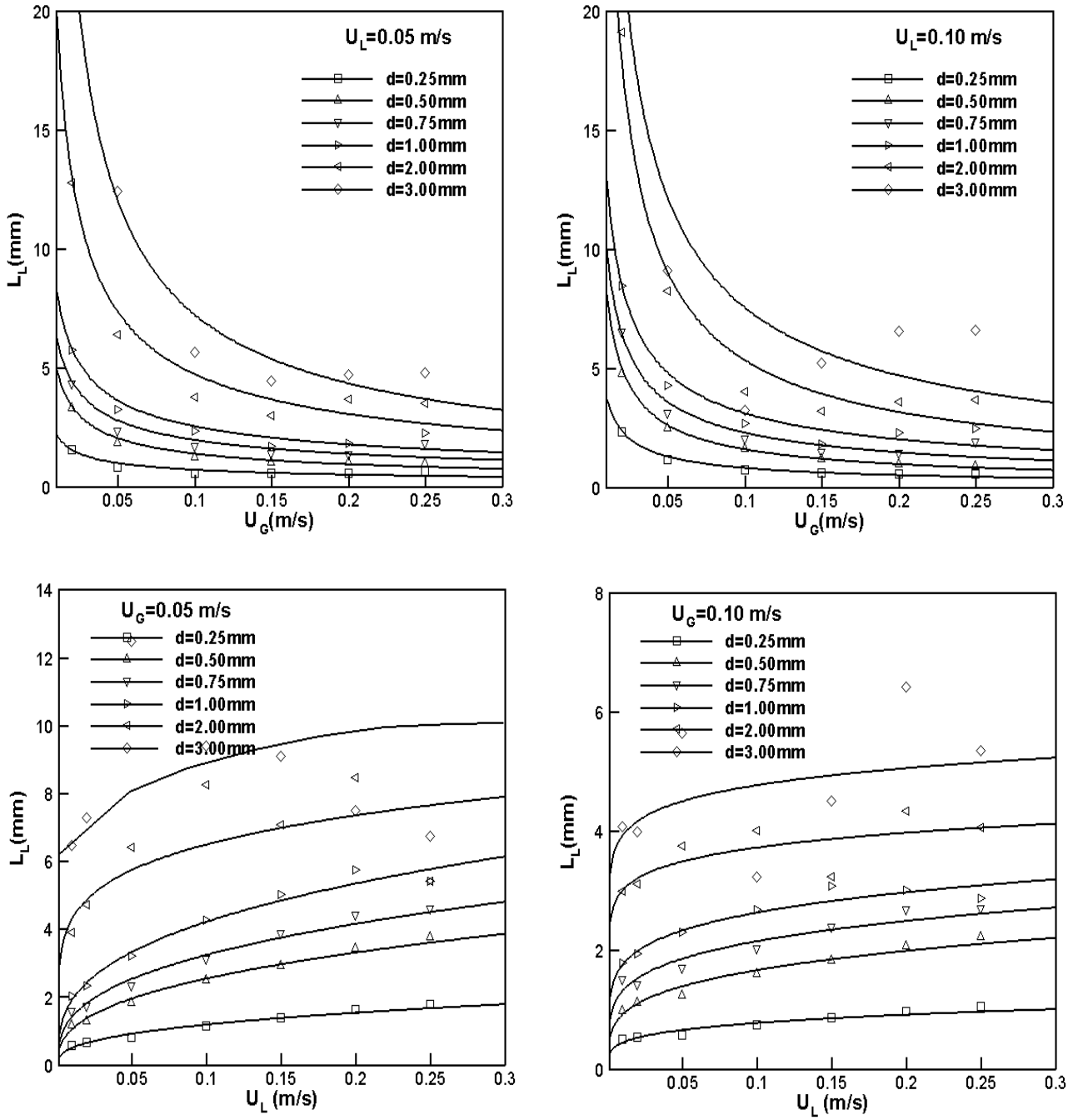

Figure 1.9: Influence of gas and liquid superficial velocities on liquid slug length.

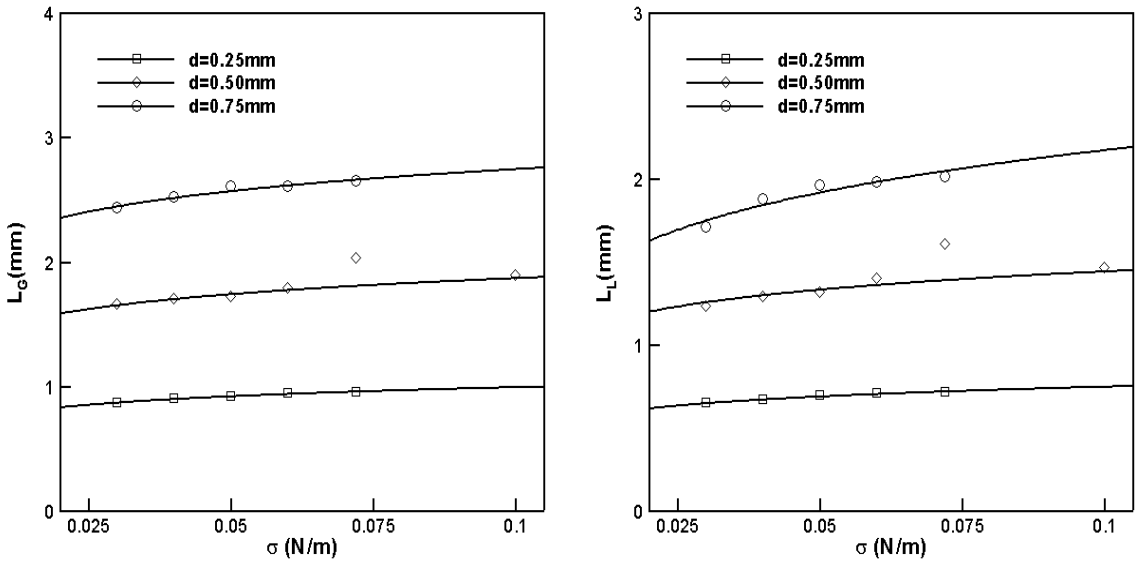

Figure 1.10: Influence of surface tension on gas and liquid slug length. (U_G=0.1 m/s, U_L=0.1 m/s)

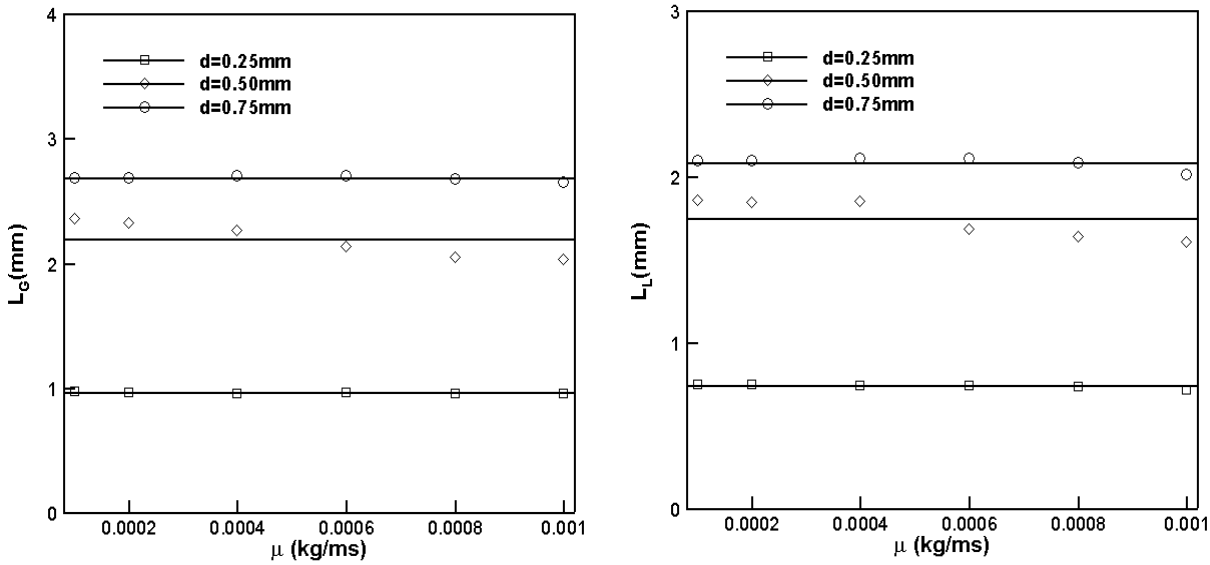

Figure 1.11: Influence of liquid viscosity on gas and liquid slug lengths. (U_G=0.1 m/s, U_L=0.1 m/s)

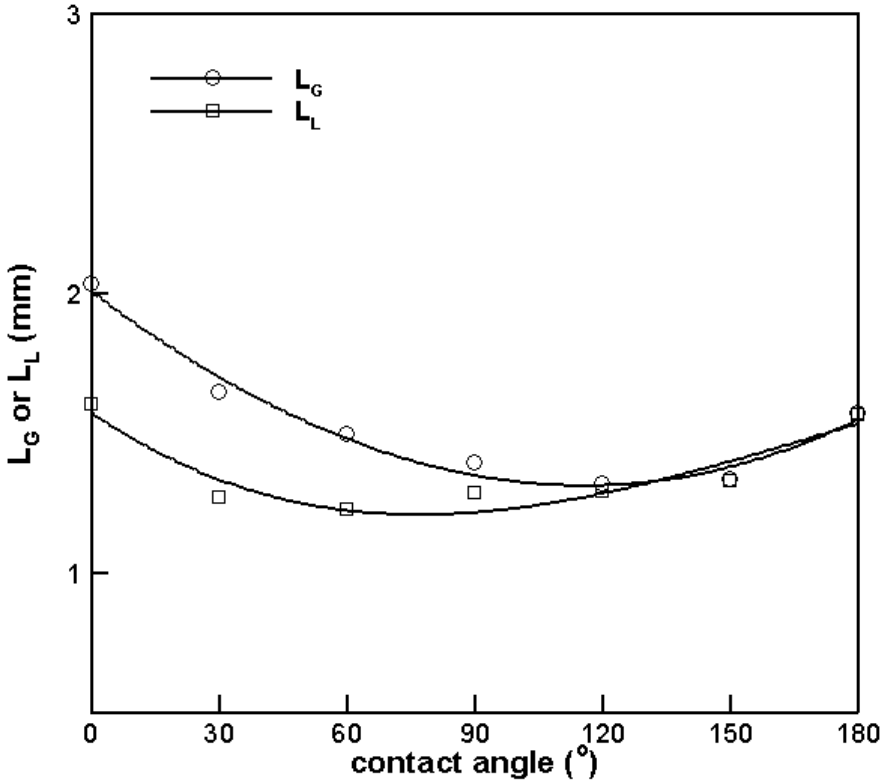

Figure 1.12: Influence of contact angle on gas and liquid slug lengths.
($d=0.50mm$, $U_G=0.1$ m/s, $U_L=0.1$ m/s)

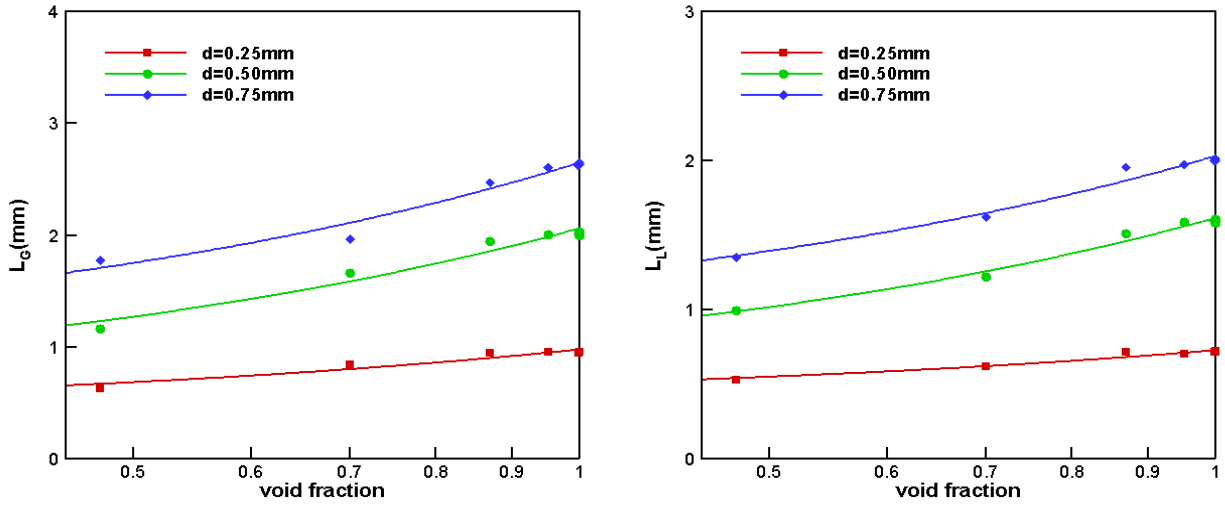

Figure 1.13: Slug length in a bed packed with 50 micron particles at different void fraction
($U_G=0.1$ m/s, $U_L=0.1$ m/s)

TASK 2: Microchannel Reactor Fabrication

The high pressure requirement for the H_2O_2 reaction necessitates the use of metallic reactors. Furthermore, in order to mitigate the decomposition of H_2O_2 once formed, the reactor should be fabricated from high purity SS 316L. To ensure enhanced mixing for the two-phase H_2O_2 reaction, a multichannel micro mixer obtained on loan from Karlsruhe Research Center (KRC) in Germany was combined with the microreactor. As part of the safety consideration in the handling of potentially explosive H_2/O_2 mixtures, the distance between this mixer and the microreactor in the experimental setup was kept to a minimum thereby minimizing the volume of H_2/O_2 mixture that can undergo potentially explosive homogeneous reaction prior to entering the reactor.

Capillary Reactor

Preliminary experimental studies utilized a 400 μm I.D. stainless steel 316L tubing as a model microreactor with microfilters at the entrance and exit of the reactor to prevent the loss of catalyst. However, excessively high pressure drop (> 500 psi) was required for the liquid flow rate of ~ 0.2 ml/min in the packed-bed microreactor. Therefore we decided to replace the reactor with an 800 μm I.D., and the pressure drop reduced significantly to a tolerable level, usually less than 10% of the entrance pressure drop. A lot of the experimental data reported under Task 5 of this report were obtained using this reactor type.

Single Channel T-junction Reactor

We next investigated the possibility of fabricating T-junction metallic reactors. Such a reactor configuration will eliminate the need for the pre-mixing of the reactant mixture and the solvent prior to entering the reactor. There are various technologies available for this purpose, including laser machining, chemical wet etching, electrodischarge machining (EDM), focused-ion beam, and mechanical milling. Of all these methods, mechanical milling seemed to be the most cost-effective while at the same time providing the machining precision needed for modeling and experimental studies. 10 T-junction microreactors were fabricated for us from Stainless Steel 316L using micromilling. The cross-sectional dimensions of the channel are 500 x 500μm. The length of the horizontal section is 11 mm while the vertical section is 60 mm long (Figure 2.1). This reactor configuration was more suited for conducting experiments in the H_2/O_2 explosive regime than the capillary reactor that we had used up to that point, since mixing of the two reactants did not occur until they were about to contact the catalyst. Another advantage of this reactor in comparison with the capillary reactor is that it enabled us to examine the state of the catalyst without disturbance after prolonged use in the reactor.

To provide adequate sealing under high pressure environment, a gasket was placed between the reactor cover plate and the bottom piece. Two types of gasket material were tried, namely PTFE and silicone, both of 250μm thickness. The PTFE gasket was relatively hard and could not provide adequate sealing at high pressure. The softer silicone gasket buckled into the channel under compression, blocking the flow. The silicone gasket was thus discarded, and replaced by the PTFE gasket. In order to eliminate the leakage at high pressure, it was decided to use more screws for proper tightening. Thus, sixteen more screw holes (eight on each side) were made on the reactor and the cover plate in addition to the original twelve screw holes. The 28 screws along with the PTFE gasket provided effective seal, even at high pressures.

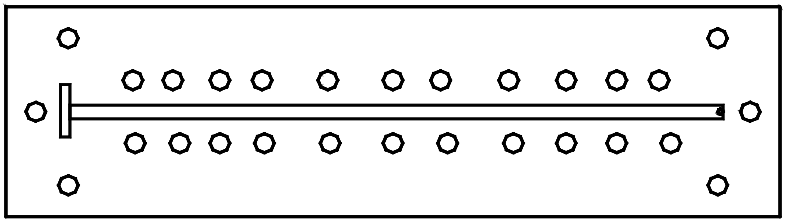

Figure 2.1: Reactor configuration with 28 screw holes

A catalyst bed retainer was placed at the end of the reactor, and the reactor was experimentally tested for three consecutive days with 0.10 ml/min of water and 10 sccm of N_2 flowing through it. The pressure drop was low (20-25 psi), and remained steady throughout the test period.

Multi-channel High Throughput Reactor

Our generic multi-channel high throughput reactor design concept is illustrated in Figure 2.2. The concept is based on a rectangular-shaped reactor block with alternating layers of reaction channels (orange) and cooling channels (blue) (Figure 2.2(a)). The block will house a matrix of parallel flow channels in which the direct combination reaction takes place, and a second matrix of parallel flow channels for the provision of cooling to the reaction channels. The main reaction is slightly exothermic, so cooling channels are needed to remove the heat of reaction in order to maintain approximately an isothermal condition. These channels will be layered in such a way that the reaction channels and their adjacent cooling channels are in close contact for effective heat transfer. The reaction and cooling channels are arranged in a cross-flow configuration which will enable incorporation of manifold design (Figure 2.2(b)).

The catalyst will be placed in the reaction channels, while cooling water will be circulated in the empty cooling channels. Typical dimensions for the reaction and cooling channels are given in Figure 2.2(c). The cross-sectional dimensions of the channels are 500 x 500 μm with 300 μm solid wall in between channels. All the channels will be fabricated from 1 mm thick metal plates. For the entire block, there are 175 channels in each plate with a total of 35 plate layers to be stacked in the vertical direction. Based on our experimental data, these number of reaction channels on this block will produce approximately 10 kg/hr of 1.5 wt% H_2O_2.

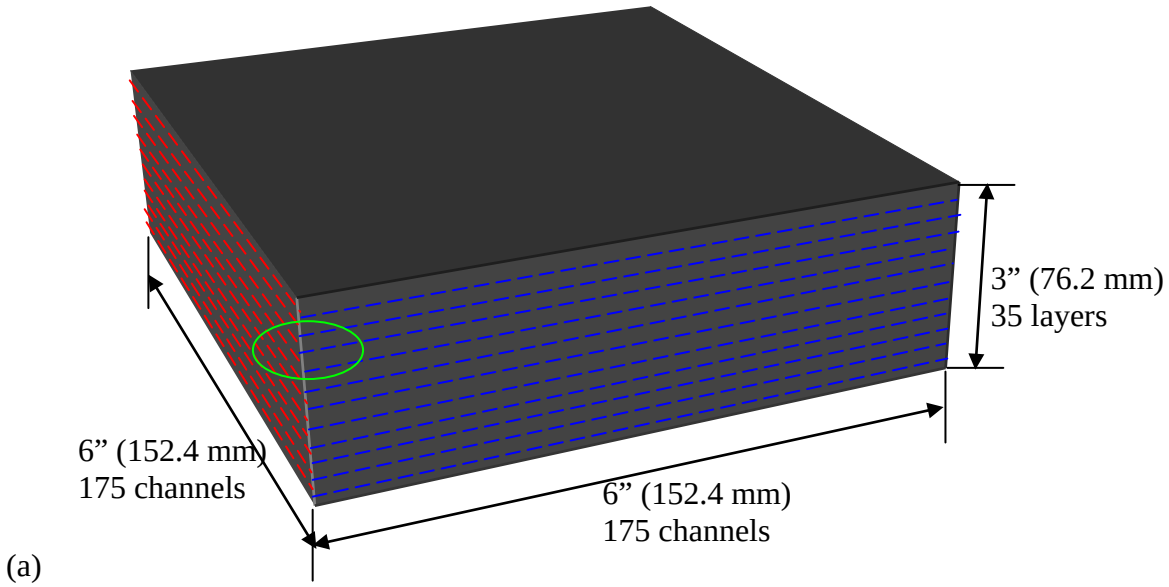

(a)

(b)

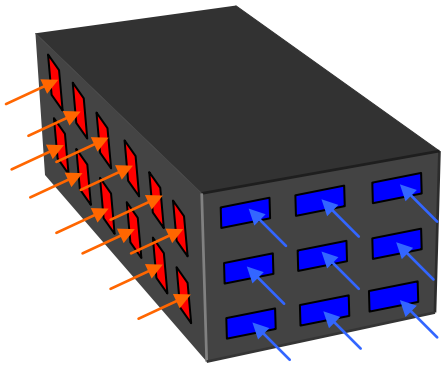

(c)

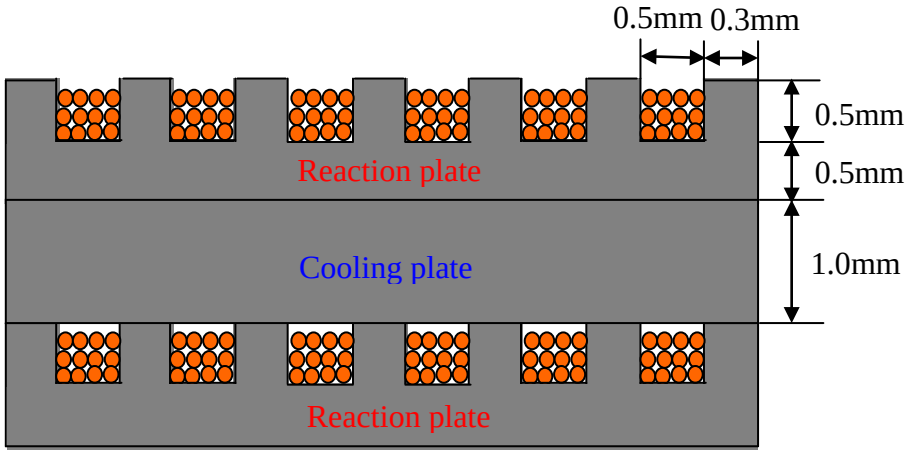

Figure 2.2c: H_2O_2 micro-reactor stack integrated with heat exchanger (a) H_2O_2 reactor block layout (b) Flow arrangements (c) Typical dimensions

In the proposed design, a thin layer (25 – 50 µm) of glass would be used to bond the metal plates in which the microchannels are etched. The metal surface will be treated with Ni to allow the glass to bond strongly to the metal. Special glass patented by Sarnoff, (an industrial partner brought into the project by FMC) would be used that could withstand stacking temperature of approximately 500^{o}C, the maximum temperature that the catalyst could withstand without performance degradation. Stacking of metal plates was considered cheaper than stacking of silicon plates, and glass bonding would account for about 95% of the cost of prototype reactor manufacture. The catalyst may be packed or deposited into the reactor before or after stacking, however for cellular structure catalyst, it must be inserted into the reactor before stacking.

The fabrication of the prototype reactor posed a number of challenges including: (1) bonding the reactor plates together using glass/NiO, (2) assembling the three pieces together, namely the entrance manifold, reactor/heat exchanger, and exit manifold while achieving perfect fluid seal at moderate/high pressures, (3) aligning the reactor/heat exchanger plates, and (4) Mechanical Milling/EDM of the channels to ensure low tolerance of 2 – 5 %.

The material of construction of the reactor was also considered to be crucial. While 316SS L was a strong candidate, the research team felt that other materials of construction should be investigated. The material of choice should have (i) high mechanical strength to withstand heat up during multi-layer stacking procedure, (ii) thermal coefficient of expansion compatible with

glass that would be used to bond the reactors together, and (iii) chemical compatibility with H_2O_2 product (minimal decomposition, corrosion, and excellent stability in presence of sulfuric acid that may be added during production). Different materials of construction were considered, the properties and attributes of which are presented in Table 2.1.

In terms of ease of bonding of the different reactor plates, titanium seems to be the best material. However, under the processing conditions used in the laboratory reactor, titanium could exhibit low but finite corrosion rates (of about 2 - 5 mils per year [50-125 µm per year]). For a prototype reactor, corrosion rates of this magnitude would be acceptable as the reactor will not be run continuously. However, such low corrosion rates could still be significant for long-term service, considering the fact that the reactor channel/channel wall dimensions are only 200 – 500 µm thick. Ideally, for such dimensions, corrosion rates should be near zero. Glass, ceramics such as alumina, and noble metals may be the only materials with near-zero corrosion rates. Titanium is not known to form pyrophoric compounds in the reactor environment.

Table 2.1: Materials for reactor fabrication and their properties

Material	**Density**	**Weight**	**Coefficient of thermal expansion**	**Thermal conductivity**	**Corrosion resistance**	**Ease of fabrication**	**Cost**
	(gm/cc)	(in lbs)	µin/in-°F	BTU-in/hr-ft²-°F		[1(easy) - 5(difficult)]	[1(lo) - 5(hi)]
Stainless steel - 316L	8.03	0.29	9.2	101	good	3	1
Allegheny Ludlum - AL 42	8.15	0.29	2.2 - 2.6		fair-poor	2	2
Carpenter controlled expn alloys - Glass sealing 42 alloy	8.12	0.29	2.3-2.6	104	fair-poor	2	2
Alumina	3.9	0.14	4.5	174	excellent	5	5
Titanium - Grade 2	4.5	0.16	4.8	114	good	2	1-2
Hastelloy C276	8.9	0.32	6.2	68	excellent	2	3
Alloy 20-Cb-3	8.08	0.29	8.2	85	excellent		2
Aluminum 1100	2.7	0.10	13.1	1540	good		1

The group selected titanium for the material of construction of the prototype reactor based on many factors including its properties, Sarnoff's extensive working experience with titanium, and the need to minimize problems at the planning stage. Since this activity dovetailed into the Phase 2 of the project, further discussion follows under Task 7 below.

Task 3: Microchannel Reactor Studies for Model Validation

In this activity, commercial software packages such as Fluent, Gambit, ANSYS, and Pro/Engineer were used for mixer/reactor design, mesh generation, optimization, and characterization. Fluent, a computational fluid dynamics (CFD) software package, was selected for flow/mixing simulations instead of ANSYS (another CFD software package) because of its capability to handle both single-phase and multi-phase flows, its versatility and user-friendliness. Two commercial software packages selected for solid modeling and mesh generation were Pro/Engineer and Gambit, both of which can be interphased with the CFD packages. Using the above modeling and simulation tools, ***a mixing analysis was undertaken on five different geometrical configurations to determine the geometry that will provide the best mass transfer characteristics for single-phase/multiphase flows while minimizing pressure drop.*** One of the five configurations studied was the standard T-junction Micromixer (TjM). The other four were proposed configurations, a Multilaminated T-junction Micromixer (a multiple-inlet version of the TjM), and three Multilaminated/Elongational Flow Micromixers (MEFMs).

Preliminary theoretical mixing analysis conducted by studying the mass diffusion of gases, and liquids through different microchannel mixer/reactor configurations indicated that the proposed MEFMs are superior to the standard T-junction mixer. Of the three variants of the MEFMs investigated, the most promising one, based on the preliminary simulation study was identified and later evaluated in greater detail along with the standard T-junction mixer using as criteria, high mixing quality with minimum pressure drop. We herein refer to the "best" MEFM as MEFM-4 since the mixing elements, placed on this mixer channel floor for fluid stretching as well as local re-orientation of fluid interfaces, are four-sided/trapezoidal structures (see Fig. 3.1a). For the mixing study on this configuration, two liquid species, water and methanol were introduced alternately at the inlets, and the mass fraction of water in the exiting streams was obtained. When equal flow rates of water and methanol are introduced at the inlets of this multiple-exit configuration, the closer the value of the mass fraction of each species in each exiting stream to 0.5, the better the mixing quality (see Fig. 3.1b). Another measure of mixing, the residence time distribution (RTD) function, was used to confirm numerically the results of the first measure, i.e., species mass fraction distribution (SMFD) of chemical species.

The mixing effectiveness in a standard T-junction micromixer was studied by introducing two test liquids/solutions into the mixing unit and capturing the images of mixing regions of interest using a fluorescence microscope. The captured images were then analyzed using image processing tools. A fluorescence microscope (Nikon Eclipse E1000) fitted with a digital CCD camera (Cooke SensiCam QE) was used to capture the images of the flow behavior/color change of two liquid streams in the mixing regions of interest. A dual syringe pump (obtained from KD Scientific) with two 10-mL syringes was employed to deliver equal flow rates of two liquid streams via the two inlet ports into the mixing unit. This mixing unit connected to fluidic accessories was suitably placed on the microscope stage as shown in the experimental set-up (see Fig. 3.2). The goal of the activity was to investigate **experimentally** mass transfer effectiveness of currently utilized as well as proposed mixing configurations. If the experimental data agree qualitatively with numerical predictions, then the CFD code (Fluent) in conjunction with the two mechanistic measures, (species mass fraction distribution, and RTD – earlier-mentioned) can be used as a predictive tool in the design, evaluation, and optimization of micromixers.

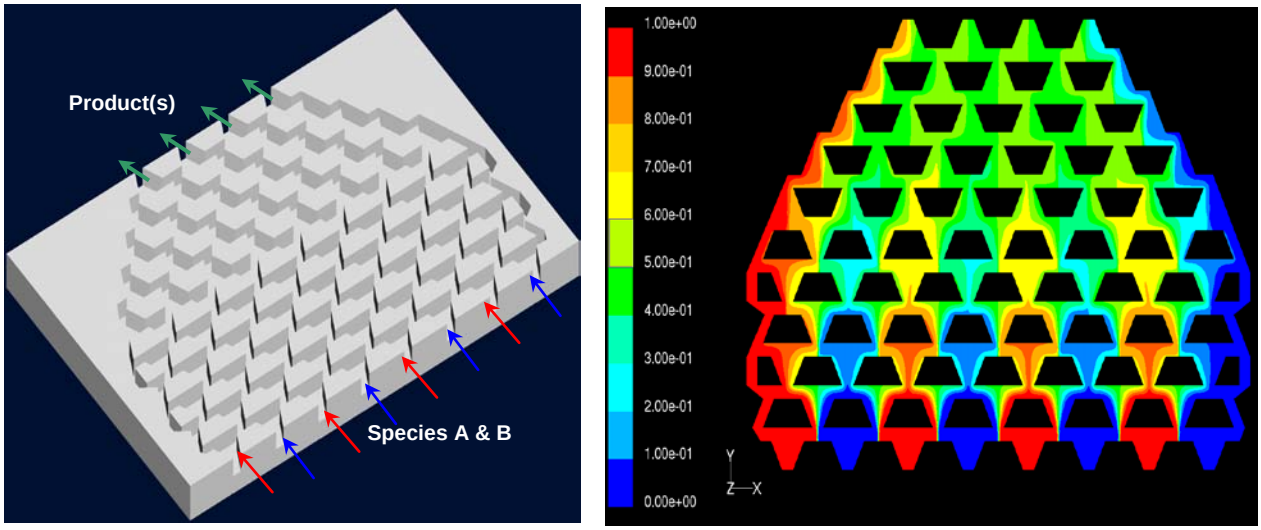

(a) (b)

Figure 3.1: The MEFM-4 showing: (a) the solid model (channel depth is 200 μm and smallest flow domain dimension is 100μm) and (b) the contour plot for the mass fraction of water in water/methanol mixture.

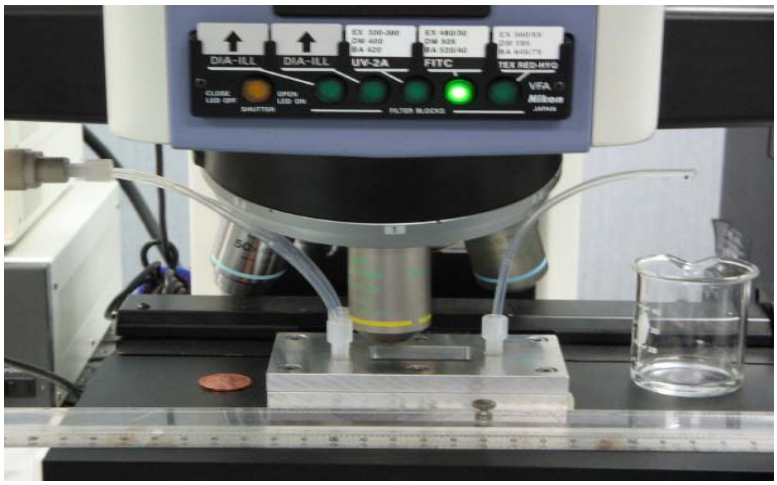

Figure 3.2: Experimental set-up for flow/mixing visualization and imaging.

The mixing behavior of miscible and immiscible liquids was probed in a T-junction mixer (fabricated from glass by Mikroglas®) by monitoring the color/intensity variations of a fluorescent dye (uranine) along its mixing length using the experimental set-up in Fig. 3.2. The two test solutions used for this study were: pure methanol and 0.1mM aqueous solution of uranine (miscible liquids) and pure toluene and 0.1mM aqueous solution of uranine (immiscible liquids). Under well-optimized experimental conditions, each of the liquid streams was injected at a volume flow rate of 0.2 mL/min using a dual syringe pump. The images were captured (after a flow time of 15 minutes) in this micromixer (with a channel width of 450 microns) at a mixing region of interest (see Fig. 3.3) using a high-performance 12-bit CCD camera, and were analyzed using Image Plus^{TM} software. The plots of the fluorescence intensity of uranine against the channel width (at an axial distance of about 15 mm from the T-junction) for the two cases of

experiments (see Fig 3.4) show the expected result: close-to-flat fluorescence intensity profile for the case of contacting methanol and aqueous solution of uranine and two distinct flat profiles of two segregated regions (bright and dark portions) when toluene and aqueous solution of uranine were contacted.

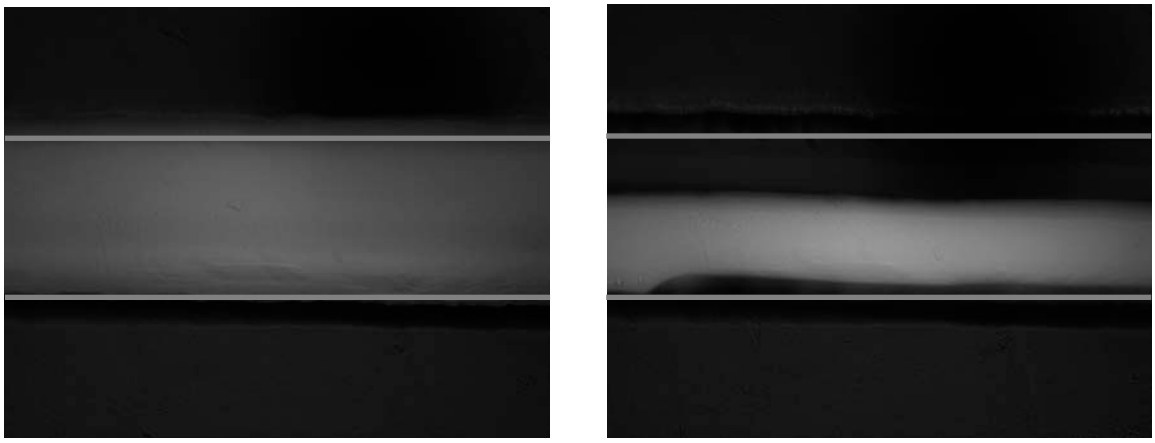

(a) (b)

Figure 3.3: Captured images of: (a) methanol/water mixture and (b) toluene/water mixture.

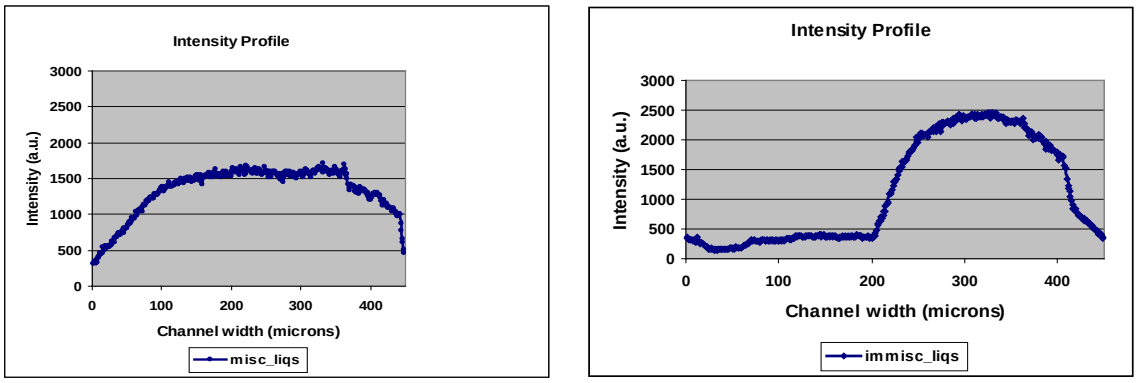

(a) (b)

Figure 3.4: Intensity profiles for: (a) methanol/water mixture and (b) toluene/water mixture.

The results of contacting miscible and immiscible liquids show as anticipated that the T-junction mixer, though a relatively simple configuration for mixing, might not be as effective as the proposed multilaminated/elongational flow micromixers (MEFMs) in achieving mixing, especially for multi-phase flow systems.

The mixing performance of the T-junction mixer was further investigated by focusing on the mixing behavior of miscible liquids *only* at four different axial locations along the mixing length of the mixer. In this part of the experiment, pure methanol and 0.2mM aqueous solution of uranine were used as the test miscible solutions. Each of the two liquid streams was injected into the mixer at a volume flow rate of 0.2 mL/min using a dual syringe pump. The color/intensity variations of uranine molecules in the mixture were then monitored at distances of 2.0, 2.5, 3.0, and 3.5 cm along the T-junction mixer's mixing length of 5.6 cm. The fluorescence images were captured at these locations using a high-performance 12-bit CCD camera, and were analyzed using Image-Pro Plus^{TM} software. The degree of mixing in the micromixers was evaluated by

considering the uniformity of intensity of the fluorescent molecules in the captured images at the four axial locations of interest. The result shows that the uniformity of intensity of uranine increases (i.e. the coefficient of variation decreases) with the axial location downstream (see Fig. 3.5), implying that mixing improves with mixing length (or residence time) as expected.

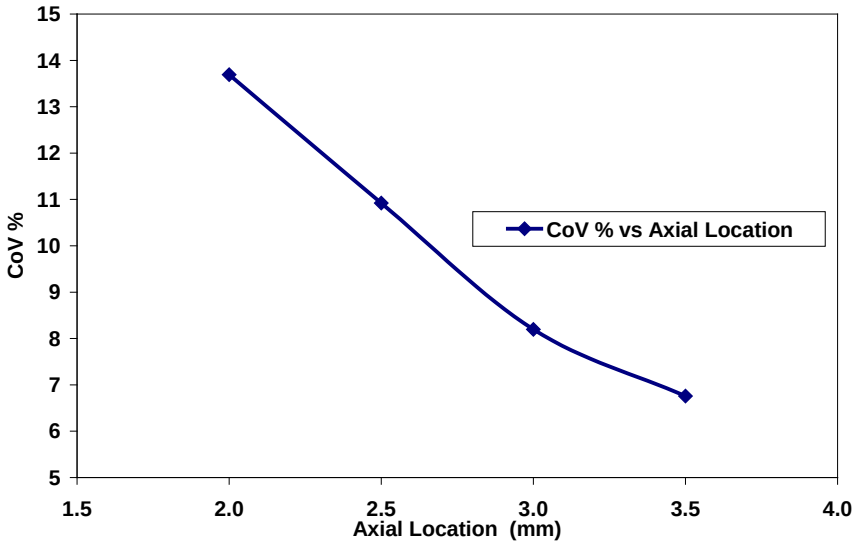

Figure 3.5: The plot of CoV (a measure of uranine intensity uniformity) vs. axial location.

The next experiments included the characterization of mixing in the proposed multilaminated/elongational flow micromixers (MEFMs) along with the standard T-junction mixer, using residence time distribution (RTD) – a more quantitative mixing measure compared to flow visualization. To this effect, while plans were underway to fabricate one of the MEFMs (i.e. MEFM-4) and the T-junction mixer utilizing the fabrication tools at Cornell Nanoscale Science & Technology Facility (CNF), the design and setting up of the experiment for the mixing characterization in micromixers using the RTD was going on concurrently. The T-junction microchannel mixer fabricated from glass by Mikroglas was used to perform the so-called 'absorbance and time acquisition' or tracer experiments. The schematic diagram of our experimental set-up is shown in Fig. 3.6. The set-up enables the determination of the RTD data needed to characterize mixing devices. The description of this experimental set-up along with the procedure is given below. A syringe pump with two 10-mL syringes was used to deliver constant and equal flow rates of pure liquid streams (such as water) via the two inlet ports into the mixing unit. Using a precise 4-port micro-volume sample injector (from Valco Instruments Co. Inc.), a small amount (e.g. 0.5 µl or 1 µl) of a tracer dye (such as uranine) was then introduced as a step or pulse input into the steady state flow of the pure-liquid-system. The detection system used was a miniature PC2000 PC Plug-in Spectrometer (from Ocean Optics Inc.) with a multichannel capacity, i.e. one master and one slave configuration for simultaneous detection and measurement of the tracer absorbance at both the inlet and outlet of the mixing device. The light source, sampling regions and the detection system were connected with one another, and integrated using 400-micron diameter optical fibers. The spectral data obtained as a function of time using the Ocean Optics' OOIBase32 spectrometer operating software were then analyzed. From these absorbance values, the concentration data were generated, and hence the RTD. Out of the two commonly used tracer injection techniques for obtaining the RTD in a mixer or

reactor namely, the step input-response and pulse input-response, the former method was firstly used since it is relatively easier to carry out experimentally than the latter. One of the technical challenges posed by the tracer experiments in obtaining reliable spectral data was the entrapment of air bubbles inside the microchannel flow/mixing system. This issue was resolved by ensuring that all the fluid-connector interfaces were tight-fitted, and the processing liquids bubble-free.

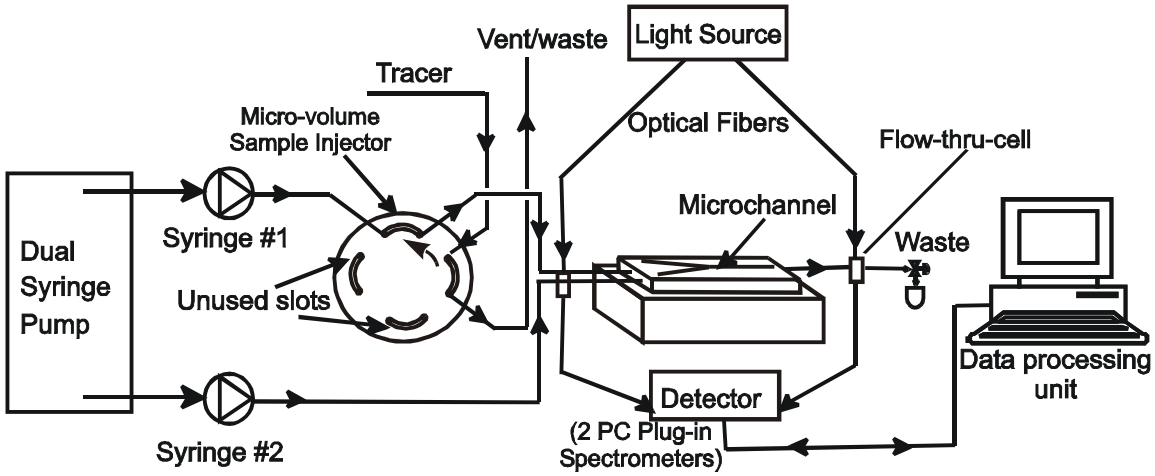

Figure 3.6: The schematic diagram for RTD determination in a micromixer/reactor.

In the step tracer experiments carried out, a syringe pump with two 10-mL syringes was employed to deliver a constant liquid flow rate of 0.25 mL/min from each syringe into the mixing unit via two inlet ports. After maintaining a continuous, steady state flow inside the mixing system by flowing 4mL of water from each syringe, one of these syringes was replaced by a syringe filled with 6mL solution of the tracer dye, uranine (fluorescein sodium). Using the two PC2000 PC Plug-in Spectrometers, the simultaneous detection and measurement of uranine absorbance at both the inlet and outlet regions of the mixing device were made possible. At a time, say t = 0s, the software data acquisition and the injection of the uranine solution and deionized water at a flow rate of 0.25 mL/min were simultaneously initiated. Based on Beer-Lamberts Law of absorption spectroscopy, calibration curves were obtained by using 5.0, 10.0, 15.0, and 20.0-ppm uranine solutions for the step tracer experiments. The consistency and the linearity of the calibration curves (results not shown) for the two sampling regions showed that the concentrations at which these experiments were performed were within the linear response range for these spectrophotometers.

The analysis of the concentration data to obtain true RTD of mixers generally poses a technical challenge because it is difficult experimentally to obtain the desired *perfect* step or pulse injection of tracer, and also exclude the effects of the peripheral components from the measured *cumulative* output signal. Therefore, this data analysis was performed with the aim of mitigating the effects of imperfect pulse or step input of tracer in obtaining the RTD of micromixers. A mathematical approach based on Convolution Integral theorem (Levenspiel,

1972) was found quite useful in achieving the goal of our data analysis. According to this theorem, a relationship between the time–dependent output tracer concentration from a mixing unit and the input concentration exists and is given by the convolution integral:

$$C_{out}(t) = \int_0^t C_{in}(t - t')E(t')dt'$$

where $C_{out}(t)$ = predicted outlet concentration of the tracer at a particular time t
$C_{in}(t - t')$ = measured inlet concentration of the tracer at a time $(t - t')$, and
$E(t')$ = residence time distribution (RTD) function

Applying the numerical version of the convolution integral, the measured output concentration data were mathematically fitted with the convolution product of the input concentration data and a suitable model for RTD function. This type of fitting allows for the estimation of the model parameters from which the RTD of the mixer can be obtained. In this convolution-deconvolution technique, the RTD function based on dispersion model was used because it is generally known to approximate quite well the dispersion/mixing behavior in real mixers/reactors. In order to solve the convolution and the associated model-fitting problem for usually large concentration data points (~ 1000) acquired from tracer experiments, a code was written and implemented using programming functions available in Mathematica® v5.2 (Wolfram Research) software.

The time-dependent absorbance/concentration data were obtained for the step injection of 20 ppm uranine into a steady state flow of water at three different volumetric flow rates, i.e., 0.125, 0.250, and 0.500 mL/min. The analysis of the concentration data and the subsequent model fitting of the data allowed for the estimation of the model parameters (mean residence time, τ, and Peclet number, Pe) from which the RTDs of the mixer were obtained. For a particular set of concentration data at these flow conditions, the values obtained for the model parameters were: τ = 25.95s and Pe = 8.83 (at 0.125 mL/min); τ = 10.89s and Pe = 4.36 (at 0.250 mL/min); and τ = 3.21 and Pe = 1.78 (at 0.500 mL/min). The results indicated that as the flow rate increased, the Pe (= uL/D_z) decreased. Since the characteristic velocity u, increases with increase in flow rate, for a fixed L, a decrease in Pe implies an increase in the coefficient of dispersion (D_z), which provides for better mixing in the T-junction micromixer. The above result shows that the higher the flow rate in the T-junction micromixer, the narrower is the RTD, the smaller the variance of the distribution, and the better the mixing performance.

The fabrication and the packaging of both the standard TjM and our proposed MEFM-4 were successfully completed using the state-of-the-art facilities at Cornell Nanofabrication Facility (CNF) and Applied Microengineering Ltd (AML). It is worth noting that suitable manifolds were designed for the uniform flow distribution of fluids in the channels of MEFM-4 (shown in Fig. 3.1a) before its fabrication using CFD modeling and simulation tools. The standard, double-stack TjM device and the proposed, triple-stack MEFM-4 device are shown in Figures 3.7 and 3.8 below. The main fabrication steps used were photolithography and Deep Reactive Ion Etching (DRIE). The three-step lithographic process used for the MEFM-4 to ensure structural and perfect back-to-frontside-alignment made its fabrication, as expected, challenging compared to the standard T-junction mixer. The DRIE recipe used enabled the deep etching of the mixing channels with vertical walls as well as the etching of the critical four-through holes, which aid the transport of one fluid from the back-side manifold (see Fig. 3.8b) to meet and mix with the second fluid that emerges from the front-side manifold (see Fig. 3.8a). The last processing steps that were implemented to make the microstructured wafers complete for our mixing studies were

the anodic bonding of the silicon substrates with 500-micron thick Pyrex™ glass wafers, followed by dicing of the bonded wafers into individual micromixers of sizes 6.45 cm x 2.54 cm and 3.50 cm x 3.00 cm for TjM and MEFM-4 respectively.

Figure 3.7: The T-junction Micromixer (TjM) fabricated from silicon substrate at CNF.

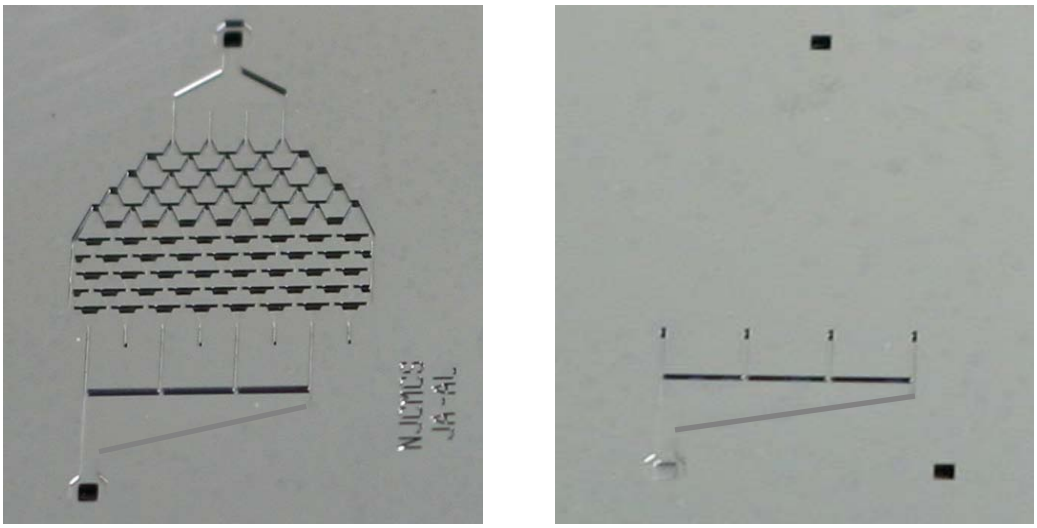

Figure 3.8: (a) The front-side and (b) The back-side - of the Multilaminated/ Elongational Flow Micromixer (MEFM-4) fabricated from silicon at CNF.

In continuation of our mixing studies in micromixers using residence time distribution (RTD) as a flow/mixing measure, the pulse input-response method was substituted for the step-input response method that we used previously. Some advantages that make pulse-input method a technique of choice for determining RTD include: the ease of analyzing data and interpreting experimental results; method requires very small amount of tracer; and the possibility of better reliability in the accounting for the amount of tracer introduced into the flow/mixing system than for the step-input method. The relative mixing performance of a standard T-junction micromixer (obtained from Mikroglas) and our fabricated, proposed multilaminated/elongational flow mixer (MEFM-4) was investigated experimentally using residence time distribution (RTD) as a flow/mixing measure. Using our RTD experimental set-up and applying pulse input-response method, time-dependent absorbance/concentration data were obtained at a volumetric flow-rate (Q) range of 0.10 - 0.50 mL/min for both the TjM and MEFM-4. Model fitting of the concentration data was subsequently performed to estimate the required flow/mixing parameter(s). Applying a non-linear regression programming scheme (implemented in Mathematica), the estimated Peclet numbers obtained at a flow rate of 0.50 mL/min, for instance, for TjM and MEFM-4 were 6.42 and 13.71 respectively. As a measure of characterizing dispersion/mixing in open mixing systems, the corresponding coefficient of variation (CoV) of the RTD was calculated to be equal to 54.2 and 37.9% for TjM and MEFM-4 respectively. As

expected, the lower CoV (and higher Peclet number, Pe = uL/D_z) was obtained for MEFM-4 with higher Pe implying lower axial dispersion (D_z). These results confirmed the fact that transverse mixing was enhanced and more dominant than axial dispersion/mixing in the proposed MEFM-4 than in TjM. To graphically elaborate on this result, Fig. 3.9 below shows the normalized RTD function, E [-], for TjM and MEFM-4, where the MEFM-4 has a narrower RTD compared to TjM. The longer tail of the normalized E curve for TjM (see Figure 3.9) compared to MEFM-4 also shows that the quality of mixing is better in MEFM-4. In essence, the smaller the CoV, the narrower the RTD, and the better the relative mixing performance of MEFM-4, which is in agreement with our earlier theoretical mixing study on these two micromixers.

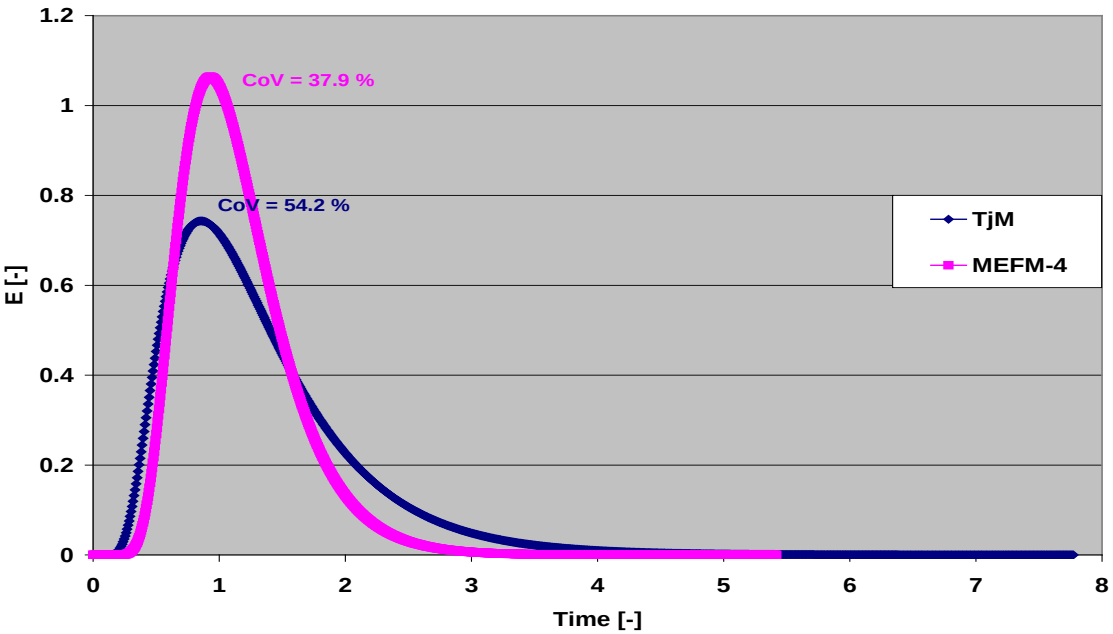

Figure 3.9: The plot of normalized E curves for TjM and MEFM-4 at a Q = 0.50 mL/min.

TASK 4: Nanostructured Thin-Film Catalyst Support

Our overall approach was to develop a library of catalyst integration methods applicable to this important research project in our Center. The catalyst integration approaches that we developed include:

- Open-channel surface-selective infiltration and deposition of sol-gel catalyst coating
- Closed-channel forced-flow infiltration and deposition of sol-gel catalyst coating
- Infiltration and immobilization of commercial catalyst particles by layer-by-layer self-assembly into various microreactor geometries
- Dipping approaches for infiltrating and depositing sol-gel catalyst coating into microcellular structures
- Infiltration and synthesis of microcellular structures that fill up microchannel volume

In the following sections, we summarized mainly our research activities on surface-selective infiltration and deposition of sol-gel catalyst coating, closed-channel forced-flow infiltration and deposition of sol-gel catalyst coating, layer-by-layer self-assembly of commercial catalyst, and synthesis of cellular structure inside the microchannels.

(1) Open-channel surface-selective infiltration and deposition of sol-gel catalyst coating

We developed a procedure to prepare and selectively infiltrate Pt/Al_2O_3 thin-film into "open" microchannel Si reactors. As shown in the Figure 4.1 below, we were able to synthesize highly dispersed Pt particles into a porous Al_2O_3 thin-film by sol-gel. Based on our characterization results, the thin film was determined to possess the following characteristics: BET surface area = 480 m^2/g, average Pt particle size = 11 nm, average pore diameter = 6 nm, and crystal structure of Al_2O_3 = amorphous.

Based on this procedure, we also developed a proprietary sol-gel synthesis procedure for preparing a Pd/alumina thin-film H_2O_2 synthesis catalyst on flat Si and stainless steel (SS) substrates with a thickness of a few microns. As evident from Figure 4.2, the thin-film catalyst is uniform, microcrack-free, and adherent. We also characterized the structure, morphology, and chemical compositions of the thin-film catalyst prepared by our proprietary technique, and compared to those of conventional powder catalysts used at FMC using transmission electron microscopy (TEM), scanning electron microscopy (SEM), energy dispersive spectroscopy (EDS), X-ray diffraction (XRD), BET surface area measurements, and inductively coupled plasma (ICP). The characterization results indicated that the key characteristics of our thin-film catalyst (i.e., surface area, pore size, density, and Pd loading) compared favorably to those of the commercial powder catalyst from FMC.

An open-channel surface-selective infiltration and deposition was also developed for stainless steel-based microchannel reactors. As shown in Figure 4.2, a support stage, which provides microfluidic transitions from the reactor testing system to a T-junction metallic microreactor, was designed and fabricated. Using the T-junction reactor, we demonstrated that a thin-film catalyst could be selectively deposited into the microchannel without contaminating the top reactor surface using the special procedures that we developed and demonstrated.

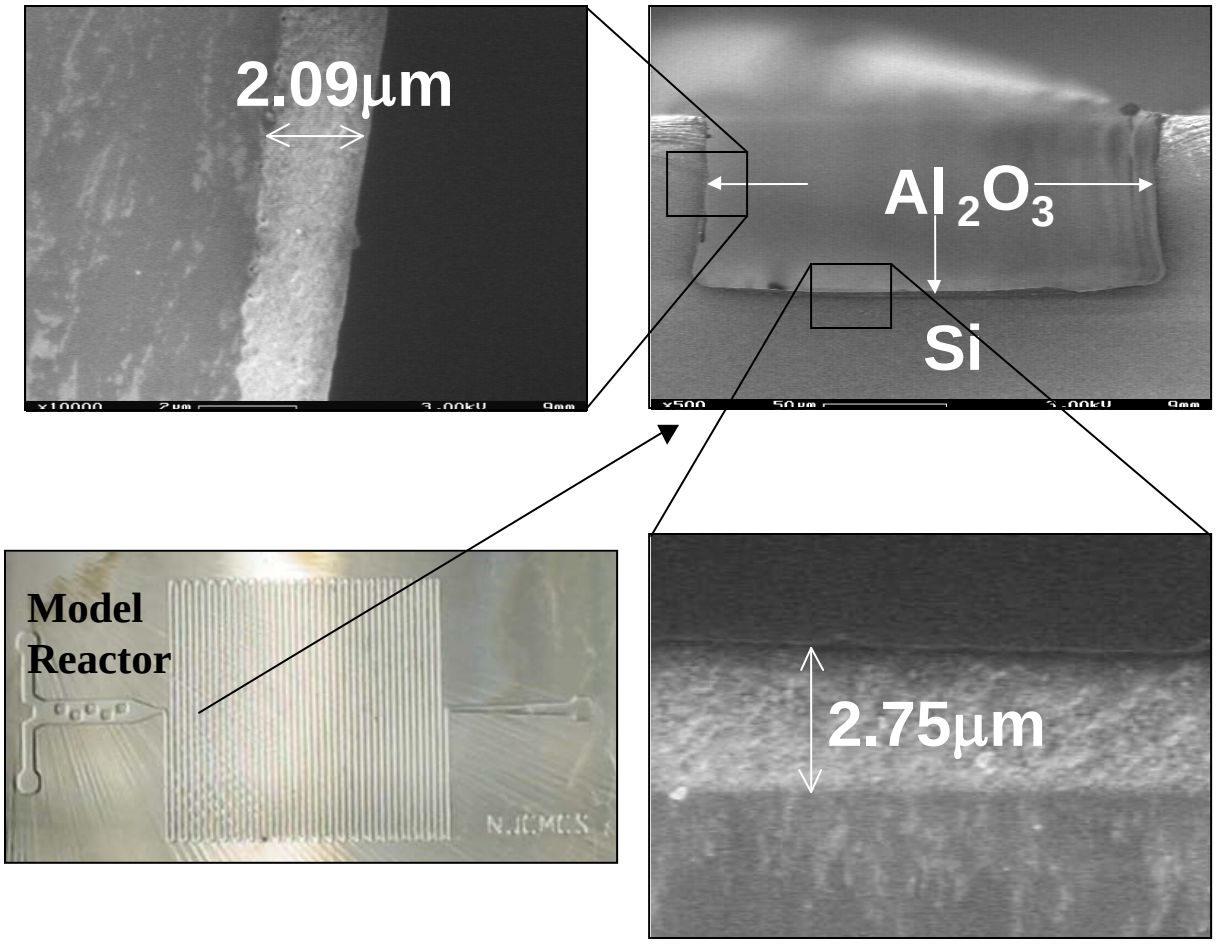

Figure 4.1: Si microchannel reactor infiltrated with Pt/Al_2O_3 thin-film. Cross-section SEM images show that the thin-film catalyst uniformly decorates the microchannel surfaces.

(2) Closed-channel forced-flow infiltration and deposition of sol-gel catalyst coating

In a parallel effort, we developed a proprietary infiltration procedure to uniformly coat the inner surface of microtube reactors with thin-film catalyst as shown in Figure 4.3. There was some localized delamination at the interface between the thin-film layer and the SS substrate surface. It appeared that the delamination occurred during our metallographic preparation of the coated microtube reactor for the cross-section analysis.

The sol-gel-based procedures were used to prepare 14 capillary tube reactors for testing under Task 5. Thickness of the thin-film catalyst was controlled to be ~0.8 μm and uniform along the 6-cm length of the capillary tube reactors.

The adhesion of the thin-film catalyst to the SS 316L substrate was evaluated by a peel test using Scotch tape on a qualitative basis. Overall, the thin-film catalyst adhered well to the substrate, except for a few local areas where some delamination was observed. For example, Figure 4.3 shows a microscopic view of the worst area. In this area, we observed that less than 10% of the thin-film under the viewing area was peeled off. The wetting behavior of the Pd/alumina thin-film catalyst on Si and SS316L substrates was studied as part of improving our infiltration procedure for 3-D microchannel reactors.

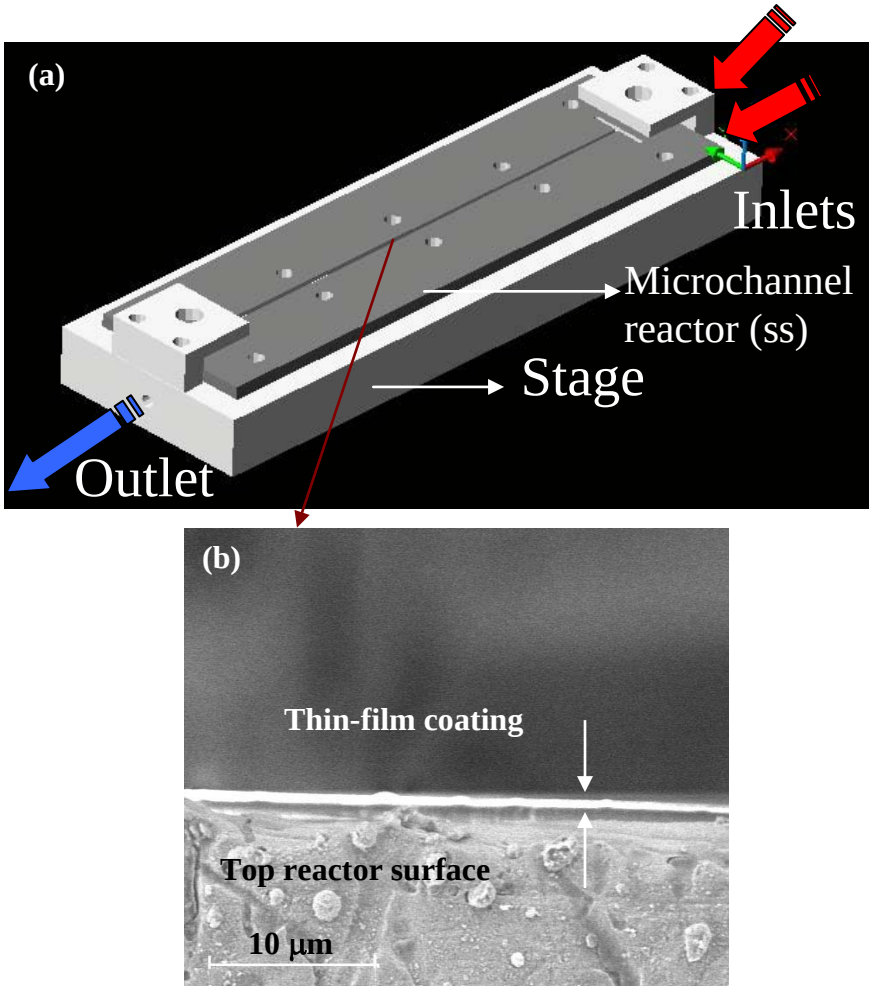

Figure 4.2: (a) T-junction reactor and the microfluidic transitions. (b) Thin-film catalyst selectively deposited on the wall of the T-junction channel.

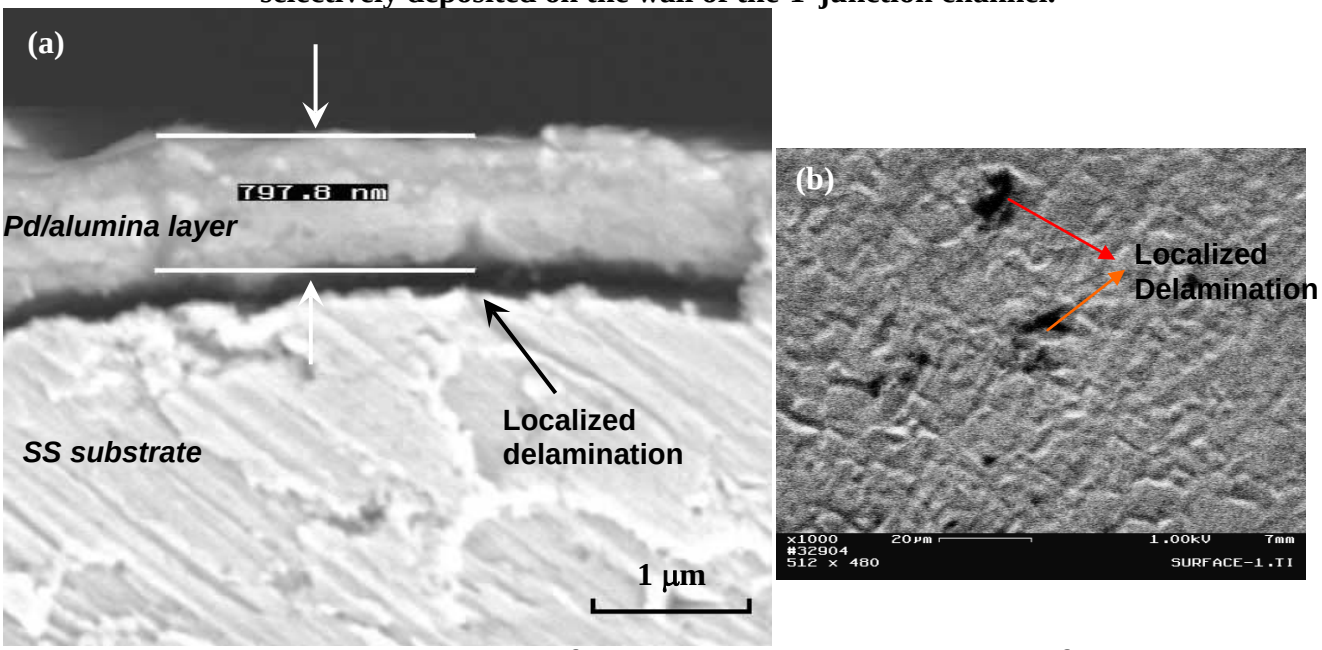

Figure 4.3: (a) Cross section view of the 6 cm long microreactor tube infiltrated. (b) Evaluation of the adhesion of Pd/alumina thin-film catalyst to the SS 316L by scotch tape test.

(3) Layer-by-layer self-assembly as a catalyst integration method

We also developed a procedure to immobilize model and catalyst particles in a thin film form on complex microstructures and building up the thickness of catalyst particles using layer-by-layer self-assembly (LBLSA).

The thickness of polyelectrolyte multilayers (PEMs) that determines the surface charge density on the surface is critical. The PEM thickness and particle surface coverage were controlled by the ionic strength of the polyelectrolyte solutions (NaCl concentration) and with the number of PEM layers (Figure 4.4). The particle surface coverage improves with increasing NaCl concentration and the number of PEM layers. However, the maximum surface coverage seems to be limited to about 70% as shown in Figure 4.5 (note that the surface coverage of 2-D close packing is ~91%) since there was no coverage increase with increased PEM thickness.

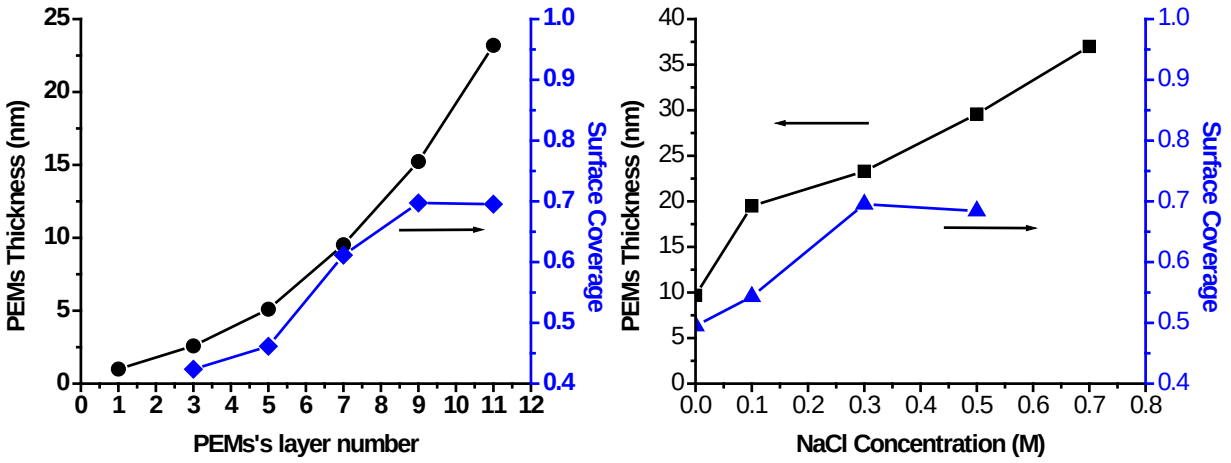

Figure 4.4: (a) Effects of the number of PEMs' layer on PEMs' thickness and the surface coverage of particles (b) effects of NaCl concentration on PEMs' thickness and the surface coverage of particles.

The layer-by-layer method was also applied to "build-up" the thickness of the particle film. By depositing repeatedly a single layer of particles, the layer-by-layer method provides a simple way of preparing relatively thick films with good uniformity. Figure 4.6 shows the SEM pictures of two and four layers of microspheres. The method was also successfully used to infiltrate and immobilize a number of commercial catalyst particles into complex cellular structures (Fig. 4.7).

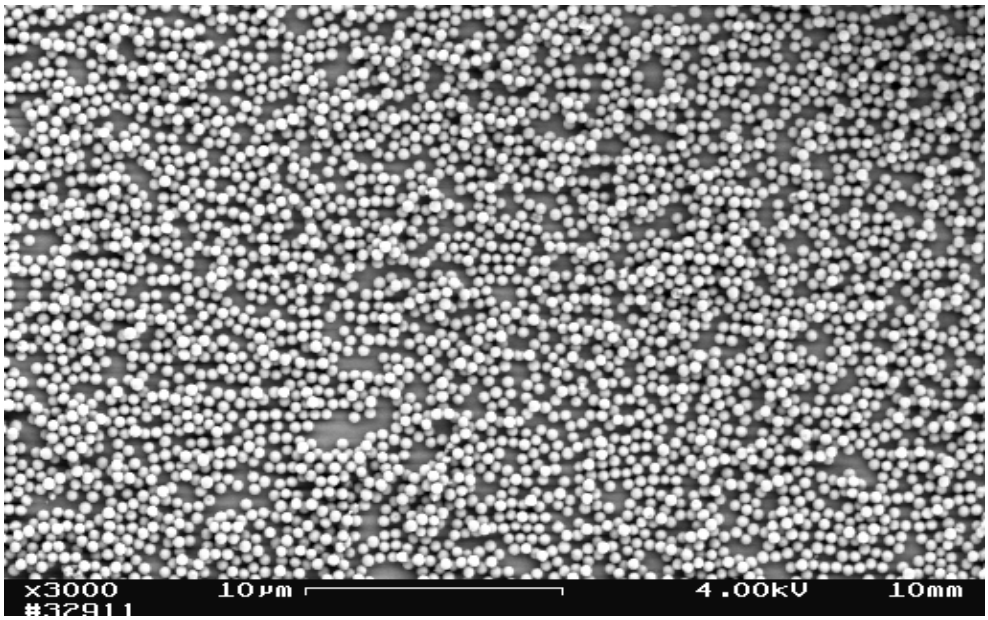

Figure 4.5: Coverage as high as 70% of single deposition of SiO_2 particles was achieved.

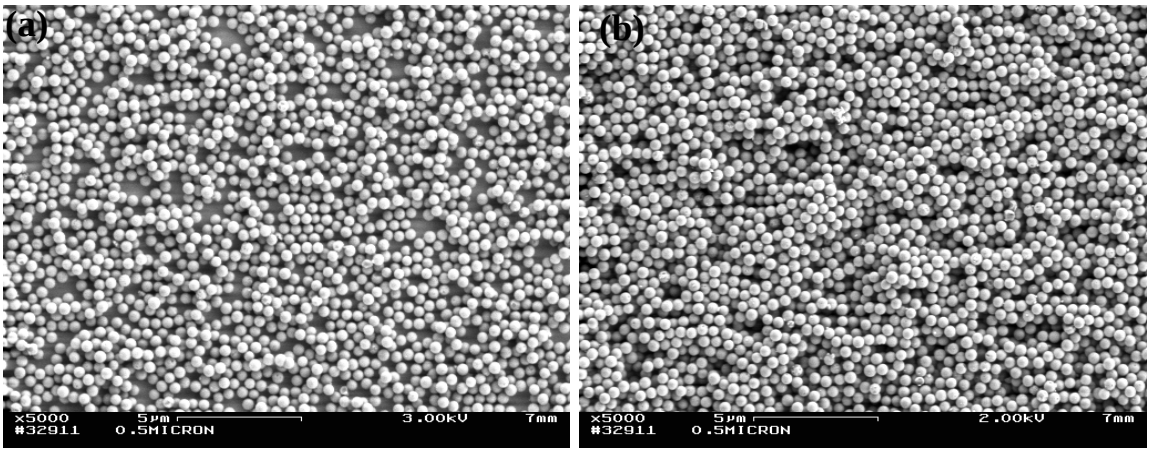

Figure 4.6: Building up the thickness of the particle thin film: (a) two and (b) four deposition cycles of silica microspheres (particle diameter - 500 nm).

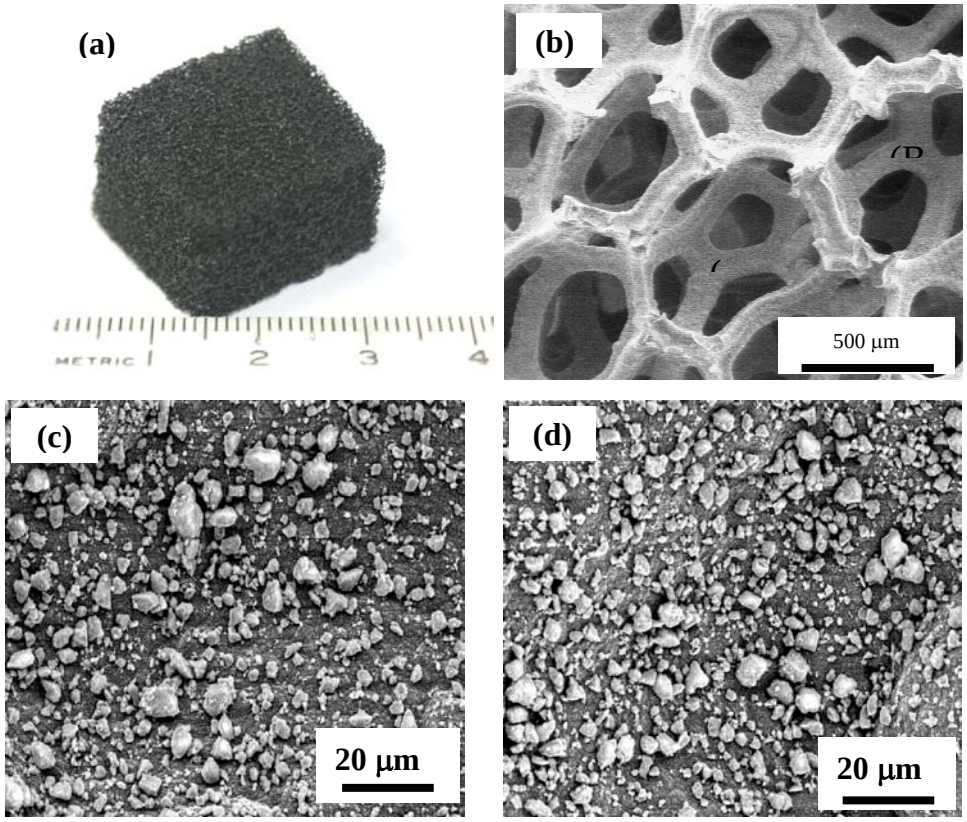

Figure 4.7: SiC cellular coupon infiltrated with the 1-layer catalyst particle assembly: (a) machined coupon with unit of the scale in cm, (b) SEM view of coated SiC skeleton, (c) and (d) SEM images of the catalyst particle assembly at points A and B in (b).

We also investigated the effects of LBL deposition on powder catalyst since it may influence the performance of the catalyst. However, any major adverse effect of the LBLSA procedures on the catalyst behavior was not evident in our study.

We evaluated the adhesion of the catalyst particle assembly deposited on flat substrates by the layer-by-layer assembly method as shown in Figure 4.8. For the evaluation, particles were assembled on model Si substrates (1.2 cm × 0.9 cm). A piece of Scotch tape was tightly attached to the top surface of the particle assembly. While the Scotch tape was being peeled off from the substrate, the force required to remove the tape was measured by a high-resolution force gauge (±0.001 N). The layer-by-layer self-assembled particles were expected to exhibit relatively poor adhesion to the substrate surface, since bonding between the particles and the substrate surface is mainly based on their weak electrostatic attractions. In order to further reinforce the immobilization of the particles on the surface, a thin layer of porous alumina was applied on the surface of the catalyst particle coating. Enhancement of the adhesion behavior by this alumina layer was observed as shown in Figure 4.8.

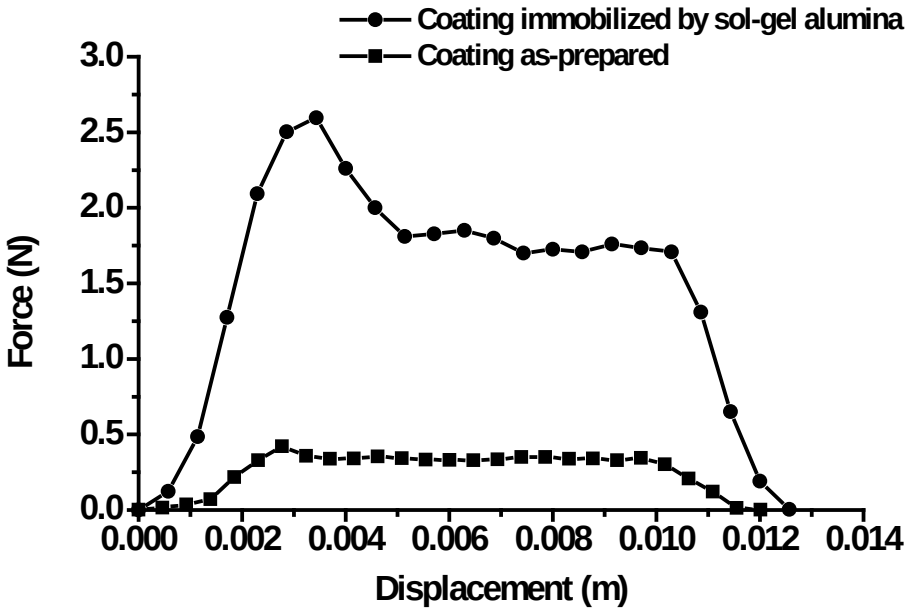

Figure 4.8: Degree of immobilization of the catalyst particle assemblies

We found that an additional thin layer of porous alumina could be used to significantly enhance the degree of adhesion if such reinforcement were desired. Adhesion behavior of the catalyst particle layer was investigated by microscopic evaluation of the delaminated surfaces resulting from the Scotch tape testing. For the catalyst layer which was not reinforced with porous alumina, the catalyst layer was mostly removed from the substrate surface. However, the catalyst layer reinforced with alumina layer was only partially removed. Figure 4.9 shows that the alumina layer diffused into the catalyst layer and formed direct contact with substrate surface.

(4) Infiltration and synthesis of microcellular structures that fill up microchannel volume

We developed a procedure to synthesize cellular structure inside microchannels to be used as a microstructure for catalyst coating (Fig. 4.10). We focused our work on optimizing the cellular structure by controlling three key structural parameters: cell size, window size, and skeleton density. Other properties of the cellular structure such as pore interconnectivity, geometrical surface area, void fraction, pressure drop and mechanical strength derive from these key parameters.

The cell size of the cellular structure was determined by the size of the microspheres used in the sacrificial template. Polystyrene microspheres with diameter in the range of 10 - 20 μm were used for the template, and the diameter of spherical cells (Figure 4.11a) in the cellular structure should be in the same range or slight smaller due to structure shrinkage during drying (Figure 4.11a). After the microspheres were packed into the microchannel using a surface-selective infiltration method they were heated at 100°C. The size of the contact area of two neighboring spheres r_N (Figure 4.11a) was controlled by the heating time, thus resulting in a certain window size in the final cellular structure. Cellular structures synthesized from template sintered after three and six minutes show some difference in cell interconnectivity (Figures 4.11c and 4.11d).

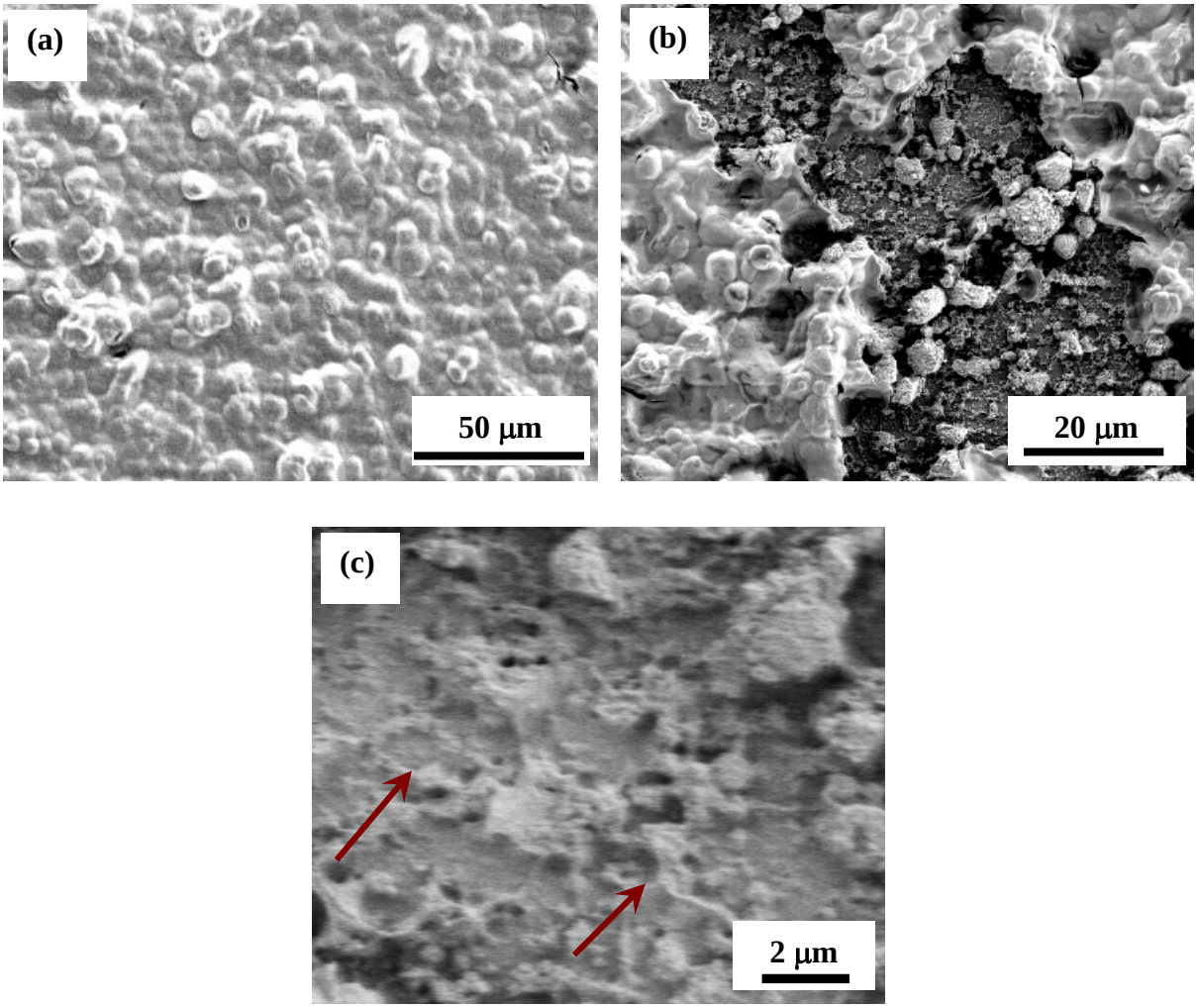

Figure 4.9: Surface scanninge electron micrographs of the catalyst particle layer reinforced with an additional layer of porous alumina: (a) before the adhesion test and (b) and (c) after the adhesion test. The arrows in (c) point indicate the alumina phase remaining on the surface.

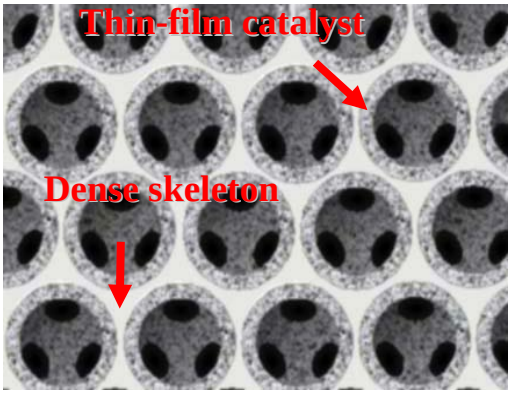

Figure 4.10: Cellular catalyst support structure.

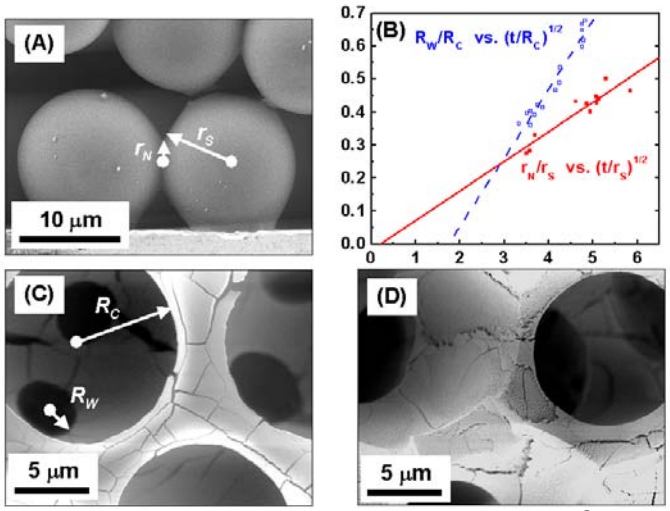

Figure 4.11: Controlling cell interconnectivity: (a) Sintering of microspheres: r_N and r_S are the radius of the contacting area between two neighboring spheres and the radius of the spheres, respectively; (b) Controlling polystyrene sintering and cell interconnectivity by changing sintering time; solid line shows the change of the polystyrene template by varying sintering time and the dotted line shows the change of cell interconnectivity of the cellular structures from sintered template; t is heating time in seconds; (c) Cellular structure from template sintered for three minutes; (d) Cellular structure from template sintered for six minutes.

We have successfully synthesized skeleton in the interstices of the microsphere template with high density and no cracks, which is a challenging task. As shown in Figure 4.12, free-standing cellular silica samples were synthesized from TEOS and Ludox®.

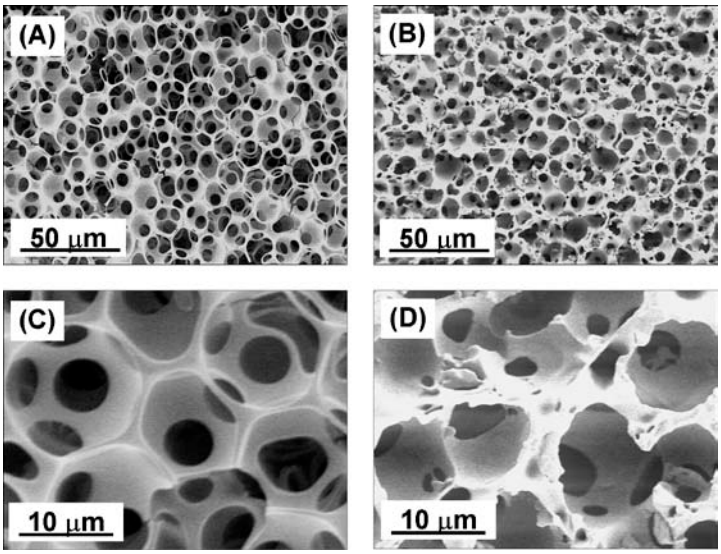

Figure 4.12: Free-standing cellular silica samples synthesized from: (A) and (C) TEOS precursor after the 500°C calcination step and (B) and (D) Ludox® precursor after the 1100°C sintering step.

The microcellular structure, combined with thin-film coating technique developed in this project provides an additional catalyst integration choice.

Task 5: Laboratory Reactor System Optimization and Evaluation

I. Summary

A laboratory microreactor system was designed, evaluated and optimized for the production of H_2O_2. H_2O_2 was safely produced by direct combination of H_2 and O_2 in all proportions including the explosive regime. Both commercially available and proprietary catalysts under development were screened for their performance. A catalyst formulated and prepared in-house using the sol-gel method achieved concentrations as high as 1.5 wt % H_2O_2. Optimum ranges of temperature, and pressure for H_2O_2 production were determined in the microreactor system. Four different reaction pathways were identified in the direct combination of H_2 and O_2, and kinetic experiments were conducted for three of these pathways by isolating each reaction and ensuring that experimental conditions were free of mass transfer limitations. The three reactions are (1) H_2O_2 synthesis (2) H_2O_2 reduction by H_2 and (3) H_2O_2 decomposition. Mechanisms were proposed for each reaction based largely on general trends of our kinetic data. Rate expressions were derived for these mechanisms and kinetic constants calculated from the kinetic data. Mechanisms not confirmed by the data following a rigorous evaluation procedure were rejected. An overall rate expression was obtained that can be used in the design and optimization of microreactor system for production of H_2O_2 by the direct combination method.

II. Performance and Optimization Studies

II.1. Experimental Methods

The reactants for the three reactions were (1) hydrogen (Ultra High Purity, Praxair) and oxygen in the form of air (Extra Dry, Praxair) for the H_2O_2 synthesis (2) hydrogen and hydrogen peroxide (35 wt. %, Sigma-Aldrich) for H_2O_2 reduction and (3) hydrogen peroxide and air for the decomposition reaction. Nitrogen (Ultra High Purity, Praxair) was used to dilute the hydrogen stream. The liquid phase consisted of deionized water with 10 ppm NaBr (Aldrich), 1% (w/w) H_2SO_4 (A. C. S. reagent grade, 95-98%, Aldrich) for the first two reactions, and specified concentration of H_2SO_4 for the decomposition reaction. The hydrogen peroxide used for the reduction experiments contained tin and phosphorus stabilizers at trace concentrations, which is common for commercial H_2O_2 solutions. We showed that the stabilizers had no effect on the rate of H_2O_2 reduction by comparing the reaction rates with unstabilized and purified (A. C. S. reagent grade, 30 wt. %, Fisher Scientific) H_2O_2 solutions. Even though the decomposition reaction takes place in the liquid phase, a gas phase was added in order to simulate the conditions present during H_2O_2 formation. The main effect of the gas phase was to influence the residence time in the reactor. When the decomposition reaction was run without any gas phase, the reaction rate was proportional to the increased residence time.

The reactants were passed through a 2-µm filter before entering the reactor. A schematic of the experimental set-up used for all experiments is shown in Figure 5.1. The flow rates of hydrogen, oxygen (as air) and nitrogen were controlled by mass flow controllers (Porter Model 201). Flow rate of the solvent was controlled by an HPLC pump (Lab Alliance Series III) and the solvent was combined with mixed gas in a PTFE micromixer (Upchurch). All streams flowed in 1/16" 316L SS tubing with 765 µm ID. The microreactor consisted of the same type of tubing packed with catalyst, enclosed with filters of polypropylene wool for retaining the catalyst, and connected to the system horizontally with PTFE fittings (Upchurch). The same type of tubing was used for all gas and liquid streams. According to the results of Hong and co-workers (2003),

the quenching distance at the operating conditions used in this work is approximately between 300 and 500 µm. Thus the diameter of the reactor tube is larger than the quenching distance at the conditions used in this work. However, the small void spaces between the catalyst particles and the presence of the liquid phase ensure that hydrogen explosions were suppressed.

The amount of the catalyst packed into the microreactor varied between 4 and 21 mg with the low values used for kinetic experiments. The length of the microreactor was chosen such that about 2-3 cm of empty tubing would remain after the reactor was packed. The empty space was then packed with glass beads of the same size range as the catalyst in order to prevent the catalyst particles from blocking the retaining filter at the downstream end of the reactor. Temperature in the microreactor was controlled by immersing it in a constant temperature water bath (Thermo-Haake DC10). Pressure was controlled by a backpressure regulator (Circle Valve Technologies) and continuously recorded using LabView software. The gas stream was diluted with N_2 to below the explosive limit prior to leaving 1/16" tubing at the system's outlet. Concentration of H_2O_2 in the liquid phase was determined by titration with potassium permanganate and gas phase composition was measured by a Shimadzu GC-14B gas chromatograph with a Mole Sieve 5A column at 35°C and argon as carrier gas. Pressure drop across the reactor varied between approximately 3-17% of inlet pressure (depending on the total flow rate), however the average pressure was maintained at 300 psig for all experiments, unless stated otherwise. The gas/liquid ratio was held constant at 440 (v/v, at standard conditions).

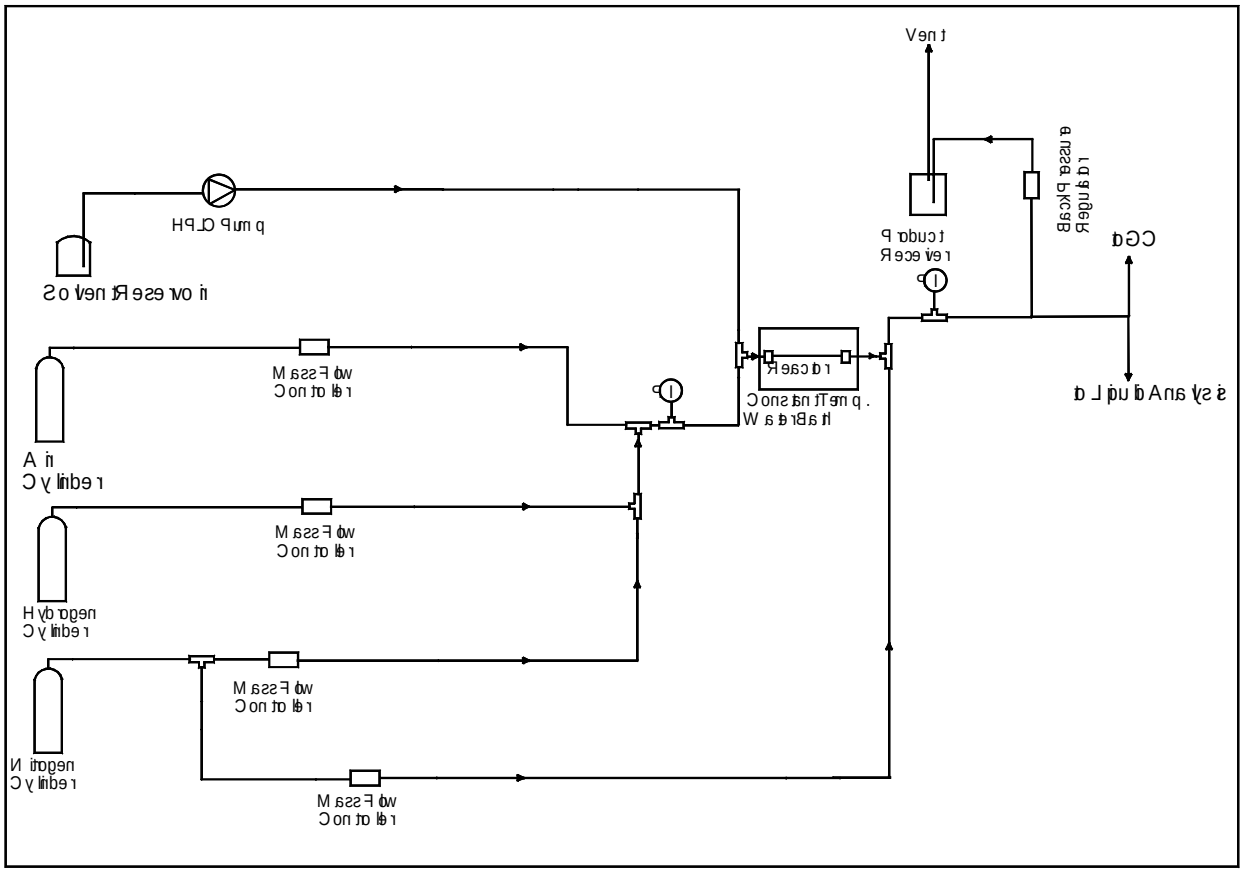

Figure 5.1: Experimental set-up for direct combination process for formation of H_2O_2.

Productivity was expressed as space-time yield, calculated as

$$STY = \frac{C_{H_2O_2} F_{liq} MW_{H_2O_2}}{W_{Pd}} \quad (5.1)$$

Selectivity was calculated using Equation 5.2 on the basis of H_2 as the limiting reactant. This definition of selectivity only applies to reactions with a 1:1 stoichiometry, that is, 1 mole of product formed for one mole of limiting reactant reacted.

Selectivity = (moles of H_2O_2 formed)/(moles of H_2 reacted) x 100% (5.2)

II.2. Catalyst Preparation

The catalyst used for all experiments was 2% Pd on SiO_2, prepared by the sol-gel method with $PdCl_2$ as the source of palladium. The gel was prepared from tetraethoxysilane (TEOS), ethanol and water (Robles-Dutenhefner et al., 2004) and calcined. Activity of the catalysts prepared using this method was typically reproducible within 10%. The calcined catalyst was ground and sieved to obtain particles with a diameter in the range 75-150 μm. This is the particle size range used in all experiments in this work, unless specified otherwise. Surface area of the catalyst was 603 m^2/g(multi-point BET technique, using Quantochrome Instruments Autosorb-1), the size of Pd particles was found to be in the range of 2-10 nm, with an average of 7 nm, and a dispersion of 18.1 % (FEG-TEM, Model CM20, Philips, Eindhoven, Netherlands).

II.3. Effect of Temperature and Pressure

Experiments were carried out at various pressures and temperatures in order to find the optimum parameters for production of 1 wt% H_2O_2 and for further kinetic experiments. Effect of temperature on the reactor performance can be seen in Figure 5.2. Space-time yield, conversion and selectivity increase with temperature and then stabilize. The initial increase in selectivity must be due to the rate of synthesis reaction increasing with temperature faster than the rate of reduction, which implies that the activation energy of synthesis is higher than that of reduction. All three curves become independent of temperature above 42 °C.

Figure 5.3 shows the effect of total pressure. The residence time was kept constant by maintaining a constant *F/W* ratio. Selectivity increases, while H_2 and O_2 conversions decrease with pressure, and then stabilize above 200 psia, while the space-time yield increases almost linearly with pressure. The increase in selectivity with pressure may be due to one of, or both, of two factors: 1) the rate of reaction (1) in Scheme 1 below may have a stronger dependence on the partial pressures of hydrogen and oxygen than the rate of reaction (3), and 2) the direct formation of water may be significant at lower pressures, but decreases essentially to zero at 300 psig. The decrease in O_2 conversion, and the fact that selectivity for H_2O_2 is 100% at 300 psig and with very small conversions (<2%), support the second explanation. Based on the data in Figures 5.2 and 5.3, kinetic experiments were carried out at an average total pressure of 300 psig and at 35-50°C because the selectivity and productivity are highest at these conditions.

A.

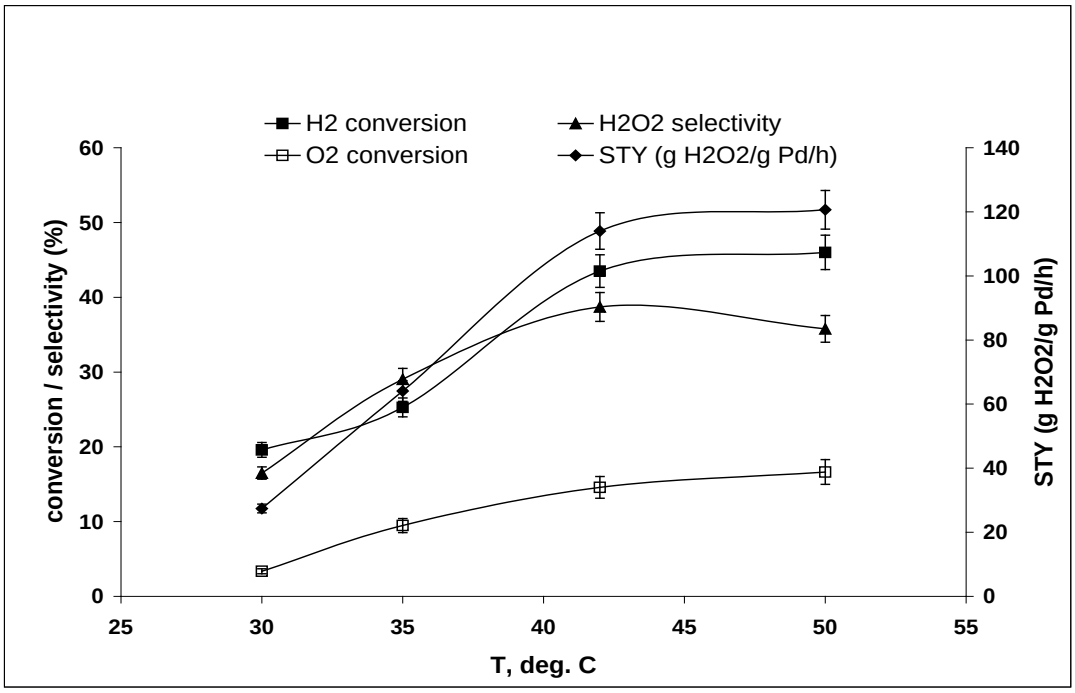

B.

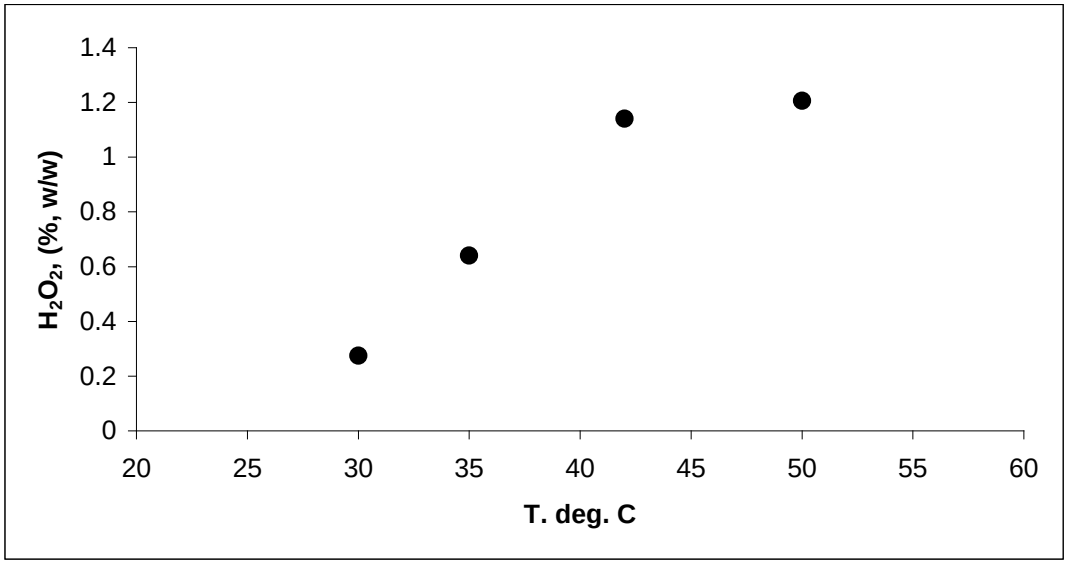

Figure 5.2: Effect of temperature on formation of H_2O_2: A. H_2 conversion, H_2O_2 selectivity, and space-time yield. B. Concentration of H_2O_2 at reactor's outlet. Reaction conditions: Gas composition: 9.1% H_2 in air, total pressure = 300 psig, gas flow rate = 22 ml/min (at standard temperature and pressure), liquid flow rate = 0.05 ml/min, 15 mg of catalyst.

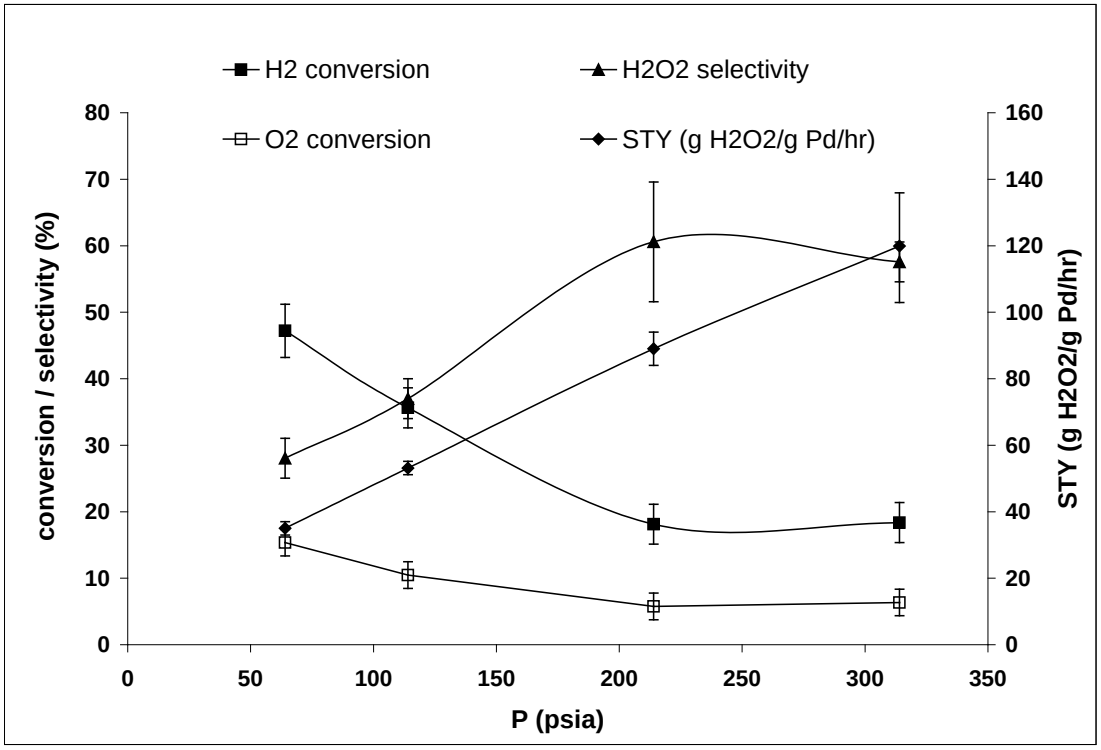

Figure 5.3: Effect of total pressure on formation of H_2O_2.
Reaction conditions: Gas composition: 9.1% H_2 in air, T = 42 °C, residence time (in empty reactor) = 1.1 sec.

III. Kinetics of Direct Combination Process

III.1. Reaction Pathways

Any attempts to determine the kinetics of the DC reaction must deal with the multiple reactions involved in this process. The reactions involve synthesis and consumption of hydrogen peroxide and take place in series and in parallel, as shown in Scheme 1. Water and hydrogen peroxide are synthesized in parallel steps and H_2O_2 can be consumed either by reduction, or by decomposition (disproportionation). Thus, in order to predict the rate of H_2O_2 formation, we need to know the rates of all four reactions in Scheme 1.

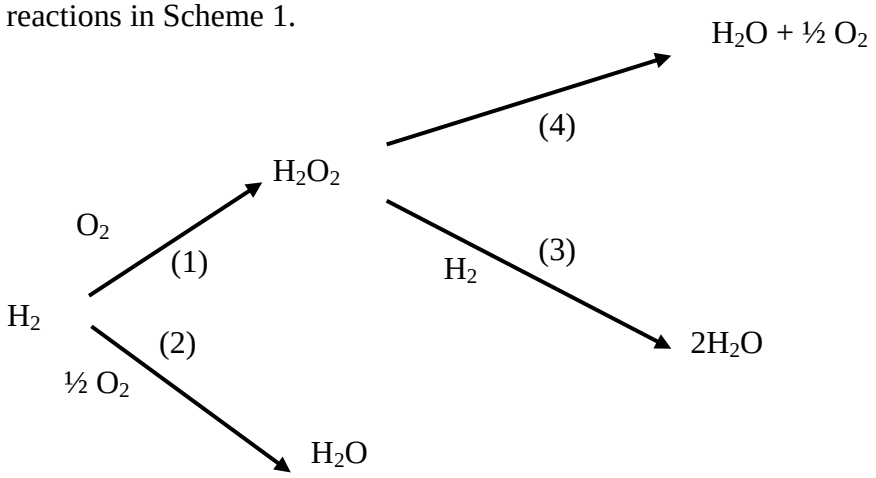

Scheme 1: Reactions involved in the formation of hydrogen peroxide.

A complete and usable rate expression at high H_2 concentrations has not been obtained in the past because of the danger and complexity of the H_2/O_2 reaction. Instead of regressing the complete mass balance for equations (1)-(4), our strategy was to isolate the reactions in Scheme 1 and to obtain the rate expressions of individual reactions that would be accurate at a wide range of reactant concentrations.

III.2. Flow Regime and Mass Transfer Limitations

Prior to determining the kinetics, we had to demonstrate the absence of internal and external mass and heat transfer limitations in this system for each of the reactions and the general procedure we followed is outlined here. Our flow visualization experiments showed that the flow regime in the microreactor is very close to Taylor flow, with distinct gas and liquid slugs. The only factor distinguishing it from true Taylor flow was the packing, which continuously broke the liquid slug boundaries, thus creating mist-like tails trailing behind liquid slugs. Thus, the catalyst particles were exposed to three types of environment: 1) liquid slugs, 2) the mist trailing behind liquid slugs, and 3) gas slugs. The absence of a liquid phase around the particles could be clearly seen during the passage of the gas slug. Wada and co-workers (2003) observed a similar flow regime at the same gas and liquid velocities in a multichannel microreactor with vertical posts installed inside the channels. Unlike in a packed-bed microreactor, the liquid slugs were not broken up by the posts. However, similarly to the packed-bed microreactor, the posts were alternately exposed to gas and liquid phases. This is a relatively complex flow regime, which is not likely to be replicated in a reactor other than a packed-bed microreactor. Nevertheless, the kinetics of H_2O_2 reduction obtained here are applicable to any type of reactor because, as will be shown below, the kinetic experiments were done in the kinetically controlled regime.

A gas-liquid-solid reaction that takes place in the slug flow regime typically involves three external mass transfer steps: from gas to liquid, from liquid directly to solid, and from gas to solid through a thin liquid film (Figure 5.4).

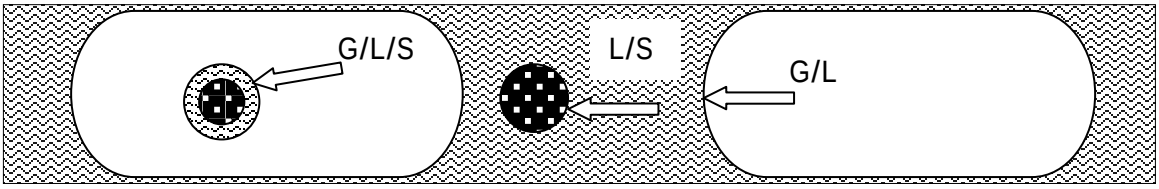

Figure 5.4: Schematic of mass transfer steps in the packed-bed microreactor.

The gas-liquid mass transfer step is typically the slowest of the three (Losey et al. (2001), and a commonly used criterion for determining the relative importance of an external mass transfer gradient is given by Mills and Chaudhari, 1997:

$$\frac{R_A}{k_{gl}a_{gl}C_{A,sat}} < 0.1 \tag{5.3}$$

For the system used here, the mass transfer coefficient could not be directly calculated because all the known correlations of mass transfer coefficients, such as the ones for trickle or bubble flow in a packed bed (Satterfield, 1970) or Taylor flow in an empty tube (Bercic and Pinter, 1997), do not apply to slug flow in a packed bed. Instead, we showed that this mass transfer step

did not control the reaction rate by measuring the effect of flow velocity on reaction rate, while keeping the residence time constant by maintaining a constant *F/W* ratio. Results for synthesis reaction in Figure 5.5 show that the reaction rate did not depend on flow velocity as long as the superficial flow velocity was at least 0.02 m/s. This implied that there was no significant concentration difference between the catalyst surface and liquid surface. The velocities used for the kinetic experiments were in the range of 0.44-1.3 m/s.

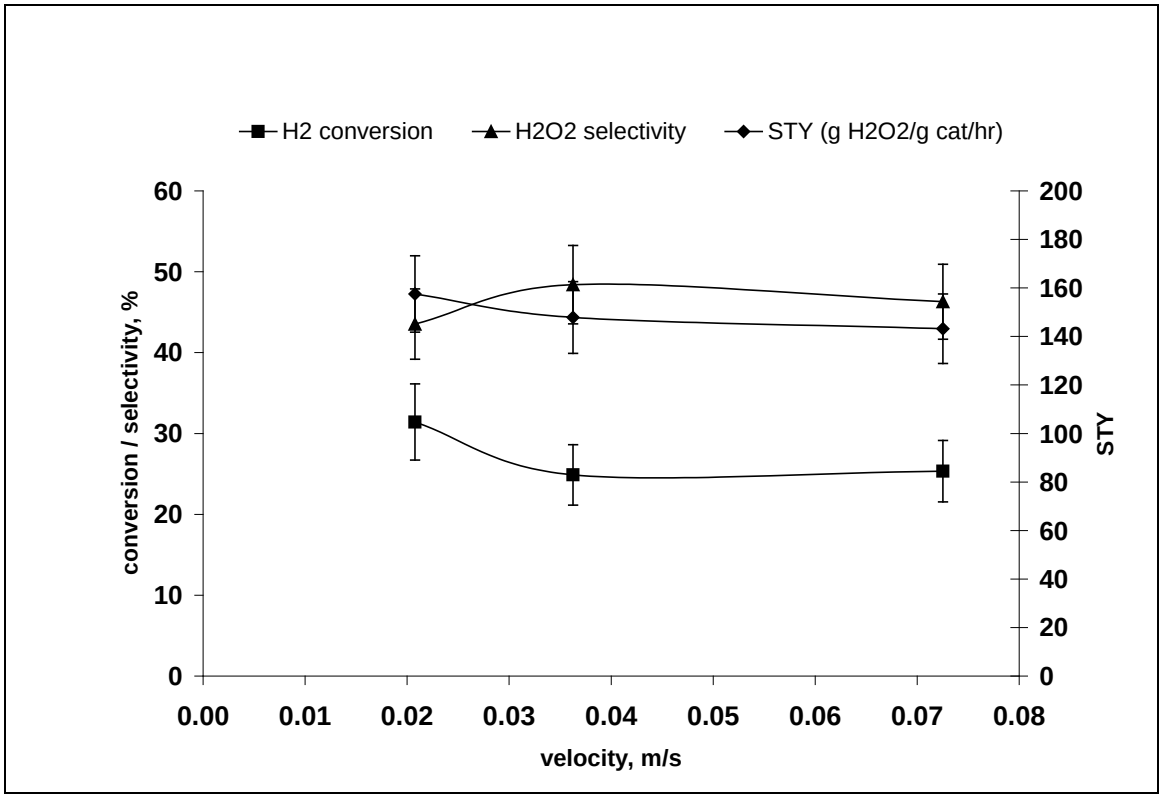

Figure 5.5: Effect of total flow velocity on formation of H_2O_2.
Reaction conditions: Gas composition: 9.1% H_2 in air, total pressure = 300 psig, T=50 °C, residence time (in empty reactor) = 1.1 sec.

Thus, we considered the criterion in Equation 5.3 satisfied, which allowed us to calculate the minimum mass transfer coefficient by setting the ratio in Equation 5.3 equal to unity. This resulted in a lower limit for $k_{gl}a_{gl}$ of 8 s^{-1} (calculated at 150 g H_2O_2/g Pd/h), which is in the range of $k_{gl}a_{gl}$ values obtained by Losey at al., 2001 in a packed-bed microreactor (5-15 s^{-1}).
The significance of an internal mass transfer limitation was estimated by assuming a first-order rate law and calculating the first-order Thiele modulus (Losey et al., 2001, Fogler, 1992) using equation 5.4:

$$\phi_{\exp} = \frac{d_p}{6}\left[\frac{\rho_p r'_A}{D_e C_{A,sat}}\right]^{0.5} \qquad (5.4)$$

We illustrate the procedure using the reduction reaction. The Thiele modulus, calculated using the highest reaction rate achieved in the kinetic experiments, with the typical values of porosity (0.5), tortuosity (5), and the constriction factor (0.75) (Fogler, 1992) and using the binary diffusivity of H_2 in water, was calculated to be 0.15. This corresponds to an effectiveness factor of unity, which implies that the internal mass transfer has no significant effect on the observed reaction rate. The results in Figure 5.6 show that the catalyst particle size had no significant effect on the rate of H_2O_2 reduction, thus confirming the calculated effectiveness factor.

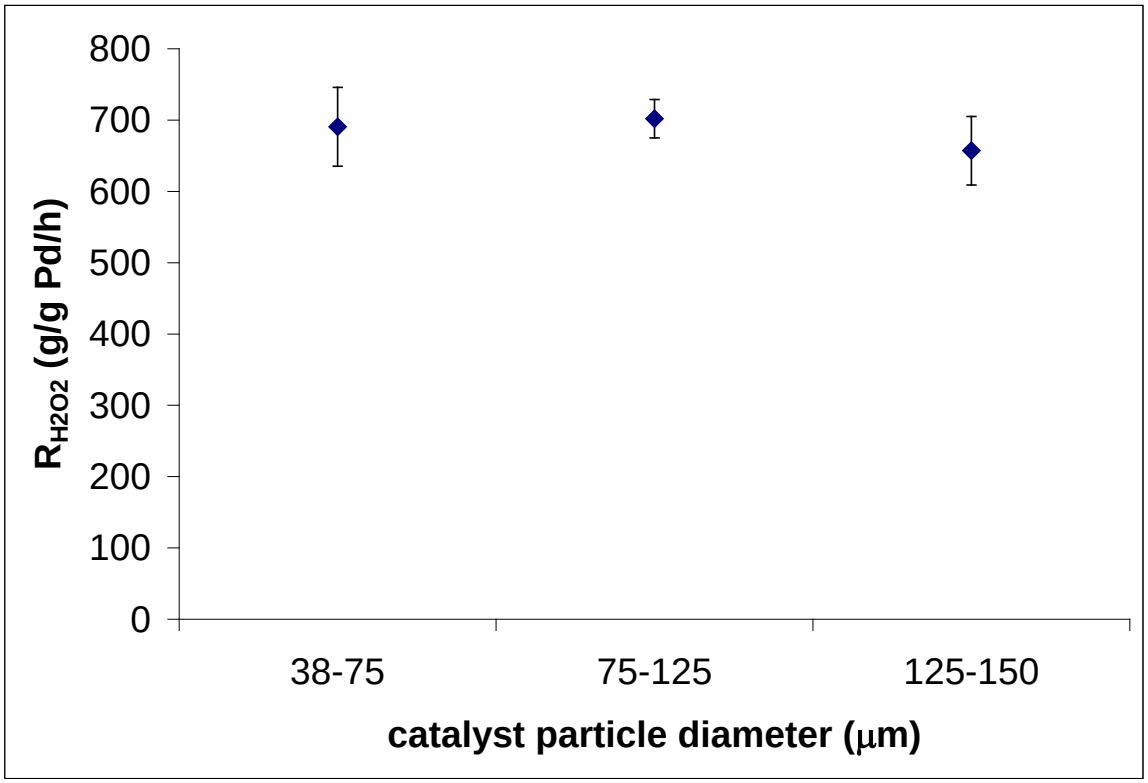

Figure 5.6: Effect of catalyst particle size on rate of H_2O_2 reduction. Reaction conditions: Gas phase: 14% (v/v) H_2 in N_2; liquid phase: 0.64 mol/l H_2O_2 in water with 1% (w/w) H_2SO_4 and 10 ppm NaBr; total pressure = 300 psig, 50 °C.

The presence of a radial heat transfer limitation can be determined using the Mears criterion (Mears, 1971), as shown in Equation 5.5:

$$\frac{\left|-\Delta H(-r_{H_2})d_p{}^2\right|}{\lambda_e T_w} < 0.4\frac{RT_w}{E_a} \tag{5.5}$$

Using a thermal conductivity value that is common for this type of catalyst (Sharma et al, 1975), the left side of the equation was calculated to be smaller than the right side by several orders of magnitude, implying that the reaction rate was not controlled by heat transfer. The axial heat transport can be neglected when $L/d_p > 30$ (Mears, 1971), where L is the length of the catalyst bed. This condition was certainly satisfied for the microreactor for all three reactions.

III.3. Kinetics of Synthesis Reaction

Two main areas of focus for researchers in this field have been the mechanism of the synthesis reaction and the controlling factors that affect the rates of reactions in Scheme 1. Pospelova and co-workers determined the main features of the mechanism of reaction (1) (Pospelova and Kobozev, 1961a) and discovered the promoting effect of halides and acids on the formation of H_2O_2 (Pospelova et al., 1961). The mechanism they proposed involved dissociative adsorption of H_2 on an active site consisting of two palladium atoms, non-dissociative adsorption of O_2 on the same site, and a surface reaction between H_2 and O_2 to form H_2O_2 through a HO_2^- intermediate. The same group also found that certain halide salts and acids can act as promoters for H_2O_2 formation. Most of their results were recently confirmed using modern spectroscopy techniques (Sivadinarayana et al., 2004, Chinta and Lunsford, 2004). The fact that O-O bond does not dissociate during H_2O_2 formation was experimentally confirmed by Dissanayake and Lunsford, 2003, and the presence of HO_2^- on catalyst surface during the reaction was discovered by Sivadinarayana et al., 2004.

In the recent decade, much work has been done to investigate in greater detail the effect of various parameters on the DC reaction. The group of Choudhary demonstrated the effect of the nature and concentration of acid and halide promoters on reactions (1), (2) and (3), as well as the effect of the oxidation state of palladium (Choudhary and Samanta, 2006; Samanta and Choudhary, 2007a; Choudhary et al., 2006a, 2007). A mechanism for reactions in Scheme 1 was proposed that accounted for the promoting effect of halides and protons (Choudhary and Samanta, 2006). The mechanism of inhibition of H_2O_2 consumption reactions by halides and protons was also investigated by the group of Lunsford (Dissanyake and Lunsford, 2003; Chinta and Lunsford, 2004) and Landon (Landon et al., 2003). The promoting effect of halides on formation of H_2O_2 was clarified by Chinta and Lunsford, 2004, who demonstrated that Br^- inhibits the direct formation of water, rather than slow down either the reduction or decomposition of H_2O_2, most likely by poisoning the catalytic sites active in breaking the O-O bond to form water (Burch and Ellis, 2003). Cl^- has the same effect as Br^-, but higher concentrations are required (Lui and Lunsford, 2006). When H^+ is present in sufficient concentration in the reaction medium, reaction (3) is suppressed and can be neglected, so that H_2O_2 is consumed only through reaction (4) (Landon et al., 2003, Chinta and Lunsford, 2004). Reaction (1) is less affected by the halides than reactions (2)-(4), so that the halides significantly increase the selectivity for hydrogen peroxide (Choudhary and Samanta, 2006). This effect applies to halides dissolved in the reaction medium, as well as to those incorporated into the catalyst support (Samanta and Choudhary, 2007b). In summary, the additives increase the rate of H_2O_2 formation by inhibiting the decomposition and reduction reactions. This is the reason why 1% H_2SO_4 and 10 ppm NaBr were present in the liquid phase during our experiments on the synthesis of H_2O_2 by direct combination.

Despite an extensive body of research on the Direct Combination process, there are no prior studies where the kinetic rate expressions of the full reaction network in Scheme 1 were described and verified. The only known attempts to obtain rate equations describing the kinetics of Direct Combination reactions were made by the groups of Inoue et al. (2007) and Melada et al. (2006a,b). The former group determined a power-law kinetic constant for the synthesis of H_2O_2 (reaction (1) in Scheme 1), and the latter group determined the power-law rate constants for the synthesis of peroxide, synthesis of water, and reduction of peroxide. Both groups performed experiments at relatively low hydrogen concentrations, whereby the rate of H_2O_2 formation had a first-order dependence with respect to hydrogen and oxygen. This allowed the

researchers to obtain power-law kinetic constants. However, power-law rate expressions for the DC process are accurate only at low concentrations of reactants. At higher concentrations, there is an increase in the fraction of occupied catalytic sites, which leads to the increasing importance of adsorption effects. Under these conditions, a significant fraction of reactants cannot take part in the reaction because of the lack of available catalytic sites. The reaction becomes dominated by the rates of adsorption, and the power law rate expressions cannot predict the reaction rate accurately any more. Langmuir-Hinshelwood rate expressions take into account the effects of adsorption and desorption and are appropriate for a complete description of the kinetics of a catalytic reaction (Vannice, 2005). Since our goal was to determine the kinetics of the Direct Combination process that would be applicable for producing H_2O_2 at concentrations of up to 5 wt%, which is sufficiently high for power-law rate expressions to become inaccurate, we aimed to obtain and verify a set of Langmuir-Hinshelwood rate expressions that can describe the rates of reactions in Scheme 1 as they take place simultaneously in a packed-bed microreactor.

We isolated the synthesis reaction by operating the reactor in the differential mode, where the conversion of reactants was not more than approximately 2%. Under these conditions, the selectivity for H_2O_2 was 100%. At such small conversions, space-time yield can be assumed to be the intrinsic reaction rate. For all experiments, the reaction rates used in all the calculations were steady state values measured after the reactor performance had been stabilized for about two hours. Four mechanisms (Table 5.1) were proposed for the synthesis reaction and surface reaction was assumed to be the rate-determining step for all mechanisms because the reaction rate became independent of reactant concentrations as the concentrations increased and then slowly decreased, which implies that the adsorption steps are in equilibrium. Mechanism 4 was selected as the best-fitting model because it had the highest R^2 values of kinetic and Arrhenius curves. The values of the kinetic parameters are presented in Table 5.2 – 5.3.

Table 5.1: Proposed mechanisms for synthesis of H_2O_2 *=Pd catalytic site.

Mechanism No.	Mechanism	Rate Law
1	$H_2 + 2* \rightarrow 2H*$ $H* + O_2 \rightarrow *HO_2$ $H* + *HO_2 \rightarrow H_2O_2 + 2*$	$r = \frac{k_3 K_{H_2} K_{O_2} P_{H_2} P_{O_2}}{\left(1 + \left(K_{H_2} P_{H_2}\right)^{1/2} + K_{O_2}\left(K_{H1} P_{H_2}\right)^{1/2} P_{O_2}\right)^2}$
2	$H_2 + ** \rightarrow H**H$ $* + O_2 \rightarrow *O_2$ $*O_2 + H**H \rightarrow H**HO_2 + *$ $H**HO_2 \rightarrow H_2O_2 + **$	$r = \frac{k_3 K_{H_2} K_{O_2} P_{H_2} P_{O_2}}{\left(1 + \left(K_{H_2} P_{H_2}\right)^{1/2} + K_{O_2} P_{O_2}\right)^3}$
3	$H_2 + ** \rightarrow H**H$ $** + O_2 \rightarrow **O_2$ $**O_2 + H**H \rightarrow H**HO_2 + **$ $H**HO_2 \rightarrow H_2O_2 + **$	$r = k_3 K_{H_2} K_{O_2} P_{H_2} P_{O_2} \left(\frac{1 + \left(1 + 2K_{H_2} P_{H_2} + 2K_{O_2} P_{O_2}\right)^{1/2}}{K_{H_2} P_{H_2} + K_{O_2} P_{O_2}}\right)^4$
4	$H_2 + * \rightarrow *H_2$ $O_2 + * \rightarrow *O_2$ $*O_2 + *H_2 \rightarrow H**HO_2$ $H**HO_2 \rightarrow H_2O_2 + **$	$r = \frac{k_3 K_{H_2} K_{O_2} P_{H_2} P_{O_2}}{\left(1 + K_{H_2} P_{H_2} + K_{O_2} P_{O_2}\right)^2}$

Table 5.2: Kinetic constants of synthesis reaction at different temperatures.

T, °C	R^2	k	K_{H2}	K_{O2}
		g H_2O_2/g Pd/hr	psi^{-1}	psi^{-1}
35	0.99958	1619.24 ± 141.17	0.0386 ± 0.0061	0.027 ± 0.0035
42	0.99863	1897.68± 317.10	0.0391 ± 0.012	0.025 ± 0.0065
50	0.98668	2424.86± 232.97	0.046± 0.0094	0.021 ± 0.0040

Table 5.3: Arrhenius constants of synthesis reaction

	K	K_{H2}	K_{O2}
Activation or Adsorption energy (kJ/mol)	22.34	10.05	-12.19
Pre-exponential factor	9.81×10^{6} g H_2O_2/g Pd/hr	1.90 psi^{-1}	2.33×10^{-4} psi^{-1}

III.4. Reduction Reaction

The group of Choudhary studied the kinetics of H_2O_2 reduction with different catalysts and with different acid and halide additives (Choudhary et al., 2007a-b). The plots of H_2 consumed *vs.* time were linear until nearly all of H_2O_2 was consumed. From this, the authors concluded that hydrogenation of H_2O_2 was zeroth order with respect to H_2O_2. However, this type of kinetic behavior may also be consistent with a Langmuir-Hinshelwood rate law, where the reaction rate rapidly increases with respect to concentration at low reactant concentrations and becomes nearly constant at high reactant concentrations. A version of kinetics of the DC reactions was described by Melada and co-workers, 2006a, who used a power law rate expression to describe the rates of reaction (1)-(3) with hydrogen concentrations below the explosive limit. Unlike the results of Choudhary et al., 2007a-b, here the reduction reaction had a first-order dependence on H_2O_2 concentration. The difference was probably due to the much lower H_2O_2 concentration achieved by Melada and co-workers than that used for H_2O_2 hydrogenation experiments by the group of Choudhary (0.030 wt% *vs* 0.2 wt%, respectively). Two limitations of first-order rate expressions are that 1) they cannot be used with higher hydrogen concentrations and 2) they are not related to a reaction mechanism.

We isolated the reduction reaction by using a mixture of hydrogen and nitrogen in the feed gas. Decomposition of H_2O_2 (reaction (4)) was completely suppressed in the experiments by 10 ppm NaBr and 1% H_2SO_4 present in the liquid phase. Since the oxidation state of palladium has a strong effect on the rate of H_2O_2 reduction (Choudhary et al., 2007b), the oxidation state of a fresh, unused, catalyst was characterized by XRD (Siemens Diffractometer D5000 with Diffrac-AT 3.2 software). The diffraction pattern showed three peaks characteristic of Pd^0 at 2-theta = 40.0, 46.6, and 68.1°. There was a large hump between 20° and 30° which indicated a large amount of amorphous material, most likely amorphous silica. Thus, there was no evidence of the presence of PdO. This is significant because, according to Choudhary et al., 2007b, the rate of H_2O_2 reduction on Pd^0 is higher than the rate of reduction on PdO by approximately a factor of two in an acid-free solution. However, Pd was most likely oxidized by H_2O_2 in the course of the experiments as shown by the effect of H_2O_2 concentration on catalyst activity. This can be

confirmed by measuring XRD spectra of the fresh and used catalyst, which may be done in future research.

We considered two likely Langmuir-Hinshelwood mechanisms of H_2O_2 reduction, both shown in Table 5.4. The first mechanism was proposed by Choudhary and Samanta, 2006, and the second was proposed by our group. The surface reaction steps (step 3 of each mechanism) were assumed to be rate-determining because the reaction rate depended on the concentration of both H_2 and H_2O_2. The rate expressions derived with the assumption of one of the adsorption steps to be rate-determining did not have the concentrations of both H_2 and H_2O_2 in the equation. The adsorption steps were assumed to be in quasi-equilibrium described by an adsorption constant K_A for each reactant *A*. All kinetic parameters were assumed to follow the Arrhenius relationship, $K_i = A_i e^{-\frac{E_i}{RT}}$.

The kinetic data were regressed by nonlinear regression using the Levenberg-Marquardt algorithm to obtain values of the kinetic parameters for both mechanisms with their 95% confidence intervals (Table 5.5A-B). Three goodness-of-fit parameters are shown in Table 5.5C: adjusted R^2, *F*, and *P* value. R_{adj}^2 is a fraction of the variations in experimental data that is predicted by the model and adjusted for the number of degrees of freedom. The *F* value is a ratio of the variation in the dependent variable due to the independent variable to the random variation in the independent variable. The *P* value is the probability of being wrong in concluding that there is an association between the dependent and independent variables. The statistical parameters are very similar for both mechanisms and imply that each model is equally likely to explain the kinetic data. However, mechanism 2 was selected as the best-fitting because the kinetic constants of this rate expression had significantly smaller confidence intervals than those of the rate expression for mechanism 1. The negative heats of adsorption indicate exothermic adsorption, which is more likely than endothermic (Jewell and Davis, 2006).

Table 5.4: Proposed mechanisms and corresponding rate expressions of H_2O_2 reduction.

Mechanism 1	Mechanism 2
$1.\ H_2 + 2* \rightarrow 2H*$ $2.\ H_2O_2 + * \rightarrow H_2O_2*$ $3.\ 2H* + H_2O_2* \rightarrow 2H_2O + 3*$ $R = \frac{kK_{H_2}K_{H_2O_2}P_{H_2}C_{H_2O_2}}{\left(1+\left(K_{H_2}P_{H_2}\right)^{1/2}+K_{H_2O_2}C_{H_2O_2}\right)^3}$	$1.\ H_2 + 2* \rightarrow 2H*$ $2.\ H_2O_2 + 2* \rightarrow 2OH*$ $3.\ 2H* + 2OH* \rightarrow 2H_2O + 4*$ $R = \frac{kK_{H_2}K_{H_2O_2}P_{H_2}C_{H_2O_2}}{\left(1+\left(K_{H_2}P_{H_2}\right)^{1/2}+\left(K_{H_2O_2}C_{H_2O_2}\right)^{1/2}\right)^4}$

Table 5.5: Kinetic constants of the proposed rate expressions and their goodness-of-fit parameters.

	Mechanism 1	Mechanism 2
***k* (g H_2O_2/g Pd/hr)**	$2.526\times10^{11} \pm 2.625\times10^{10}$	$1.565\times10^{11} \pm 2.017\times10^{6}$
K_{H2} (psi^{-1})	$1.835\times10^{-6} \pm 3.488\times10^{-7}$	$2.316\times10^{-6} \pm 5.703\times10^{-11}$
K_{H2O2} ($(mol/l)^{-1}$)	0.076 ± 0.0173529	$0.195 \pm 5.647\times10^{-6}$

	Mechanism 1	Mechanism 2
E_a (kJ/mol)	45.25 ± 0.27	43.71 ± 0.034
$\Delta H_{K_{H2}}$ (kJ/mol)	-24.88 ± 0.51	-23.08 ± 0.065
$\Delta H_{K_{H2O2}}$ (kJ/mol)	-6.59 ± 0.60	-4.68 ± 0.076

	R^2_{adj}	***F***	***P***
Mechanism 1	0.9360	80.80	<0.0001
Mechanism 2	0.9362	81.13	<0.0001

The validity of rate expression 2 was verified by comparing the predicted space-time yields with experimental space-time yields obtained in an integral reactor. The experimental values were in close agreement with the calculated values. The conversions of H_2O_2 used for the comparison were in the range of 15-34%. Higher conversions were not used because the velocities required for higher conversions were low enough for the reaction to become controlled by external mass transfer. The presence of an external mass transfer limitation at low velocities was demonstrated, where the conversions obtained at decreasing velocities were compared with predicted conversions. The increasing discrepancy between the experimental and predicted points must be due to the reaction entering the external mass transfer-controlled regime. An attempt to increase the conversions by increasing the catalyst loading was not successful because of excessively high pressure drop.

A drawback of these experiments is the absence of oxygen in the gas phase. The rate expression obtained here may be inaccurate for use in a simulation of a DC process if the rate of reduction is affected by the presence of oxygen. This may be the case if, for example, the oxygen

oxidizes Pd to PdO in the course of the reaction. However, this is unlikely because the temperatures used for the DC process are too low for oxidation of palladium by oxygen (Hill, 2002; McCabe, 2001). This question will be resolved by comparing the experimental reactor performance for formation of H_2O_2 with the results predicted by the overall reactor model that includes the rate expressions for H_2O_2 synthesis, reduction and decomposition.

III.5. Decomposition Reaction

H_2O_2 decomposition (reaction (4)) is inhibited by the presence of acids in the reaction medium, particularly H_2SO_4, H_3PO_4, and HCl (Choudhary, et al. 2006b). The inhibition effect of acids is attributed to the formation of a bond between protons and H_2O_2, which would give H_2O_2 a partial positive charge and prevent it from adsorbing onto the catalyst (Choudhary and Samanta, 2006). Acids and halides promote the formation of H_2O_2 when either is present in the reaction medium. However, when both an acid and a halide are present, the promoting effect is greater than the individual effect of either compound. This is due to the greater efficacy of halides in suppressing the decomposition of H_2O_2 in the presence of acid: the suppressing effect of halides was greater by approximately a factor of three in acidic solution than in pure water. It has been proposed that the protons enhance the effect of halides by decreasing the pH below the isoelectric point of the catalyst support, so that the catalyst surface becomes positively charged and the halide anions are much more likely to be adsorbed onto the catalyst, where they inhibit the H_2O_2 consumption reactions. Thus, the promoting effect of acid on H_2O_2 productivity has been well established. However, hydrogen peroxide in an acidic solution is not desirable for a number of applications where H_2O_2 is currently used, such as soil remediation and cloth bleaching. In such cases, the DC process must be operated using a solvent that is either acid-free or with a very low acidity.

For this project, our goal was to propose a plausible mechanism for the decomposition of H_2O_2 over Pd/SiO_2 catalyst and from that obtain a broadly applicable rate expression for this reaction. Decomposition of hydrogen peroxide is a widely studied reaction and a number of studies were done on decomposition catalyzed by palladium on a variety of supports, for example (Beena et al., 1996; Barteri et al., 1978; Potekhin et al., 2005; Salem et al., 2000; Choudhary and Gaikwad, 2003). In the literature, the ranges of H_2O_2 concentration covered were typically less than 1 mol/l and the heterogeneously catalyzed decomposition reaction was always found to follow first-order kinetics with respect to H_2O_2. A first-order rate expression would not adequately describe the data at higher concentrations of H_2O_2 because mechanisms of heterogeneously catalyzed reactions are typically of Langmuir-Hinshelwood (L-H) type (Davis and Davis, 2003). At low concentrations, L-H rate expressions can usually be simplified to first-order rate expressions. Since our goal was to model a microreactor for production of up to 1.5 mol/l H_2O_2 (5% w/w), we performed kinetic experiments at sufficiently high concentrations of H_2O_2 to find a Langmuir-Hinshelwood rate expression for this reaction. In addition, we aimed to quantify the effect of sulfuric acid on the rate of decomposition by comparing the L-H kinetic constants at two different acid concentrations. A study by Choudhary and co-workers, 2003, looked at first-order kinetics for H_2O_2 decomposition at different concentrations of H_2SO_4 on Pd/C catalyst. The researchers found that the activation energy decreased from 17.65 to 17 kJ/mol, and the pre-exponential factor decreased from 107.2 to 61.7 min^{-1} as the acid concentration was varied from 0 to 10 mol/l (approximately 98% w/w). However, no halides were used in the reaction medium, which makes their result not comparable to the present work. As described above, the combined inhibiting effect of sulfuric acid and halide anions is much greater than the individual effect of each. In this project, all decomposition experiments were

carried out in the presence of 10 ppm NaBr in order to obtain rate expressions that are compatible with the previously obtained kinetics of synthesis and reduction of hydrogen peroxide. The rate expression of the decomposition reaction was determined by carrying out kinetic experiments with only air in the gas phase and a liquid phase with concentrations of H_2SO_4 that were sufficiently small for a significant amount of decomposition to take place.

We proposed a cyclic Pd oxidation/reduction mechanism for the decomposition reaction (equations 4 and 5 of Table 5.6) and derived a rate expression based on this mechanism (rate expression 5 of Table 5.6B). Values for the kinetic parameters of rate expression 5 were obtained by non-linear regression of experimental data (Table 5.7). The proposed mechanism was supported by a close agreement between the experimental and predicted reaction rates in both acid-free and acidic solutions, as well as the observations of Choudhary and Samanta, 2007, and Choudhary et al., 2006b described above. An unambiguous proof of the mechanism, however, requires detailed surface studies of the catalyst, which may be done as part of future research.

The rates of decomposition in 0.05% (w/w) H_2SO_4 were lower than those in acid-free solution by approximately one order of magnitude, when both sets of experiments were done with 10 ppm NaBr in the reaction medium. This difference was much greater than the difference between rates of decomposition in acid-free and acidic halide-free solutions obtained from the literature. The difference was attributed to the presence of NaBr. Isothermal kinetic parameters were found to decrease in an inverse exponential relationship with respect to the concentration of H_2SO_4. This relationship was verified by comparing the experimental and predicted rates of decomposition between 0 and 0.2 wt% H_2SO_4. However, further research is needed to confirm this relationship because it was determined using only three H_2SO_4 concentration points. The inverse exponential relationship is purely empirical and further study is needed to relate it to the mechanism of interactions between the acid, bromide, hydrogen peroxide, and the catalyst. It was found that a H_2SO_4 concentration of about 0.1% was sufficient to significantly suppress H_2O_2 decomposition over Pd/SiO_2 catalyst.

Tables 5.6A-B: Proposed mechanisms of H_2O_2 decomposition with rate expressions that correspond to each mechanism step as rate-limiting. Parameters k_i and K_i are the rate constants and equilibrium coefficients (respectively) that correspond to step *i* of a mechanism. * = Pd catalytic site

Table 5.6A: Radical mechanism of Choudhary and Samanta, 2006.

Step	Limiting Rate Expression	Rate Expr. No.
1) 2 H_2O_2 + 4* $\rightarrow$ 4*OH	$r = \dfrac{k_1 C_{H_2O_2}{}^2}{\left(1+\left(K_3 C_{O_2}\right)^{1/2} + C_{H_2O}{}^{1/2}\left(\dfrac{K_3}{K_2}C_{O_2}\right)^{1/4}\right)^4}$	1
2) 4*OH $\rightarrow$ 2H_2O +2*O + 2*	$r = \dfrac{k_2}{\left(\dfrac{1}{K_1^{1/4} C_{H_2O_2}{}^{1/2}} + \dfrac{1}{K_1^{1/4}}\left(\dfrac{C_{O_2}}{K_3 C_{H_2O_2}}\right)^{1/2} + 1\right)^4}$	2

3) $2^*O \rightarrow O_2 + 2^*$	$r = \dfrac{k_3}{\left(1 + \dfrac{C_{H_2O}}{(K_1K_2)^{1/2} C_{H_2O_2}} + \dfrac{C_{H_2O}}{K_1^{1/4} K_2^{1/2} C_{H_2O_2}^{1/2}}\right)^2}$	3

Table 5.6B: Cyclic Pd oxidation/reduction mechanism.

Step	Limiting Rate Expression	Rate Expr. No.
1) $* + H_2O_2 \rightarrow *O + H_2O$	$r = \dfrac{k_1 C_{H_2O_2}}{1 + \dfrac{C_{H_2O} C_{O_2}}{K_2 C_{H_2O_2}}}$	4
2) $*O + H_2O_2 \rightarrow * + H_2O + O_2$	$r = \dfrac{k_2 C_{H_2O_2}}{1 + \dfrac{C_{H_2O}}{K_1 C_{H_2O_2}}}$	5

Table 5.7: Isothermal kinetic constants for the two potential rate expressions. *k*: g/g Pd/hr; K_1: (l/mol)^2 for rate expression 3, l/mol for rate expression 5; K_2: (l/mol)^2.

	T, ºC	Rate expression 3	Rate expression 5
k	30	39.71 ± 3.91	37.72 ± 0.76
	40	91.49 ± 3.72	74.51 ± 0.82
	50	265.50 ± 29.23	178.93 ± 0.62
K_1	30	709.47 ± 3860.08	66.41 ± 2.45
	40	294.40 ± 70.72	84.99 ± 2.05
	50	461.40 ± 616.50	101.99 ± 0.84
K_2	30	399.48 ± 1390.27	
	40	592.08 ± 94.27	
	50	290.24 ± 252.35	

III.6. Overall Reaction

The kinetic rate expressions determined in separate experiments, as described above, were used to set up a model of the Direct Combination reactor where all four of the reactions in Scheme 1 are taking place simultaneously. The direct formation of water (reaction (2)) could not be isolated because water was used as the liquid solvent. However, the rate of this reaction was negligible when the conversion of reactants was small because, under these conditions, the selectivity for hydrogen peroxide was 100%. It is likely that hydrogen peroxide was the initial product for high reactant conversions as well; however we cannot be certain *a priori*. The only way to account for the direct formation of water is to initially assume that the rate of this reaction

is negligible. If there is a good correspondence between the predicted and experimental values, then the initial assumption will be confirmed. However, if the conversions of reactants are consistently higher than predicted, then the difference is most likely due to direct water formation.

III.6.1. Reactor Model

The overall rate of formation of H_2O_2 can be calculated from Equation 5.6:

$$r_{H_2O_2,ov} = r_1 - r_3 - r_4 \tag{5.6}$$

A mathematical model of the microreactor had to be developed prior to using Equation 5.6 to predict the reactor performance. The model had to include mass transfer effects because the rate of H_2O_2 reduction is controlled by the rate of external mass transfer at the low flow velocities required to produce hydrogen peroxide at commercial concentrations of about 1% (w/w). The set of equations we derived is similar to the equations used by Nijhuis and co-workers (2003) to model hydrogenation of styrene in a monolith reactor, as well as to those used by Tadepalli and co-workers (2007) to model hydrogenation of nitroanisole in the same type of microreactor as used in this work. The mass transfer steps that take place in the microreactor have been shown in Figure 5.4. The flow regime is Taylor flow, where liquid slugs with well-defined boundaries alternate with gas slugs.

The following assumptions are implicit in the model:

1) The H_2O_2 synthesis reaction takes place as H_2 and O_2 diffuse from the gas phase directly onto the catalyst surface through a thin liquid film. This assumption is justified because the synthesis reaction is not limited by gas-liquid mass transfer at the velocities used in experiments described in this project.
2) The mass transfer rate of hydrogen diffusing into the liquid slug prior to the reduction of H_2O_2 is taken into account by the product of the gas-liquid mass transfer coefficient and the gas-liquid interface area, $k_{gl}a_{gl}$. This quantity will be referred to as the mass transfer parameter. Thus, the reduction of H_2O_2 is the only reaction in Scheme 1 that is controlled by external mass transfer at the flow velocities considered in this work.
3) The amount of H_2O_2 formed from the H_2 and O_2 dissolved in bulk liquid is negligible compared to the amount formed from H_2 and O_2 that diffuse directly from the gas phase onto the catalyst surface through a thin liquid film.
4) There is no difference between reaction rates in liquid slugs and in gas slugs. In other words, this is a pseudo single-phase model. The modeling of different reaction rates in gas and liquid slugs would involve the use of step functions, or Heavyside functions. Such a model would require the knowledge of liquid and gas slug lengths, which is not available for a packed-bed microreactor. The benefit of such a detailed model would be the ability to compute a concentration profile over the reactor length that takes into account the concentration differences between gas and liquid slugs. There was, however, no need for such a detailed simulation at this time because our goal in the project was to be able to predict the composition of gas and liquid phases at the reactor's exit. This was done by calculating a concentration profile that did not take into account the difference in reaction rates between the gas and the liquid phases. The mass transfer rate of hydrogen into the liquid phase, determined by the parameter $k_{gl}a_{gl}$, is strongly affected by the lengths of gas and liquid slugs (Nijhuis et al., 2003., Kreutzer et al., 2001). However, the assumption of a pseudo single-

phase model enabled us to calculate $k_{gl}a_{gl}$ without the knowledge of slug lengths, as shown in the model equations below.

5) The liquid-solid mass transfer parameter $k_{ls}a_{ls}$ was estimated, using the correlations for monolith reactors (Nijhuis et al., 2003., Kreutzer et al., 2001), to be approximately one order of magnitude greater than the gas-liquid mass transfer parameter. This was expected since gas-liquid-solid reactions are usually not limited by liquid-solid mass transfer.

The mass transfer steps considered by the model are summarized in Figure 5.7. The mass balances of reactants and products are given in Equations 5.7 – 5.9:

$$\frac{dF_{H_2}}{dz} = \frac{a}{MW_{H_2O_2}}\left(-r_1 - r_2 - r_3\right) \tag{5.7}$$

$$\frac{dF_{O_2}}{dz} = \frac{a}{MW_{H_2O_2}}\left(-r_1 - 0.5r_2 + 0.5r_4\right) \tag{5.8}$$

$$\frac{dF_{H_2O_2}}{dz} = \frac{a}{MW_{H_2O_2}}\left(r_1 - r_3 - r_4\right) \tag{5.9}$$

where F_i is the molar flow rate of compound i, z is the length of reactor, and a is the weight of catalyst per unit length of reactor. The direct formation of water (r_2) is neglected, as described above.

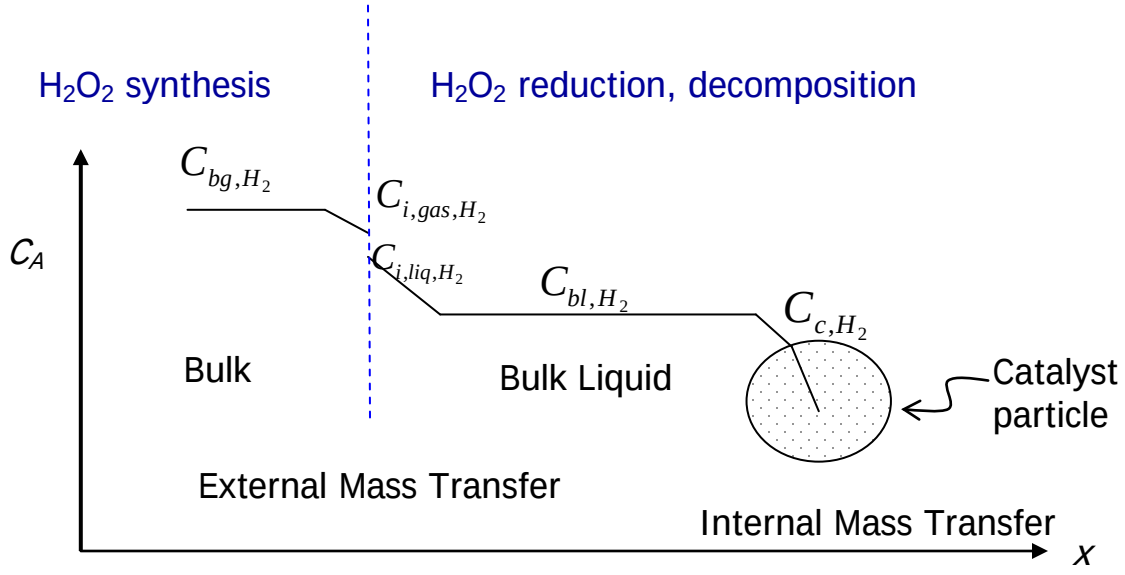

Figure 5.7: Schematic of mass transfer steps considered by the reactor model.

The reactor model equations are as follows:

Hydrogen in bulk liquid

$$v_l \frac{dC_{bl,H_2}}{dz} = k_{gl}a_{gl}(C_{sat,H_2} - C_{bl,H_2}) + k_{ls}a_{ls}(C_{c,H_2} - C_{bl,H_2}) \quad (5.10)$$

Hydrogen at catalyst surface

$$k_{ls}a_{ls}(C_{bl,H_2} - C_{c,H_2}) = c\rho_{cat}r_{H_2O_2,red} \quad (5.11)$$

H_2O_2 in bulk liquid

$$v_l \frac{dC_{c,H_2O_2}}{dz} = c\rho_{cat}\left(r_{H_2O_2,syn} - r_{H_2O_2,red} - r_{H_2O_2,dec}\right) \quad (5.12)$$

Hydrogen in bulk gas

$$v_l \frac{dC_{bg,H_2}}{dz} = k_{gl}a_{gl}(C_{bl,H_2} - C_{sat,H_2}) - c\rho_{cat}r_{H_2O_2,syn} \quad (5.13)$$

Oxygen in bulk gas

$$v_l \frac{dC_{bg,O_2}}{dz} = c\rho_{cat}\left(-r_{H_2O_2,syn} + 0.5r_{dec}\right) \quad (5.14)$$

$$r_{H_2O_2,red} = \frac{k_{red}K_{H_2,red}K_{H_2O_2,red}P_{H_2}C_{H_2O_2}}{\left(1+\left(K_{H_2,red}P_{H_2}\right)^{1/2}+\left(K_{H_2O_2,red}C_{H_2O_2}\right)^{1/2}\right)^4} \quad (5.15)$$

$$r_{H_2O_2,syn} = \frac{k_{syn}K_{H_2,syn}K_{O_2,syn}P_{H_2}P_{O_2}}{\left(1+K_{H_2,syn}P_{H_2}+K_{O_2,syn}P_{O_2}\right)^2} \quad (5.16)$$

$$r_{H_2O_2,dec} = \frac{k_{dec}C_{H_2O_2}}{1+\dfrac{C_{H_2O}}{K_{dec}C_{H_2O_2}}} \quad (5.17)$$

where $\ln(k_{dec}) = m_k C_{H_2SO_4} + b_k$ *and* $\ln(K_{dec}) = m_K C_{H_2SO_4} + b_K$

An important drawback of the reactor model in Equations 5.10 – 5.17 is that the gas flow rates are not taken into account. The only flow rate in the equation is that of the liquid phase. Since the volumetric flow rate of the gas is much higher than that of the liquid, the gas flow rate has a much higher effect on the residence time. Thus this model is only valid at the gas/liquid ratio of 440 (at standard temperature and pressure), which was the ratio throughout all the kinetic experiments used to obtain the rate expressions in Equations 5.15 – 5.17.

III.6.2. Results and Discussion

III.6.2.1. Gas-Liquid Mass Transfer Parameter

The flow velocities used in the experiments in this portion of the project (4-10 cm/s) were much lower than those used for the kinetic experiments (10-40 cm/s) in order to increase the residence time in the reactor, which allowed us to produce up to 1 wt% hydrogen peroxide. As mentioned above, the reduction reaction is controlled by external mass transfer at low flow velocities. Thus, the value of $k_{gl}a_{gl}$ must be determined in order to be able to model the microreactor. This was

done by carrying out the reduction reaction at variable velocities in the mass transfer-controlled regime and comparing the experimental space-time yields with those calculated by Equations 5.10 – 5.17. (Since only the reduction reaction was considered here, the reaction rates $r_{H_2O_2,syn}$ and $r_{H_2O_2,dec}$ in Equations 5.12 – 5.17 were set to zero during the calculations). The values of the kinetic constants of the rate expressions in Equations 11-14, as well as the most likely reaction mechanisms, were determined in separate experiments in the kinetically-controlled regime, as described in previous sections of this activity. The values of $k_{gl}a_{gl}$ were chosen by trial and error, such that the calculated reaction rates were within less than 5% of experimental data. The system of differential equations was solved using Athena Visual Workbench software. Figure 5.8 shows $k_{gl}a_{gl}$ values calculated at various velocities. The mass transfer coefficient increases with velocity, as expected for a reaction limited by external mass transfer (Kreutzer et al., 2001). The range of mass transfer parameters is similar to that obtained by Tadepalli et al. (2007).

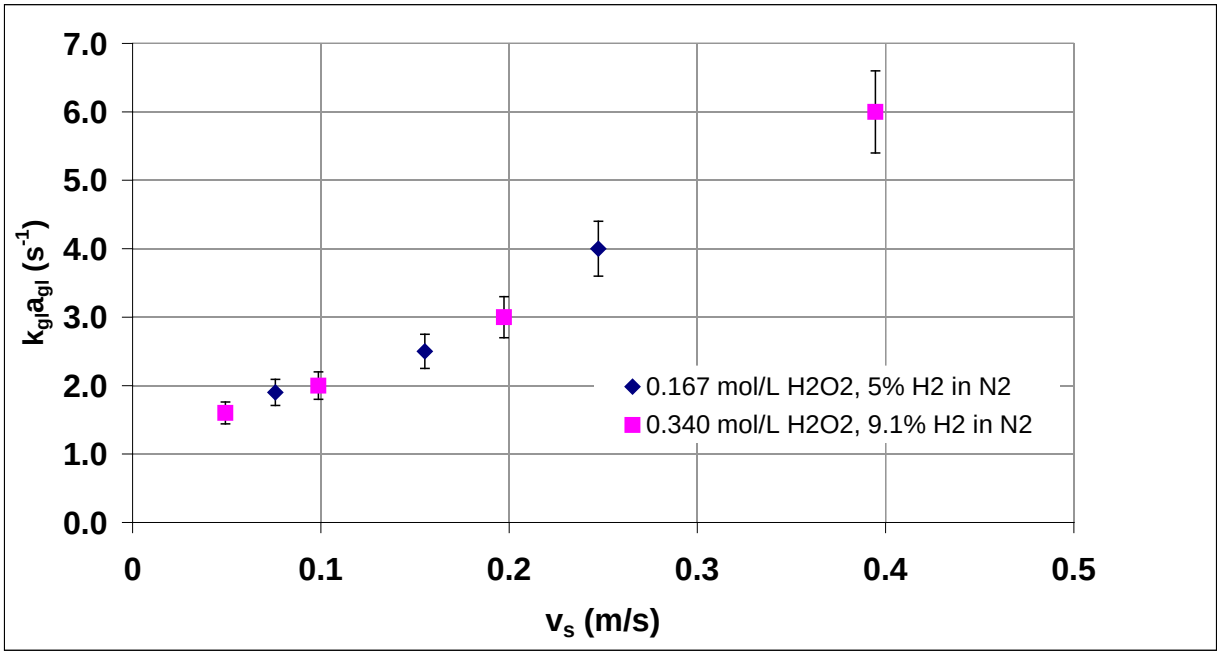

Figure 5.8: Effect of total flow velocity on $k_{gl}a_{gl}$.
Operating conditions: **T = 42 ºC, P = 300 psig, gas phase as specified in legend, liquid phase: 1% H_2SO_4 and 10 ppm NaBr in DI water with H_2O_2 concentration as specified in legend.**

III.6.2.2. Verification of Reactor Model

The mass transfer parameters in Figure 5.8 were used with Equations 5.7–5.14 to model the performance of the microreactor under conditions where the reactions in Scheme 1 are taking place simultaneously. Figures 5.9–5.13 compare the predicted reactor performance with experimental values at variable catalyst loadings, pressures and velocities (at constant residence times), and temperatures. The results show a good correspondence between the experimental and predicted points with typical discrepancies of less than 10%. The experimental and predicted points showing the effect of temperature in Figure 5.10 have a greater discrepancy than typical for the other graphs. This must be due to the slightly lower activity of the catalyst batch used to obtain this set of data. Particularly interesting is the case of variable velocity in Figure 5.13, where the residence time was kept constant. These data were used in the previous section on H_2O_2 synthesis to show the lack of an external mass transfer limitation for the synthesis reaction

because the space-time yield did not increase with velocity. At that time, the slight decrease in reaction rates with velocity was attributed to experimental error. However, the calculated values show that the decreases in space-time yields and selectivities are due to the increase of gas-liquid mass transfer coefficients with velocity, which leads to an increasing rate of H_2O_2 reduction.

In Figure 5.14, we can see the effect of sulfuric acid concentration on the rate of H_2O_2 formation, while all the other factors that may affect the space-time yield were kept constant. Sulfuric acid has a strong effect on the rate of H_2O_2 decomposition, which is taken into account in Equation 5.17. H_2O_2 reduction is not affected by sulfuric acid, however, the effect of sulfuric acid on the synthesis of H_2O_2 (reaction (1) in Scheme 1) has not been determined. The close correspondence between the measured and calculated points in Figure 5.14 shows that the synthesis reaction is not significantly affected by the concentration of sulfuric acid.

Figure 5.15A shows the calculated concentration profile obtained for the conditions that correspond to those used for experiments in Figure 5.9, together with the experimental points from Figure 5.9. We can see than the concentration of H_2 in the bulk liquid is much lower than the saturation concentration (*i. e.* the concentration in equilibrium with the bulk gas) throughout most of the reactor length, which shows that the gas-liquid mass transfer of H_2 is controlling the reaction rate. The reaction affected by this mass transfer limitation is the reduction of H_2O_2 because this is the only reaction where H_2 dissolved in the liquid is one of the reactants. Figure 5.15B shows the calculated concentration profile under the same conditions as in Figure 5.15A, except that the two-phase flow velocity was increased by a factor of about five. Now, the gas-liquid mass transfer limitation is not significant any more, which leads to higher rates of reduction, so that the maximum H_2O_2 concentration obtained here is lower by a factor of about three, than that obtained in the low-velocity reactor simulated in Figure 5.15A.

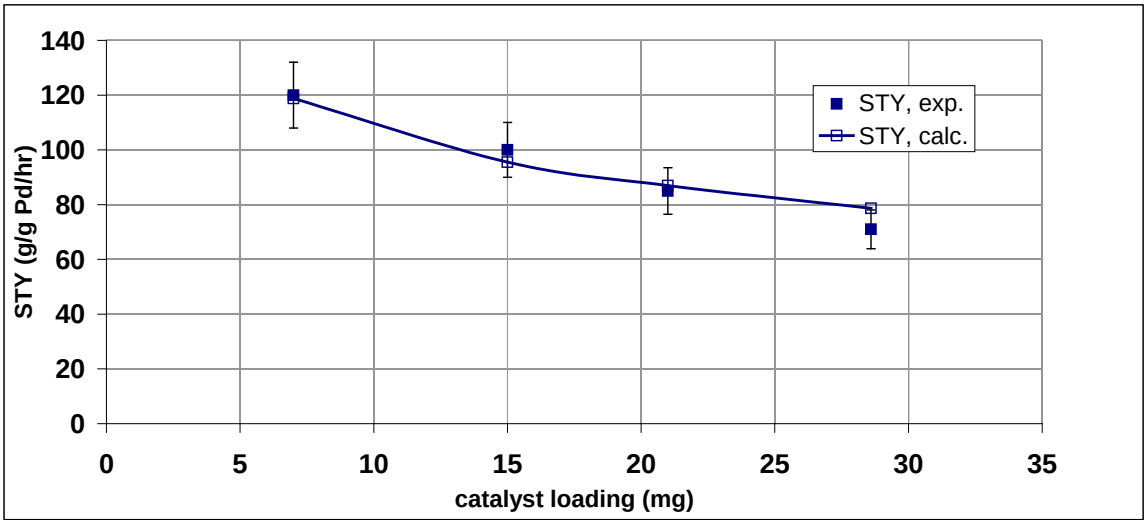

Figure 5.9: Comparison of experimental and calculated space-time yields at various catalyst loading levels. *Operating conditions*: T = 42 ºC, P = 300 psig, gas phase: 9.1% H_2 in air, liquid phase: 1% H_2SO_4 and 10 ppm NaBr in DI water.

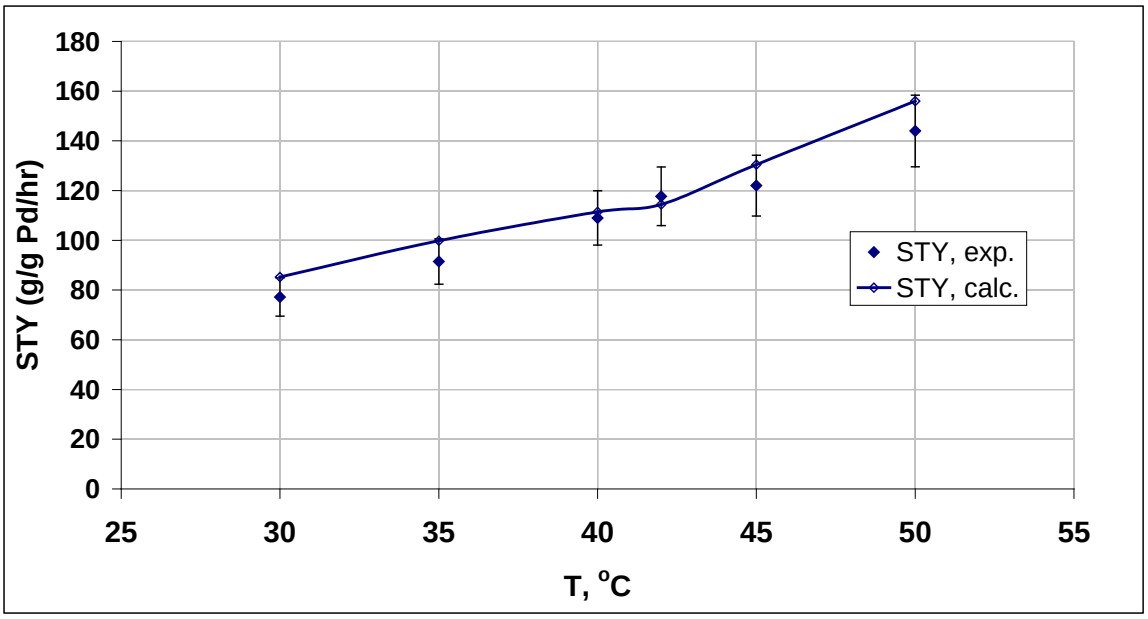

Figure 5.10: Comparison of experimental and calculated space-time yields at various temperatures. *Operating conditions*: P = 300 psig, 7 mg of catalyst, gas phase: 9.1% H_2 in air, liquid phase: 1% H_2SO_4 and 10 ppm NaBr in DI water.

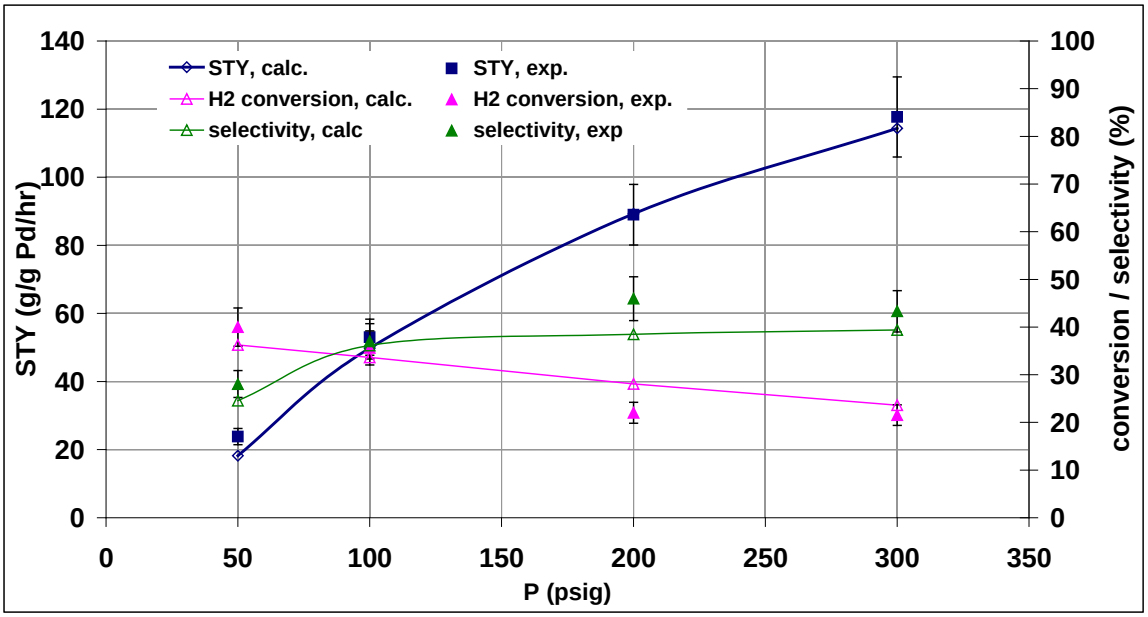

Figure 5.11: Comparison of experimental and calculated reactor performance at various total pressures. *Operating conditions*: T = 42 °C, gas phase: 9.1% H_2 in air, liquid phase: 1% H_2SO_4 and 10 ppm NaBr in DI water, residence time = 0.78 sec.

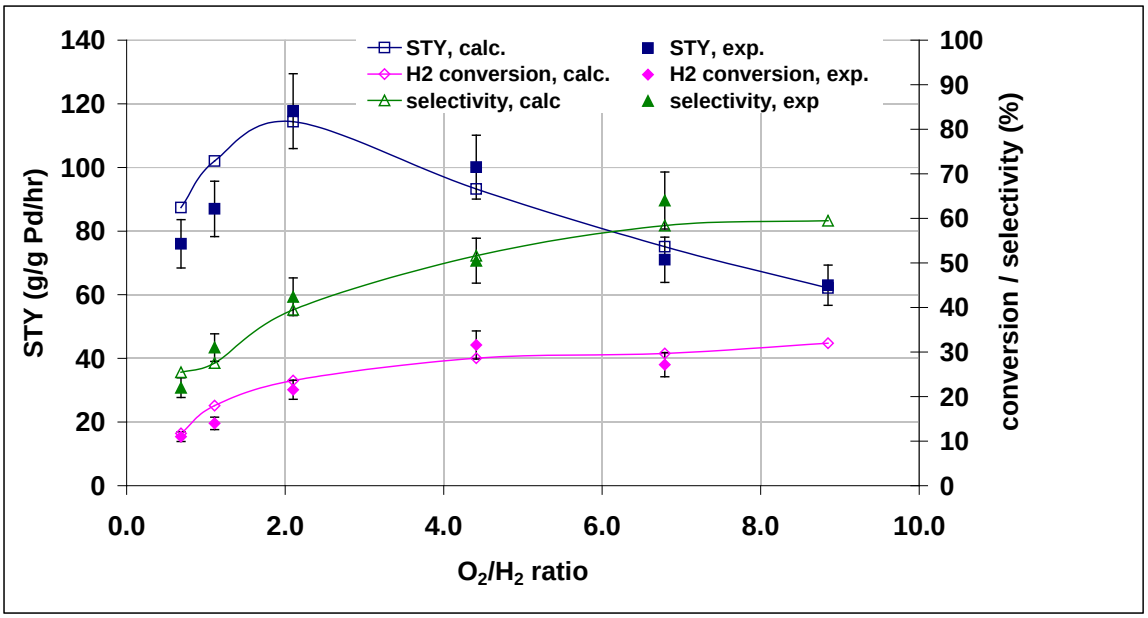

Figure 5.12: Comparison of experimental and calculated space-time yields and conversions at various gas compositions. *Operating conditions*: P = 300 psig, T = 42 °C, 7 mg of catalyst, gas phase: air with specified hydrogen composition, liquid phase: 1% H_2SO_4 and 10 ppm NaBr in DI water.

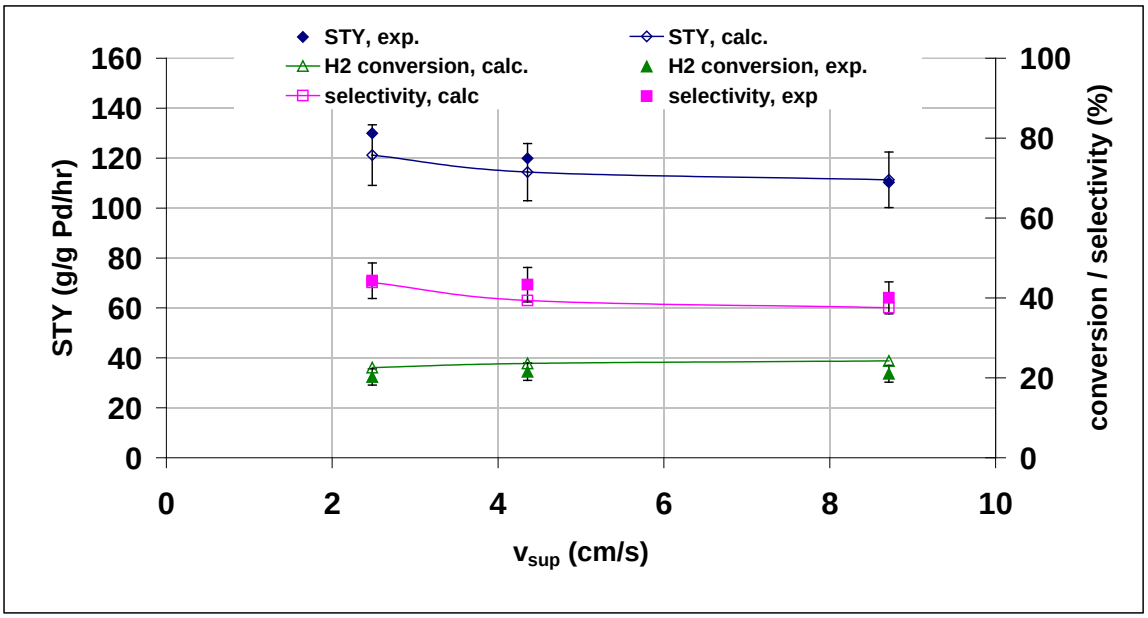

Figure 5.13: Comparison of experimental and calculated space-time yields and conversions at various total superficial flow velocities. *Operating conditions*: P = 300 psig, T = 42 °C, gas phase: 9.1% H_2 in air, liquid phase: 1% H_2SO_4 and 10 ppm NaBr in DI water, residence time = 0.78 sec.

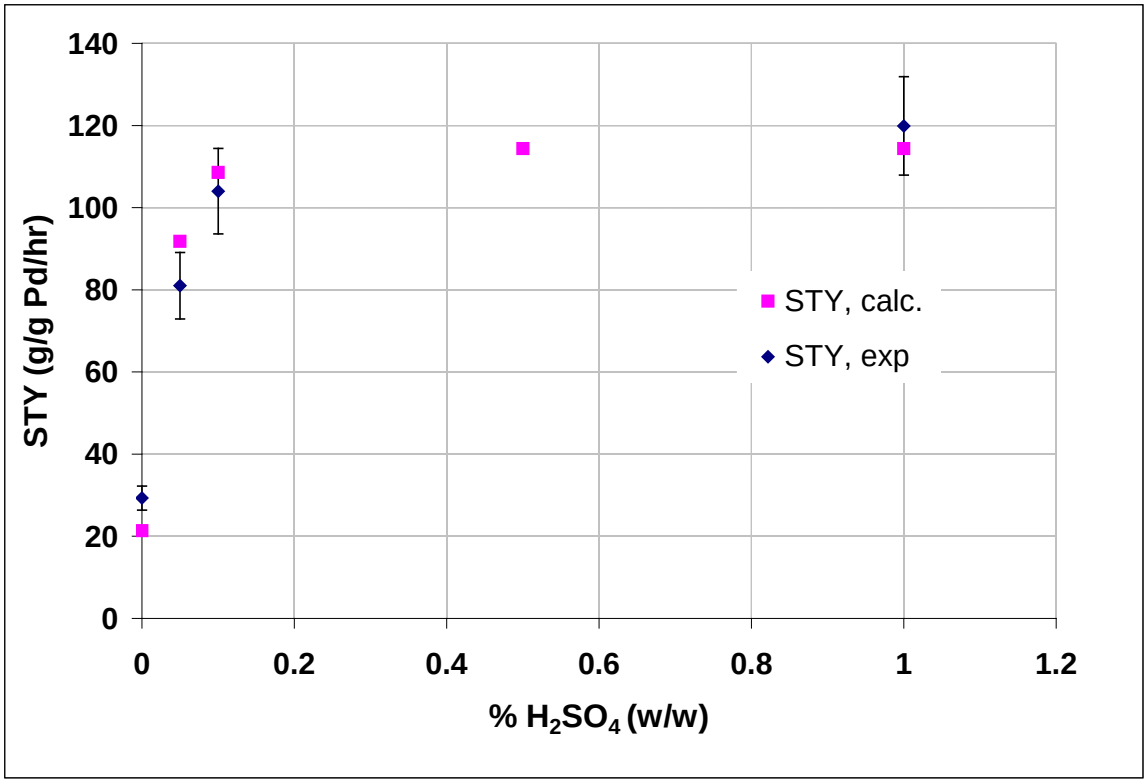

Figure 5.14: Comparison of experimental and calculated space-time yields at various concentrations of sulfuric acid. *Operating conditions*: P = 300 psig, T = 42 ºC, 7 mg of catalyst, gas phase: 9.1% H_2 in air, liquid phase: 10 ppm NaBr in DI water with specified concentration of H_2SO_4.

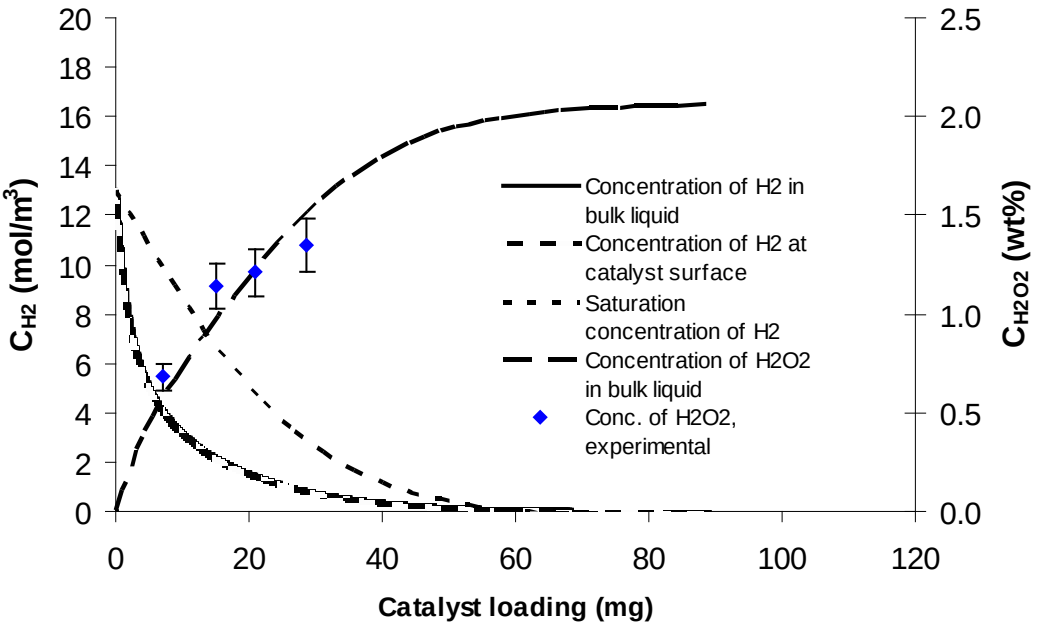

A.

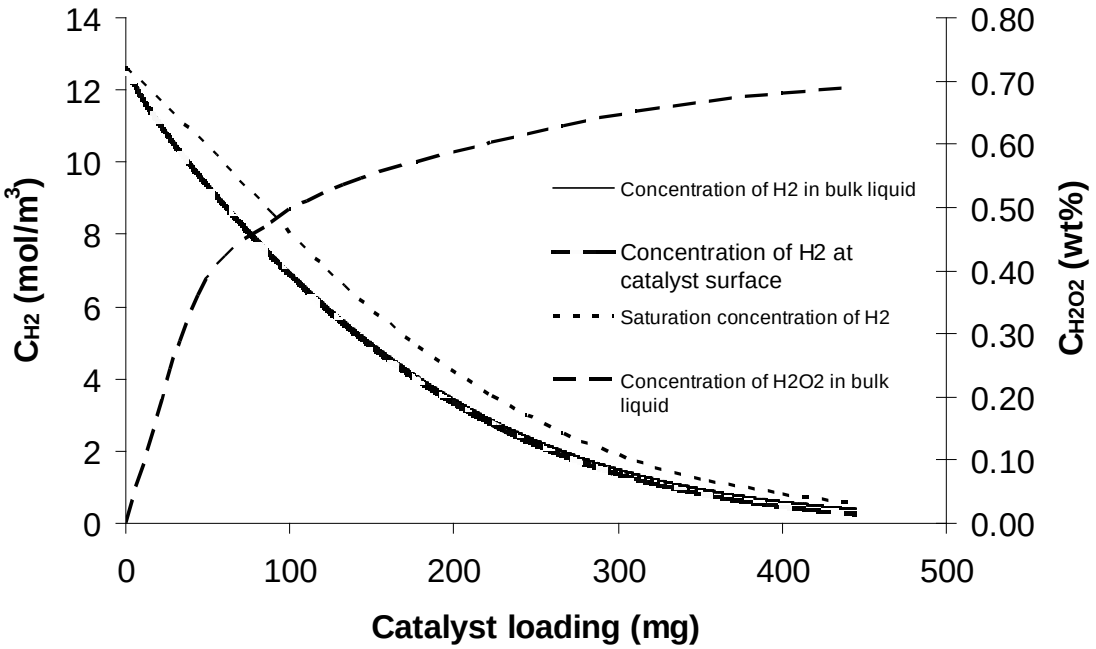

B.

Figure 5.15A-B: Calculated concentration profiles at various two-phase flow velocities. Operating conditions: P = 300 psig, T = 42 ºC, gas phase: 9.1% H_2 in air, liquid phase: 1% H_2SO_4 and 10 ppm NaBr in DI water. A) Two-phase flow velocity = 0.11 m/s, $k_{gl}a_{gl}$ = 1.7 s^{-1}. B) Two-phase flow velocity = 0.52 m/s, $k_{gl}a_{gl}$ = 7 s^{-1}.

The most likely sources of discrepancies between experimental and predicted reactor performance are:

1) Different batches of catalyst were used for each series of kinetic experiments (H_2O_2 synthesis, decomposition and reduction), as well as for the model verification experiments.
2) Kinetic experiments used to obtain the rate expression for H_2O_2 reduction were carried out in an oxygen-free atmosphere. Since the oxidation state of palladium has a significant effect on the rate of reduction (Choudhary et al., 2006, 2007), the reduction rates predicted by this rate expression may be slightly different from the actual rates in the presence of oxygen.
3) If the direct formation of water were significant, then it would have caused the measured conversions of hydrogen and oxygen, as well as the space-time yields of H_2O_2, to be greater than those calculated using equations 5.10–5.17.
4) As described above, the rate expressions in Equations 5.15–5.17 were determined for each reaction separately by isolating the reaction. It was impossible to know in advance whether these rate expressions would still be valid with all three reactions taking place simultaneously. A change in the kinetics of one of the three reactions may have been the cause of a discrepancy between the measured results and the results predicted by the reactor model.

The closeness of experimental and predicted reactor performance implies that none of these factors was significant. Thus, the model has aided the clarification of certain important aspects of Direct Combination chemistry.

III.6.3. Conclusions

The overall rate expression of hydrogen peroxide formation is a tool that enables us to model and design a microreactor for production of hydrogen peroxide by the direct combination method. We obtained the overall kinetics of this reaction by combining the rate equations for H_2O_2 synthesis, H_2O_2 reduction, and H_2O_2 decomposition by disproportionation. Gas-liquid mass transfer parameters were measured over a range of velocities in order to model the microreactor in the mass transfer-controlled regime. Space-time yields of H_2O_2 and conversions of reactants were measured at various catalyst loadings, temperatures, operating pressures, O_2/H_2 ratios and residence times. These are all the parameters needed to fully specify a direct combination process for H_2O_2 production. Experimental data points were acceptably close to the calculated points, thus verifying the reactor model and the rate equations. The model can be used to calculate the optimum operating conditions for this process, as well as to predict the performance of the microreactor at a given set of conditions. Furthermore, the model clarified the following aspects of the chemistry of the direct combination process: 1) direct formation of water is negligible with 10 ppm NaBr in the liquid phase, 2) the rate of H_2O_2 reduction is not affected by the presence of O_2, and 3) the rate of H_2O_2 synthesis is not affected by the acidity of the liquid phase.

III.7. References

Barteri, M., M. Farinella, B. Pispisa. Dual- vs single-active site mechanism in the catalytic decomposition of hydrogen peroxide. *J. Inorg, Nucl. Chem.,* 40 (1978), 277-1278.

Beena, B., A. Shivanekar, U. Chudasama. Catalytic activity of Pd(II) sorbed on an inorganic ion exchanger zirconium molybdate. *Journal of Molecular Catalysis A: Chemical,* 107 (1996), 347-350.

Bercic, G., and Pintar, A.. The role of gas bubbles and liquid slug lengths on mass transport in Taylor flow through capillaries. *Chemical Engineering Science,* 52 (1997), 3709-3719.

Burch, R., and P. R. Ellis. An investigation of alternative catalystic approaches for the direct synthesis of hydrogen peroxide from hydrogen and oxygen. *Applied Catalysis B: Environmental,* 42 (2003), 203-211.

Chinta, S., and J. H. Lunsford. A mechanistic study of H_2O_2 and H_2O formation from H_2 and O_2 catalyzed by palladium in an aqueous medium. *Journal of Catalysis*, 225 (2004), 249–255.

Choudhary, V. R., and A. Gaikwad. Kinetics of hydrogen peroxide decomposition in aqueous sulfuric acid over palladium/carbon: effect of acid concentration. *Reaction Kinetics and Catalysis Letters,* 80 (2003), 27-32.

Choudhary, V.R. and C. Samanta. Role of chloride or bromide anions and protons for promoting the selective oxidation of H_2 by O_2 to H_2O_2 over supported Pd catalysts in an aqueous medium. *Journal of Catalysis,* 238 (2006), 28-38.

Choudhary, V.R., C. Samanta, T.V. Choudhary. Direct oxidation of H_2 to H_2O_2 over Pd-based catalysts: Influence of oxidation state, support and metal additives. *Applied Catalysis A: General*, 308 (2006a), 128–133.

Choudhary, V. R., C. Samanta, T.V. Choudhary. Factors influencing decomposition of H_2O_2 over supported Pd catalyst in aqueous medium. *Journal of Molecular Catalysis A: Chemical*, 260 (2006b), 115–120.

Choudhary, V. R., C. Samanta, and P. Jana. Hydrogenation of hydrogen peroxide over palladium/carbon in aqueous acidic medium containing different halide anions under static/flowing hydrogen. *Industrial & Engineering Chemistry Research*, 46 (2007a), 3237 – 3242.

Choudhary, V. R., C. Samanta, and P. Jana. Decomposition and/or hydrogenation of hydrogen peroxide over Pd/Al_2O_3 catalyst in aqueous medium: Factors affecting the rate of H_2O_2 destruction in presence of hydrogen. *Applied Catalysis A: General*, 332 (2007b), 70–78.

Davis, M. E., and R. J. Davis. *Fundamentals of Chemical Reaction Engineering*. McGraw-Hill, 2003.

Dissanyake, D. P., and J. H. Lunsford. The direct formation of H_2O_2 from H_2 and O_2 over colloidal palladium. *Journal of Catalysis*, 214 (2003), 113-120.

Fogler, H. S. Elements of chemical reaction engineering. Prentice-Hall, Englewood Cliffs, N.J. Ch. 12 (1992).

Hill, K. D. An investigation of palladium oxidation in the platinum/palladium thermocouple system. *Metrologia,* **39 (**2002), 51-58.

Hong, S.-W., Y.-S. Shin, J.-H. Song, S.-H. Chang. Performance test of the quenching meshes for hydrogen control. *Journal of Nuclear Science and Technology*, 40 (2003), 814-819.

Inoue, T., M. A. Schmidt, K. F. Jensen. Microfabricated multiphase reactors for the direct synthesis of hydrogen peroxide from hydrogen and oxygen. *Industrial and Engineering Chemistry Research*, 46 (2007), 1153-1160.

Jewell, L. L., and B. H. Davis. Review of absorption and adsorption in the hydrogen–palladium system. *Applied Catalysis A: General*, 310 (2006), 1–15.

Kreutzer, M. T., P. Du, J. J. Heiszwolf, F. Kapteijn, J. A. Moulijn. Mass transfer characteristics of three-phase monolith reactors. *Chemical Engineering Science*, 56 (2001) 6015–6023.

Landon, P., P. J.Collier, A. F. Carley, D. Chadwick, A. J. Papworth, , A. Burrows, C. J. Kiely and G. J. Hutchings. Direct synthesis of H_2O_2 from H_2 and O_2. *Phys. Chem. Chem. Phys.*, 5 (2003), 1917-1923.

Liu, Q., and J. H. Lunsford. The roles of chloride ions in the direct formation of H_2O_2 from H_2 and O_2 over a Pd/SiO_2 catalyst in a H_2SO_4/ethanol system. *Journal of Catalysis*, 239 (2006), 237-243.

Losey, M. W., M. A. Schmidt, and K. F. Jensen. Microfabricated Multiphase Packed-Bed Reactors: Characterization of Mass Transfer and Reactions. *Ind. Eng. Chem. Res.*, 40 (2001), 2555-2562.

McCabe, R. W. Palladium catalyst pre-oxidation to reduce light-off temperature. U. S. Patent 6187709 (2001).

Mears, D. E. Diagnostic criteria for heat transfer limitations in fixed bed reactors. *Journal of Catalysis*, 20 (1971), 127-131.

Melada, S., R. Rioda, F. Menegazzo, F. Pinna, and G. Strukul. Direct synthesis of hydrogen peroxide on zirconia-supported catalysts under mild conditions. *Journal of Catalysis*, 239 (2006a), 422–430.

Melada, S., F. Pinna, G. Strukul, S. Perathoner, G. Centi. Direct synthesis of H_2O_2 on bemetallic and monometallic catalytic membranes using methanol as reaction medium. *Journal of Catalysis*, 237 (2006b), 213-219.

Mills, P. L., and R. V. Chaudhari. Multiphase catalytic reactor engineering and design for pharmaceuticals and fine chemicals. *Catalysis Today*, 37 (1997), 367-404.

Nijhuis, T. A., F. M. Dautzenberg, J. A. Moulijn. Modeling of monolithic and trickle-bedreactors for the hydrogenation of styrene. *Chemical Engineering Science*, 58 (2003), 1113 – 1124.

Pospelova, T. A. and N. I. Kobozev. Palladium catalyzed synthesis of hydrogen peroxide from its elements. II. Active centres of palladium. *Russian Journal of Physical Chemistry*, 35 (1961a), 262-265.

Pospelova, T. A. and N. I. Kobozev. Palladium catalyzed synthesis of hydrogen peroxide from its elements. III. Active centres for the catalytic decomposition of hydrogen peroxide on palladium. *Russian Journal of Physical Chemistry*, 35 (1961b), 584-587.

Pospelova, T. A., N. I. Kobozev and E. N. Eremin. Palladium catalyzed synthesis of hydrogen peroxide from its elements. I. Conditions for the formation of hydrogen peroxide. *Russian Journal of Physical Chemistry*, 35 (1961), 143-147.

Potekhin, V. V., S. N. Solov'eva, V. M. Potekhin. Kinetics and mechanism of hydrogen peroxide decomposition in the presence of the tetraaquapalladium (II) complex. *Russian Chemical Bulletin (Int. Ed.)*, 54 (2005), 1105-1110.

Robles-Dutenhefner, P. A., D. L. Nunes, J. A. Goncalves, E. V. Gusevskaya, and E. M. B. Sousa. Sol-gel palladium composites: effect of thermal treatment on the catalytic activity. *Journal of Non-Crystalline Solids*, 348 (2004), 195-200.

Salem, I. A., M. El-Maazawi, A. B. Zaki. Kinetics and mechanisms of decomposition reaction of hydrogen peroxide in presence of metal complexes. *International Journal of Chemical Kinetics*, 32 (2000), 643 – 666.

Samanta, C., and V. R. Choudhary. Direct formation of H_2O_2 from H_2 and O_2 and decomposition/hydrogenation of H_2O_2 in aqueous acidic reaction medium over halide-containing Pd/SiO_2 catalytic system. *Catalysis Communications*, 8 (2007a), 2222–2227.

Samanta, C., and V.R. Choudhary. Direct synthesis of H_2O_2 from H_2 and O_2 over Pd/H-beta catalyst in an aqueous acidic medium: Influence of halide ions present in the catalyst or reaction medium on H_2O_2 formation. *Catalysis Communications* 8 (2007b), 73-79.

Satterfield, C. N. Mass Transfer in Heterogeneous Catalysts, M. I. T. Press, 1970, Ch. 2.

Sharma, C. S., P. Harriott and R. Hughes. Thermal conductivity of catalyst pellets and other porous particles: Part II: Experimental measurements. *Chemical Engineering Journal*, 10 (1975), 73-80.

Sivadinarayana, C., T. V. Choudhary, L. L. Daemen, J. Eckert and D. W. Goodman. The Nature of the Surface Species Formed on Au/TiO_2 during the Reaction of H_2 and O_2: An Inelastic Neutron Scattering Study. *Journal of American Chemical Society*, 126 (2004), 38-39.

Tadepalli, S., D. Qian, A. Lawal. Comparison of performance of microreactor and semi-batch reactor for catalytic hydrogenation of o-nitroanisole. *Catalysis Today*, 125 (2007), 64–73.

Vannice, M. A., Kinetics of Catalytic Reactions, Springer Science, 2005.

Wada, Y., M. A. Schmidt, and K. F. Jensen. Flow Distribution and Ozonolysis in Gas-Liquid Multichannel Microreactors. *Ind. Eng. Chem. Res.*, 45 (2006), 8036-8042.

Task 6: Laboratory Reactor System Optimization and Evaluation

The modeling and simulation work in Task 1 focussed principally on the flow characteristics in microchannels. The flow behaviour plays a very important role in reactor design. We established that the gas-liquid flow in microchannels is mainly the Taylor slug flow. The gas and liquid slug lengths depend on superficial velocity, channel diameter, fluid property and inlet geometry. From this activity, we learned how to design a multiphase micro-reactor such that the gas and liquid slug lengths are minimized and consequently mass transfer between the phases is enhanced.

We next incorporated reaction kinetics into the modeling and simulation of two phase flows. This multiphase flow with chemical kineitcs was quite challenging because it involved momentum, heat and mass transfer as well as chemical reactions. Furthermore, the use of solid catalyst makes the problem more complicated because the actual flow has three phases in addition to the gas and liquid phases. It is very difficult to determine in which of the phases the reaction exactly takes place, is it in liquid slugs, or in gas slugs, or between the gas and liquid phases? This is the key question that needs to be addressed for this type of reactor before any meaningful simulation can be carried out. However, the answer was not readily available, hence we expected that CFD would throw some light on the question.

The verison of our CFD software had the capability to deal with multiphase species transport. However, the user has to simplify the physical problem, choose an appropriate model, and then incorporate some user-defined functions. Here we still used the VOF two phase model with chemical reactions. We selected the o-nitroanisole hydrogenation reaction as the model reaction since we had obtained experimentally the rate expressions for this reaction in addition to the one that was available in the literature. The complete rate expressions for the H_2O_2 kinetics were not available at the beginning of this activity because of the complexity of the kinetics of the direct combination process (see Task 5 above). Since both the hydrogenation reaction and the direct combination reaction are multiphase gas/liquid reactions, the knowledge gained in the CFD simulation on hydrogenation reaction will be applicable to that of H_2O_2 reaction.

The first step in the CFD simulation was to assume that the reaction involved both the gas and liquid phases. Since the model reactor was a packed bed, and there is a thin liquid film on the catalyst surface, we made the assumption that the reaction occurred inside the whole volume, both gas and liquid. Figure 6.1 shows the mass fraction of o-nitroanisole along the reactor length, and Figure 6.2 shows the mass fraction of anisidine along the reactor length. One can clearly see the change of the reactant and product concentrations inside the reactor.

Another objective of this activity was to study the mass transfer between the phases. From the species concentration distribution, the mass transfer coefficient can be computed and compared with our experimental value and that in the literature.

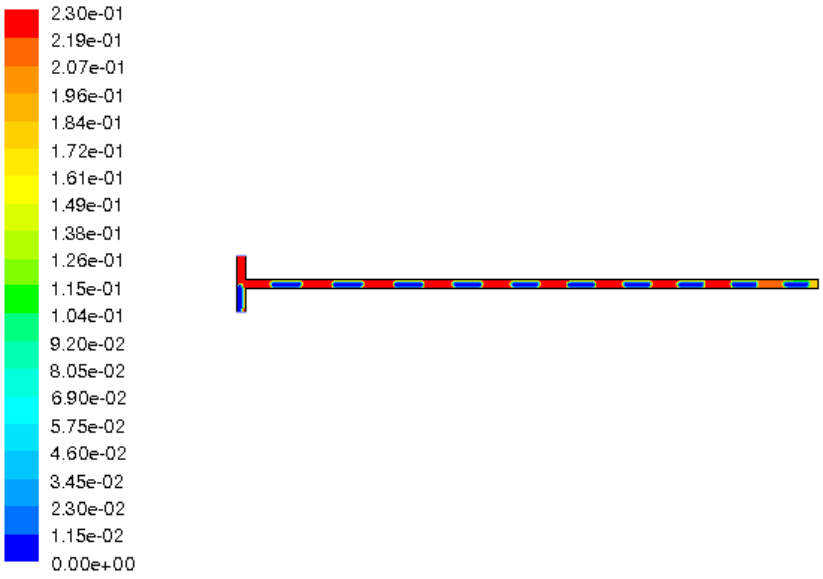

Figure 6.1: **Mass fraction of o-nitroanisole (reactant) along the reactor**

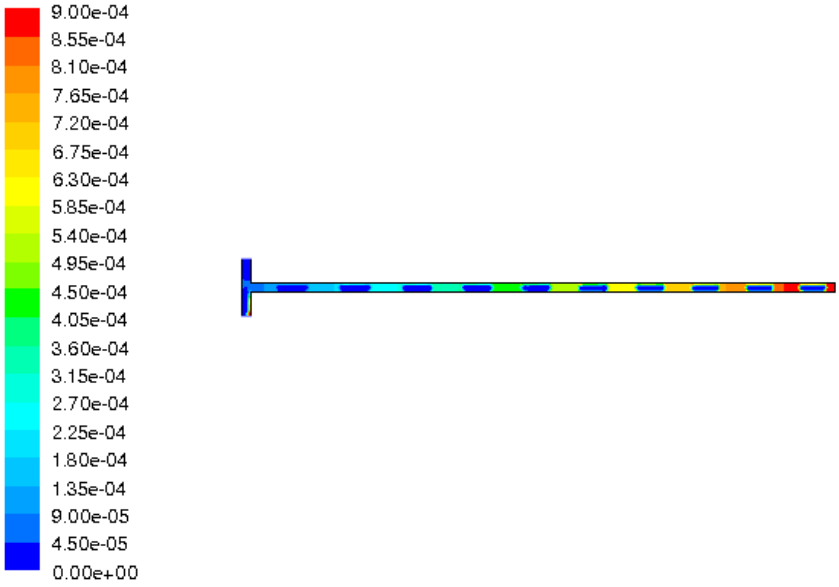

Figure 6.2: **Mass fraction of anisidine (product) along the reactor length**

As a first step, we applied the simple 1D model for the kinetic analysis. We assumed values for the mass transfer coefficients, and predicted the effluent product concentration. When the predicted and measured effluent concentrations agreed, the correct mass transfer coefficient had been selected. We next predicted reactant and product concentration profiles along the reaction length. However, no detailed information about slug length and its variation with reaction extent could be obtained from the 1D analysis. Also, with the 1-D analysis, the question as to whether the reaction took place predominantly in liquid or gas phase could not be unanswered. Inherent in the 1-D analysis is that the reaction occurs at the interface between the gas and liquid.

The predicted reaction extent from the simulation was much smaller than that obtained from the experimental data. We next assumed that the reaction took place in the liquid, because the substrate was in the liquid phase. Hydrogen from the bulk gas transfers across the interface, dissolves in the liquid, and then reacts with the reactant. Although the catalyst was packed in the bed, the model treated the solid only as a momentum sink. The VOF two phase model was still used in the simulation. A gas to liquid mass transfer mechanism was superposed on the simulation and a mass transfer parameter of 5 s^{-1} was assumed.

Figure 6.3 shows the slug lengths inside the reactor; liquid slug is shown in red while the gas slug is in blue. One can see that, as the reaction proceeds down the reactor length, the gas slug is getting shorter because of the consumption of hydrogen; at the same time, the liquid slug is getting longer because of the liquid product. Figure 6.4 is the mass fraction of o-nitroanisole along the reactor length which as expected should reduce since the reactant is being consumed by the reacton. Figure 6.5 is the mass fraction of hydrogen dissolved in liquid. The concentration of hydrogen in the liquid is very small because of its low solubility. There is a distribution of hydrogen concentration inside the liquid slug because of the diffustion and reaction effects. Near the interface, hydrogen concentration in the liquid is larger for there is a direct contact between the gas and liquid phase.

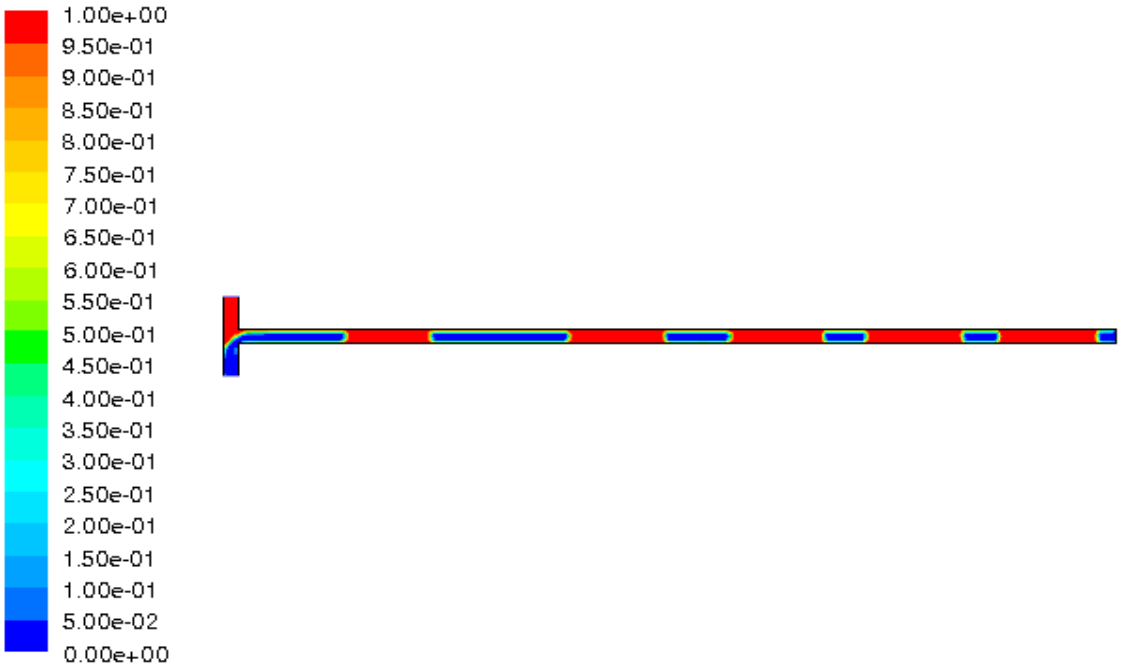

Figure 6.3: Gas (blue) and liquid (red) slugs inside the reactor

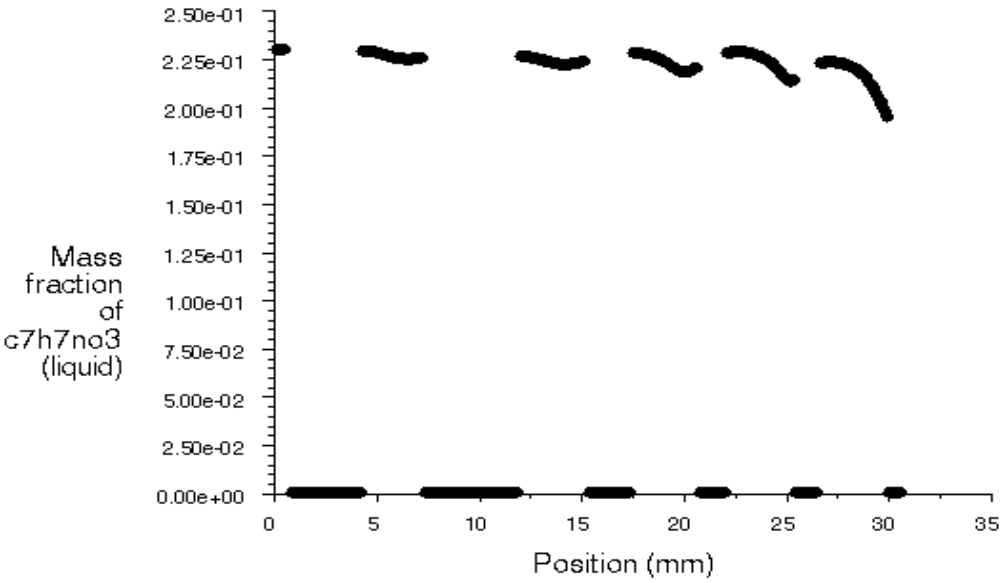

Figure 6.4: Mass fraction of o-nitroanisole (reactant) along the reactor

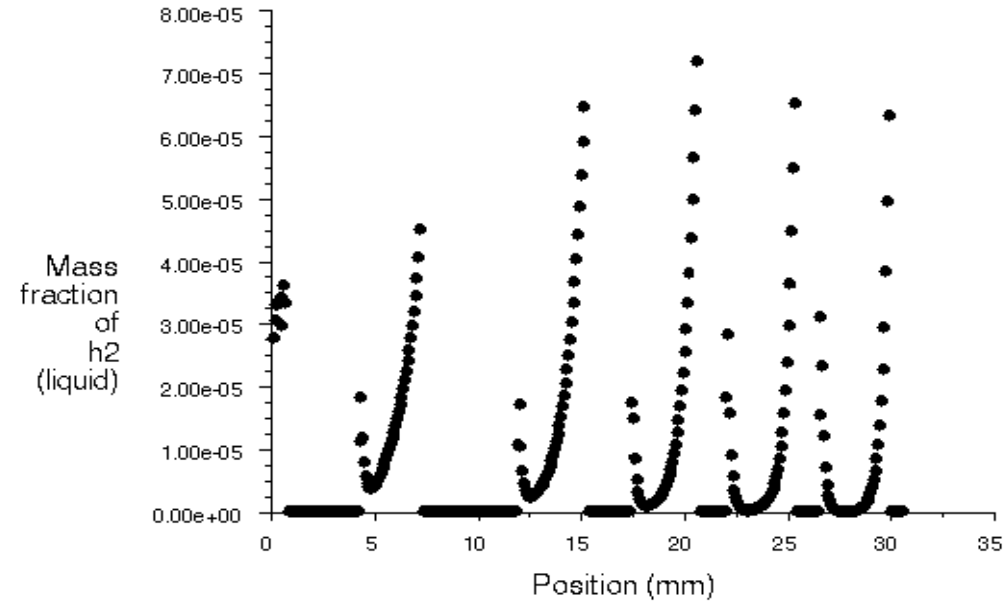

Figure 6.5: Mass fraction of hydrogen in the liquid phase (reactant) along the reactor

The mass transfer parameter from gas to liquid was an adjustable parameter in the model we used. According to the literature, the mass transfer coefficient in microreactors is 2 orders of magnitude larger than that in standard laboratory scale reactors. The significant increase of mass transfer coefficient is the primary advantage of microreators over conventional reactors. Many fast reactions which are hitherto difficult to conduct in conventional reactors due to poor mass transfer will be much easier to perform in microreactors. Losey et al., 2001 used micro-fabricated packed bed reactors for the hydrogenation of cyclohexene and obtained the mass transfer parameter in the range of 5 to 15 s^{-1}. The mass transfer parameter of 5 s^{-1}, which was used in previous simulations was changed to 10 s^{-1} and the simulations repeated. The results are shown in Figures 6.6 – 6.8. When the mass transfer rate of hydrogen into the liquid becomes faster, the reduction of gas slug length along the reactor is faster, and so is the increase of liquid slug length. This also results in more consumption of o-nitroanisole, which implies that more substrate is converted to the product in the reactor. However, the hydrogen concerntration in the liquid phase is much higher compared to the previous result due to the faster rate at which it is replenished. This higher level of hydrogen concentration enables a higher reaction rate than in the previous model. Applying this model, the gas-liquid mass transfer parameter in the microreactor can be obtained by fitting the model results with the experimental data.

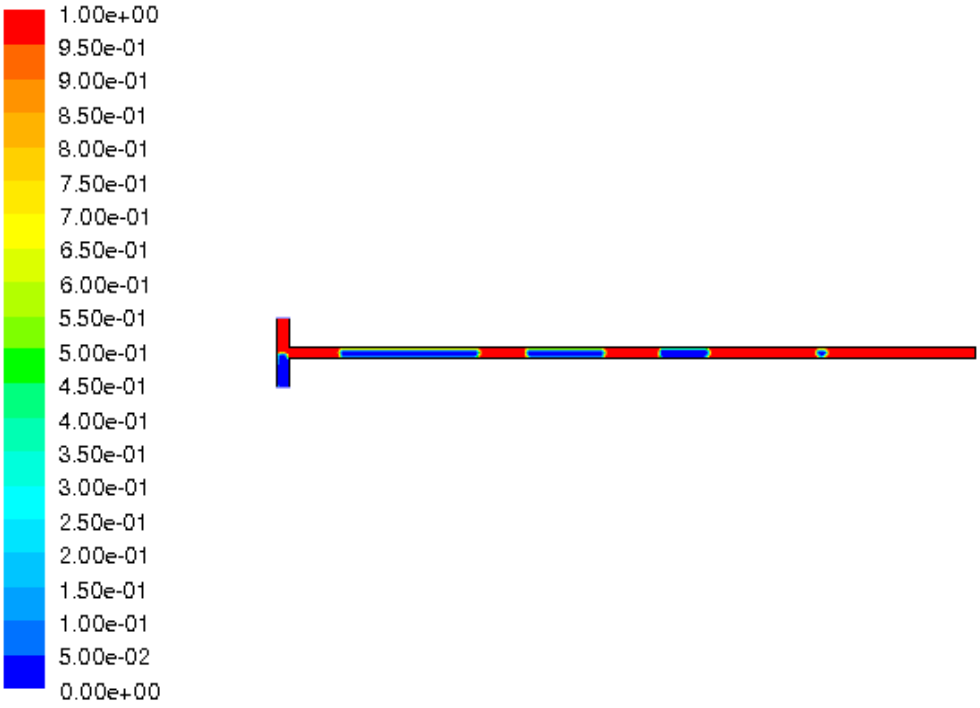

Figure 6.6: Gas (blue) and liquid (red) slugs inside the reactor

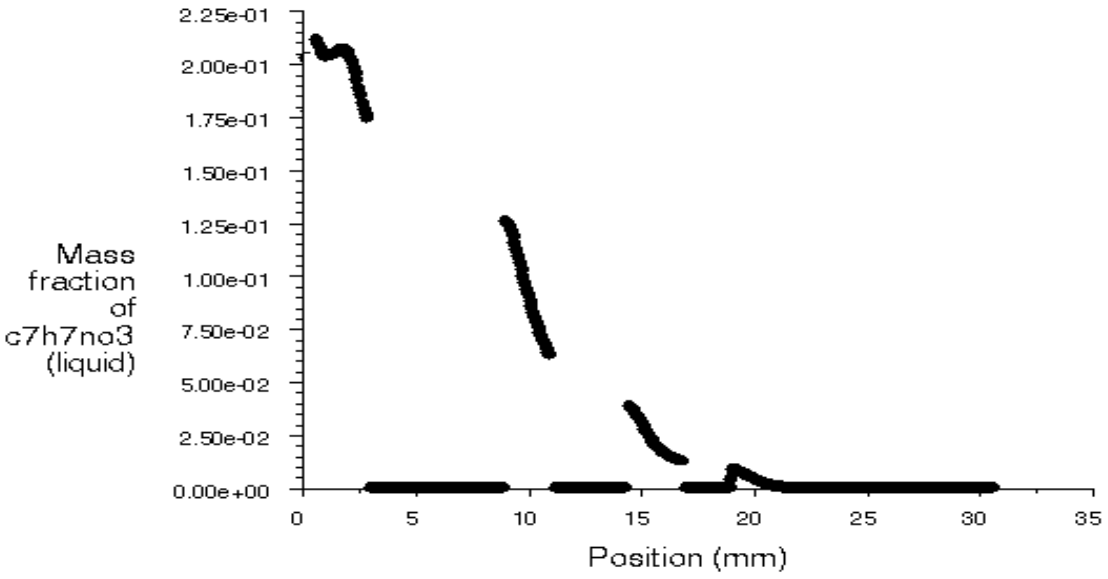

Figure 6.7: Mass fraction of o-nitroanisole (reactant) along the reactor length

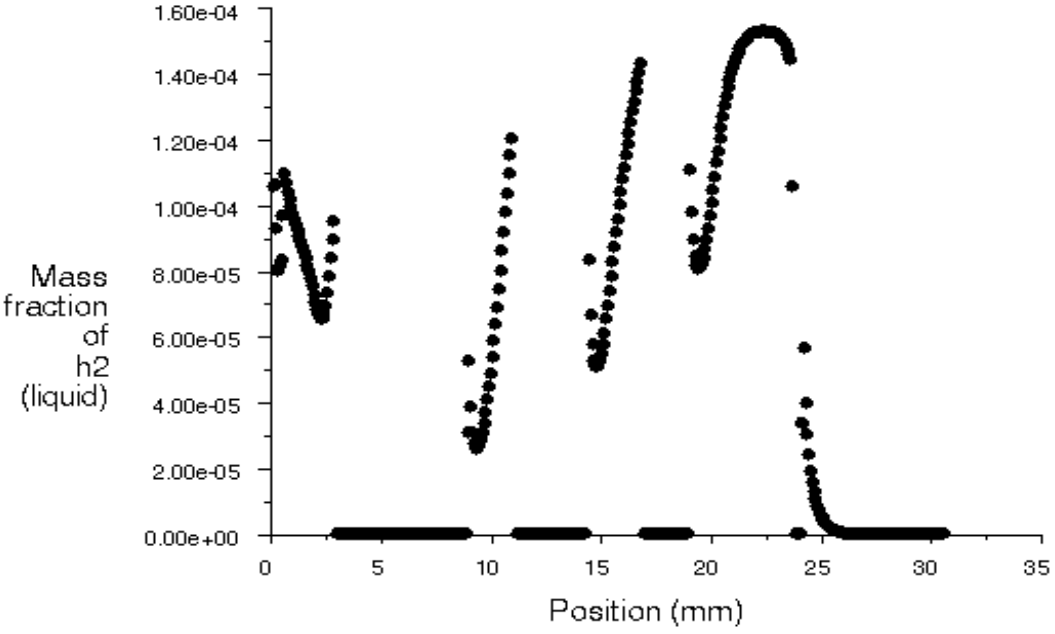

Figure 6.8: Mass fraction of hydrogen in the liquid phase (reactant) along the reactor length

The second hydrogenation reaction considered in this activity was that of the BMS proprietary molecule, a nitro ketone. The reaction pathway for this molecule was identified and the corresponding kinetics determined. Compared to the previous model reaction – hydrogenation of o-nitroanisole to o-anisidine, this reaction had some distinct features: the concentration of the

substrate was much smaller in the reaction solution because the substrate was solid; the reaction was much faster so a higher process flow rate was generally required to eliminate the mass transfer effect.

Similar to the simulation of the previous model reaction, the model we used for hydrogenation of BMS molecule is also multiphase reaction VOF model: hydrogen passes through gas-liquid inteface, dissolves into the liquid, and then reacts with the substrate. The chemical reaction only takes place in the liquid phase, and the gas is transferred into liquid by gas-liquid mass transfer process. In this simulation, the chemical kinetics used was that obtained in our lab, and the mass transfer coefficient from gas to liquid was $10s^{-1}$.

Figure 6.9 shows the slug lengths inside the reactor; liquid slug is in red and gas slug is in blue. One observes that, as the reaction proceeds downstream of the reactor, the gas slug length is becoming shorter and shorter because of the consumption of hydrogen; at the same time, the liquid slug is getting longer because of the liquid product. Figure 6.10 presents the mass fraction of nitro compound along the reactor length which reduces with reactor length since it is being consumed by the reacton. Figure 6.11 is the mass fraction of hydrogen dissolved in liquid. The concentration of hydrogen in the liquid is very small because of its low solubility in the substrate. It's observed that there is a hydrogen concentration distribution inside the liquid slug because of the interplay between diffusion and reaction effects. At the interface on the liquid side, hydrogen concentration is higher than in the bulk liquid because there is a direct contact between the gas and liquid phase. Along the reactor length, average hydrogen concentration in the liquid increases, which indicates that the diffusion rate is faster than the reaction rate.

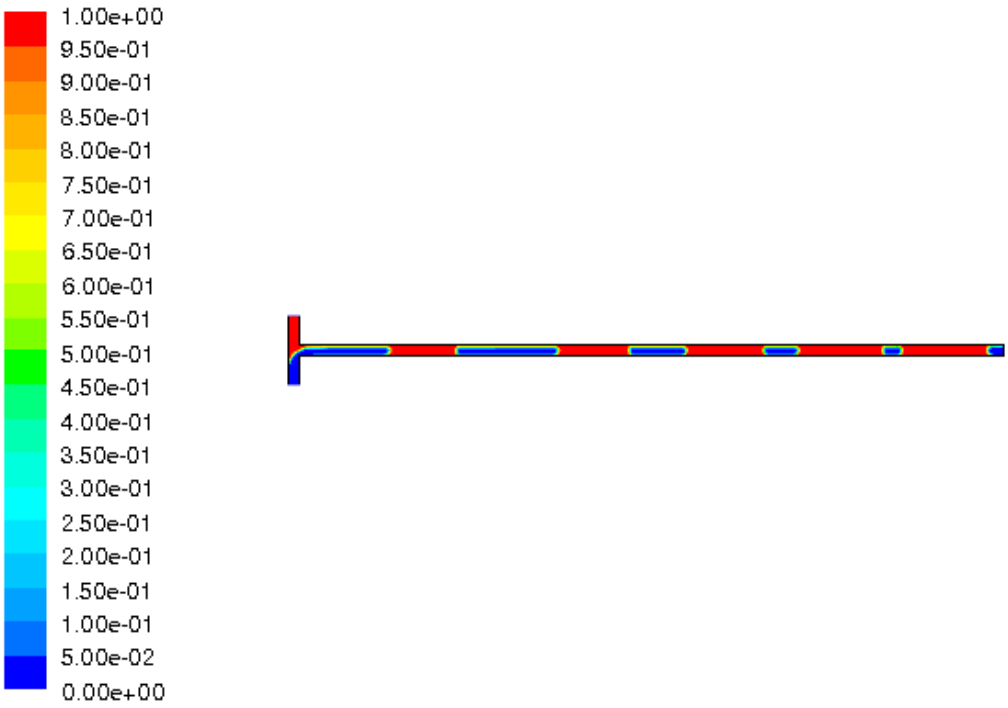

Figure 6.9: **Gas (blue) and liquid (red) slugs inside the reactor**

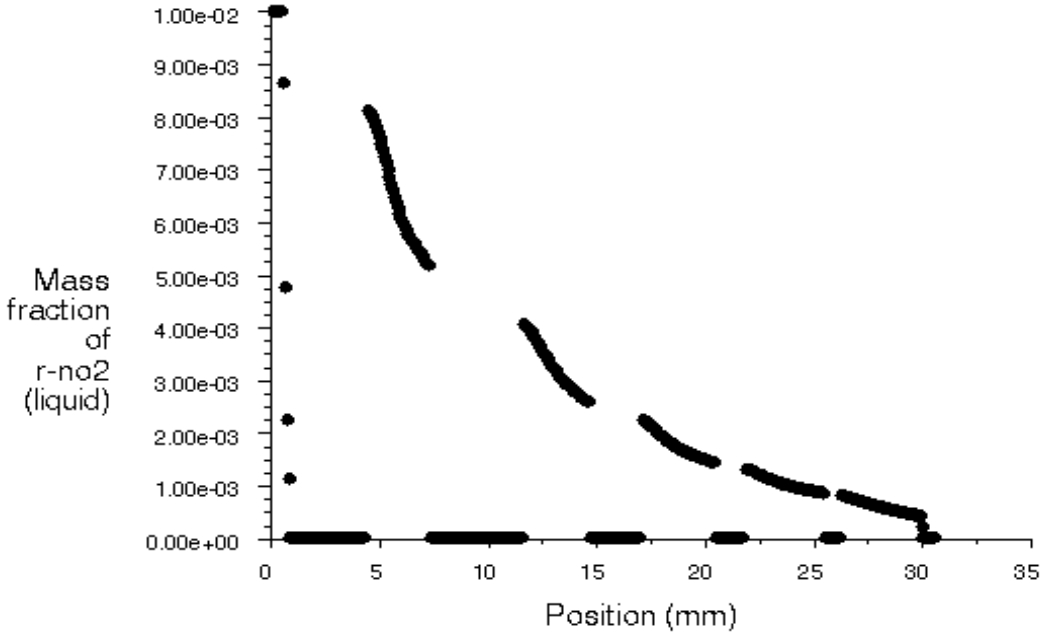

Figure 6.10: **Mass fraction of nitro compound (reactant) along the reactor length**

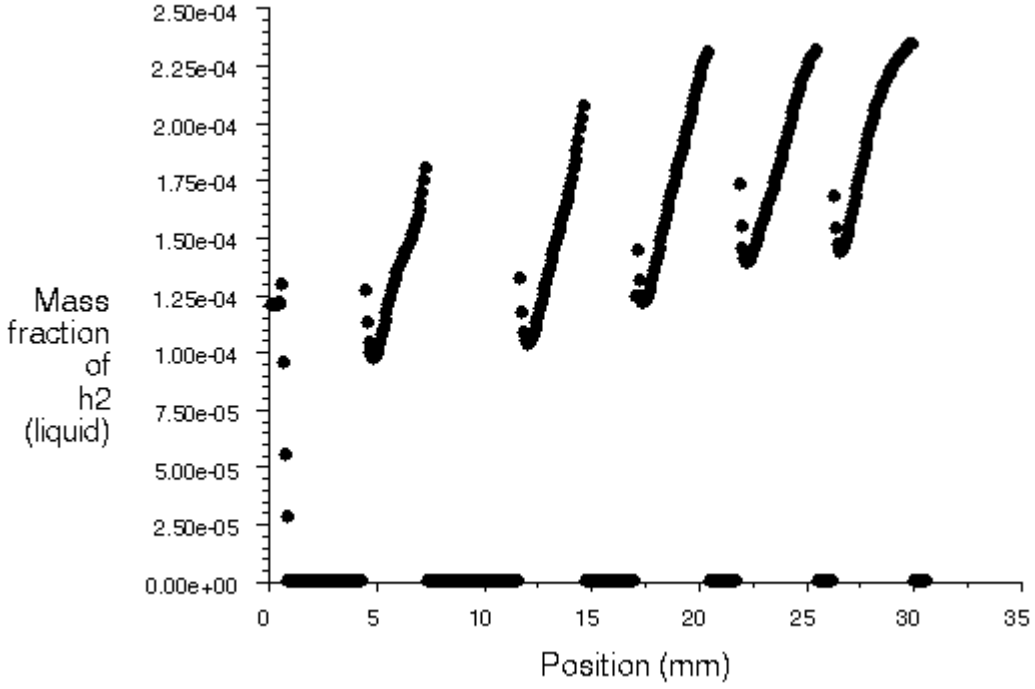

Figure 6.11: Mass fraction of hydrogen in the liquid phase (reactant) along the reactor length

The CFD simulations of H_2O_2 production by direct combination of H_2 and O_2 were begun after the kinetics became available. The reaction pathway of this synthesis approach is complicated as discussed extensively in Task 5; it involves four parallel/series reactions, namely: synthesis (reaction 1), water formation (reaction 2), H_2 reduction (reaction 3) and disproportionation or

decomposition (reaction 4). However, based on our laboratory experimental conditions, reaction 2 and reaction 4 were negligible. Therefore, these two series reaction steps, H_2O_2 synthesis and reduction of H_2O_2, were the most important reactions to consider in our modeling and simulation work. A detailed study of these two reactions in our laboratory provided the complete kinetics information.

The model reactor is the T-junction micro-reactor same as the one we used in our other CFD simulations work on the hydrogenation reaction. The multiphase model is again the VOF. There is one feature of this reaction system that distinguishes it from the hydrogenation reaction. The two reactants H_2 and O_2, which participate in the main reaction, i.e., synthesis of H_2O_2, are in the gas phase with an essentially inert liquid phase while one of the reactants in hydrogenation is in the liquid phase. The main synthesis reaction takes place in the gas phase, whereas hydrogenation occurs in the liquid phase. Here is the model we propose for CFD simulations of the direct combination process: H_2 and O_2 combine in the gas phase to form H_2O_2, and then the formed H_2O_2 passes through the gas/liquid interface and dissolves into the liquid phase; meanwhile some H_2 dissolves in the liquid phase and then reacts with H_2O_2 for the reduction reaction. Since the reduction is very small because of the low solubility of H_2 in water, and the available version of Fluent6.2 did not support two user-defined homogeneous reactions simultaneously, we focused only on the synthesis reaction.

The simulation conditions were close to what we used in the laboratory experiments. The in-house reaction kinetics was used in the CFD simulations. In gas-liquid interface, the mass transfer parameter of H_2O_2 from gas to liquid was set to 10 s^{-1}. Figure 6.12 shows six flow patterns at consecutive snapshot times with inverval of 0.04 s. Because of the large flow rate ratio of the gas to the liquid, we were not able to see many slugs in the reactor. However, it is clear that the liquid slug is getting longer as we proceed downstream because of liquid product. We can also expect that the gas slug will be getting shorter downstream because both H_2 and O_2 are being consumed.

Figure 6.13 is the profile of mass fraction of H_2O_2 in the liquid phase corresponding to the states of Figure 6.12(a) ~ (f). Along the reactor length, the H_2O_2 concentration is increasing due to its production. The distribution of H_2O_2 concentration is close to linear inside the liquid slug, and the slope of the lines is almost the same. Figure 6.14 is the profile of mole fraction of H_2 in the gas phase corresponding to the state of Figure 6.12(f). The H_2 concentration is decreasing slightly along the reactor due to its consumption by the reaction. The distribution of H_2 concentration also follows a linear relationship. These linear relationships can probably be attributed to the fact that, in our simulation conditions, the H_2 conversion was low, and the H_2O_2 concentration in the liquid was kept small.

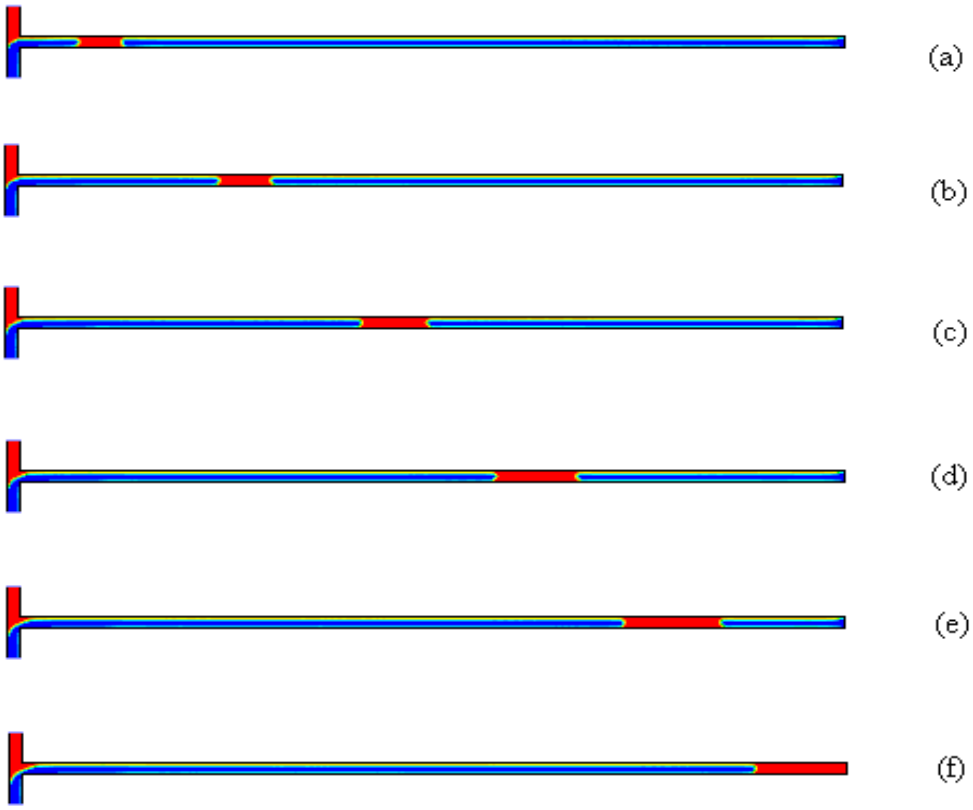

Figure 6.12: Six flow patterns at consective snapshot times with inverval of 0.04 s (blue —— gas, red —— liquid)

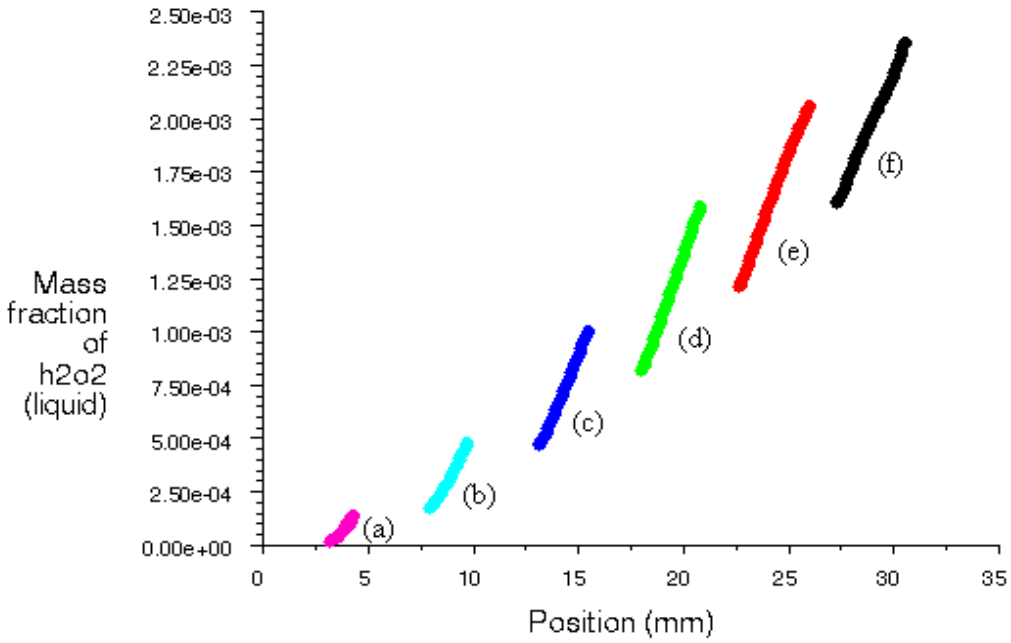

Figure 6.13: Mass fraction of H_2O_2 in the liquid phase corresponding to the states of Figure 1(a) ~ (f).

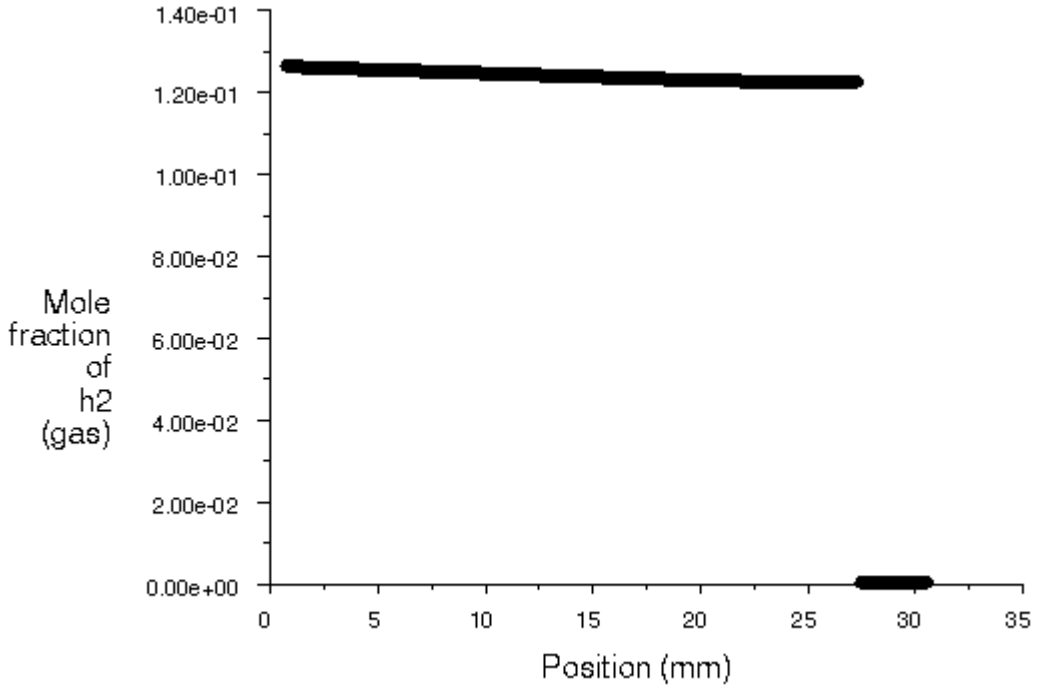

Figure 6.14: Mole fraction of H_2 in the gas phase corresponding to the state of Figure 8(f).

TASK 7: Microchannel Reactor Fabrication

At the end of Phase I of the project, we reviewed the go/no-go criteria for phase 2, and based on the outcomes of Tasks 1 to 6, the criteria were met. Towards this end, FMC approved fund internally, as part of its in-kind and cash contributions to the project, for the demonstration of the prototype system of 1 kg/hr production of approximately 1 wt% H_2O_2. The plan was to implement a single-flow through system with a set-up at the FMC's Princeton facility. Data would be collected to validate the laboratory performance in the demo unit especially the catalyst life. The information would be crucial in the evaluation of the economic viability of the process.

We selected Chart-Energy as the supplier of the multilayer, multichannel microreactor unit for the demo. Following a visit to Chart-Energy at their La Crosse facility in June 2006, we worked with the company to complete the pre-design of the demo's reactor unit. The reactor comprised about 500 channels of dimension 800 µm by 800 µm made of SS316L. Air/O_2 mixture was the main gas stream and H_2 stream was designed to be injected at the top of the catalyst bed. The catalyst was supported by a screen. The reactor block size (not including the tubing and flange) was about 103 mm (width) by 63 mm (height) by 175 mm (length). The demo unit was completely assembled within a few weeks of delivery by Chart-Energy.

FMC's internal catalyst was first used for the trial runs to acquire experience with the operation of the demo unit. Thereafter, the plan was to follow-up with the sol-gel catalyst developed for this project. It was to be noted that we had shown in the laboratory system that the hydrogen peroxide productivity using FMC's internal catalyst was relatively low compared to that of the sol-gel catalyst developed for this project. However, FMC's catalyst was available in commercial amounts but the quantity of the sol-gel catalyst was currently limited by small-scale laboratory production . It therefore made sense to use the FMC catalyst for the initial trial runs to perfect the operation of the demo unit.

Figure 7.1: Multichannel High Throughput Microreactor

A safety review of the pilot plant was conducted. The demo unit was successfully loaded with FMC's catalyst using FMC's internally developed catalyst loading technique. Few experimental runs in the temperature range of 35 to 60^{o}C and liquid flow rate of 0.3 kg/hr to 1 kg/hr of 1 wt% H_2SO_4 solution with 10 ppm of NaBr were conducted in the demo unit loaded with 14.5 g of FMC catalyst. A certified pre-mixed 3vol% H_2 in air at flow rates ranging from 19 standard liters per minute (slm) to 24 slm was used. Our preliminary results showed that 200 to 400 ppm of H_2O_2 were obtained with optimum productivity occurring between 50 and 55^{o}C. We also made a few runs in the single capillary reactor of 0.775 mm ID (775μm), and 7.3 inches in length (similar to the length of microreactor pilot unit) using the certified pre-mixed 3vol% H_2/Air at about 50 sccm and 1 wt% H_2SO_4 solution at flow rate of 3.0 ml/min and temperature range of 50 to 55^{o}C. We obtained about 350 to 400 ppm of H_2O_2 which was in the same concentration range obtained in the pilot demo unit. Thus our preliminary results showed that the scale-up from a laboratory single tube reactor to a multichannel microreactor was confirmed. Subsequent experimental runs would focus on optimization studies.

However, before we could begin this set of runs, we experienced some difficulties with the removal of the catalyst from the microchannels of the pilot plant reactor after the end of the preliminary runs which utilized FMC catalyst for system shake-up. Majority of the 450 microchannels were blocked. Some of the channels were later successfully cleaned out by drilling. After other attempts to unpack the reactor unit failed, we found out that the channels could be easily cleaned and the reactor unpacked by using high pressure steam. By applying repeated sudden opening and closing of the steam flow after pressure build up in the unit, the catalyst was removed from the unit. These difficulties enabled us to develop and acquire the know-how for unpacking such multichannel microreactor units.

The next set of experiments was conducted with FMC's propriety catalyst (***a modified version of the catalyst sample supplied to Stevens in 2003***). We discovered operating conditions that allowed us to produce over 2 wt% H_2O_2 in a single-channel reactor from a gas feed of 3% hydrogen in air and a solution feed of 1 wt% H_2SO_4 (with 10 ppm NaBr). Under the same operating conditions in the multi-channel pilot reactor, however, very low concentrations of peroxide (under 500 ppm) were initially obtained. We began to investigate the reasons for the low productivity of the multi-channel pilot compared to the single-channel reactor. In the previous pilot runs, the pre-mixed 3% H_2-air mixture flowed into the top of the reactor channels and the aqueous feed was injected through liquid injection ports within each channel. We concluded that there was non-uniform distribution of the liquid feed into the individual channels through these injection ports which led to both poor mixing and non-uniform gas-liquid distribution in the reactor channels. The pilot injection ports are about 150 μm in diameter, which was too large to create a high enough back-pressure to promote uniform liquid distribution in every channel. To resize the injection ports would require ordering a new reactor, the delivery of which would result in considerable delay to the project and thus extending the completion deadline. We therefore investigated and implemented a change in liquid-gas distribution, introducing both the gas feed (3% pre-mixed H_2 in air) and the aqueous feed (1 wt% H_2SO_4 solution with 10 ppm of NaBr) simultaneously through the liquid injection ports to increase the pressure for better mixing and more uniform distribution into the channels. With this change we observed a significant improvement in the productivity of the pilot reactor.

The reactor channels were filled with 18 g of FMC's proprietary catalyst and the flow rate of the aqueous feed was varied between 0.5 kg/hr and 1 kg/hr. The flow rate of the 3% H_2-air mixture was varied between 19 to 45 standard liters per minute and the temperature from 35 deg

C to 60 deg C. The reactor pressure was controlled under 1000 psig to provide an equivalent partial pressure of hydrogen to that of about 9% H_2 in air at 300 psig. Under this range of operating conditions we produced at or above 1 wt % H_2O_2 at a liquid (aqueous) flow rate of 1 kg/hr. This proved that the pilot reactor could achieve the production rates specified in the contract with DOE using FMC's commercially manufactured catalyst. This catalyst has the added advantage of stability, with a proven catalyst life of over 36 months in commercial operation.

We next investigated the effects of different combinations of flow configurations of the gas-liquid mixture into the pilot microreactor through the two sides injection points and through the top and bottom of the reactor. The uniform distribution of the gas-liquid mixture into each of the 451 channels was found to be very critical to obtaining high productivity. From our results, as shown in the tables below, we concluded that the design of the injection points of this reactor, particularly the size at 150 µm was too large and needed to be redesigned. We plan to do this in our future development work which would continue outside the DOE grant.

Table 7.1: Downward Concurrent Flow at Low Temperature and Pressure

Configuration	Description	Pressure Drop psig	Wt % H_2O_2
A	Flow Gas and Liquid from the Top.	14	0.13
B	Flow Gas from Top Flow Liquid from both sides of the Injection points.	16	0.48
C	Flow Gas and Liquid from one side of the Injection points.	17	0.51
D	Flow Gas and Liquid from both sides of the Injection points.	17	0.50

Table 7.2: Upward Concurrent Flow at High Temperature and Pressure

Configuration	Description	Pressure Drop, psig	Wt % H_2O_2
E	Flow Gas and Liquid from the Bottom.	45	0.10

F	Flow Liquid from the Bottom and Flow Gas from One Side of the Injection Points.	6	0.07

We had some problems in the development of an accurate and reproducible analysis of both the inlet and exiting gas compositions from the microreactor. The results of such analysis would enable us to determine the conversion of the feed gas as well as the selectivity of the catalyst among other variables like space-time yield for characterizing the catalyst performance. We finally developed the GC method to analyze the composition of the exit gas from the reactor. We used Shimadzu GC-2014, a packed column and TCD (thermal conductivity detector). 2%, 5%, 10% and 15% of standard H_2 in N_2 mixtures were used to make the calibration. We optimized the conditions and developed a very accurate method to measure hydrogen concentration. We are currently using both the single capillary reactor and multi-channel microreactor pilot unit to collect data using our developed GC method.

FMC would continue to self-fund R&D on this project beyond the scope of the DOE project in an attempt to further improve the feed distribution and productivity of the multi-channel pilot reactor. We will reverse the pilot reactor flows so that the liquid feed enters the channels and the gas feed is introduced through the injection ports. Further optimization studies using FMC's catalyst in the single channel reactor are also planned, as are material balance runs in both units. The re-design and purchase of an improved pilot reactor is also under consideration. The extensive data to be collected on the multichannel reactor performance will then provide a strong basis for the evaluation of the economic feasibility of the process.

The results of this activity were presented at the AIChE Spring Meeting in New Orleans, LA on 4/7/2008 under Topical 5: IMRET-10: 10^{th} International Conference on Microreaction Technology in a paper entitled "**Production of Hydrogen Peroxide via the Direct Combination of H_2 and O_2 in a Pilot Microreactor"**

6. Products Developed and Technology Transfer Activities

a. Publications

A. Lawal, W. Lee, and E. Dada, "Microchannel Reactor System Design & Demonstration for On-site H_2O_2 Production by Controlled H_2/O_2 Reaction," *Process Intensification Topical Conference Proceedings, AIChE Spring National Meeting, New Orleans, March 30 – April 3, 2003*.

R. Halder, S. Tadepalli, H. Qiu, W. Lee, A. Lawal, and E. Dada, Microchannel Reactor System Design & Demonstration for On-site H_2O_2 Production by Controlled H_2/O_2 Reaction, *Process Intensification Topical Conference Proceedings, AIChE Spring National Meeting, New Orleans, April 26 – April 29, 2004*.

J. Adeosun, and A. Lawal, Mass Transfer Enhancement in Micro-channel Reactors, *International Workshop and Symposium on Industrial Drying, India (2004), pp. 317 – 333.*

A. Lawal, R. Halder, S. Tadepalli, Y. Voloshin, H. Chen, W. Y. Lee and E. Dada, Microchannel Reactor System Design & Demonstration for On-site H_2O_2 Production by Controlled H_2/O_2 Reaction, *Process Intensification Topical Conference Proceedings, AIChE Spring National Meeting, Atlanta, April 10 – April 14, 2005*.

Y. Voloshin, A. Lawal, R. Halder, H. Chen, W. Y. Lee, and E. A. Dada, "Determination of Kinetics of H_2O_2 Formation by Direct Combination of H_2 and O_2 in a Microreactor," *Proceedings of AIChE National Spring Meeting, Orlando, April 23 – 27, 2006*.

J. T. Adeosun, and A. Lawal, "Numerical and Experimental Study of Mixing Enhancement in Micromixers using Residence Time Distribution (RTD)," *Applications of Micro-reactor Engineering Topical Conference Proceedings, AIChE Spring National Meeting, Orlando, April 23 – 27, 2006*.

J. T. Adeosun, and A. Lawal, Theoretical and experimental studies of mixing enhancement in micromixers, *Proceedings of AIChE Spring National Meeting, Houston, April 22 – 27, 2007.*

Y. Voloshin, R. Halder, and A. Lawal, Kinetics of H_2O_2 formation by direct combination of H_2 and O_2 in a microreactor, *Proceedings of AIChE Spring National Meeting, Houston, April 22 – 27, 2007.*

A. Lawal, Y. Voloshin, H. Qiu, W. Y. Lee, and E. A. Dada, Microchannel reactor system design & demonstration for on-site H_2O_2 production by controlled H_2/ O_2 reaction, *Proceedings of AIChE Spring National Meeting, Houston, April 22 – 27, 2007.*

J. T. Adeosun, and A. Lawal, Mass Transfer Enhancement in Microchannel Reactors by Re-orientation of Fluid Interfaces and Stretching, *Sensors and Actuators B*, *110 (2005) 101-111*.

D. Qian, and A. Lawal, Numerical Study on Gas and Liquid Slugs for Taylor Flow in a T-junction Microchannel, *Chemical Eng. Science*, *61 (2006) 7609-7625*.

Y. Voloshin, R. Halder, and A. Lawal, Kinetics of Hydrogen Peroxide Synthesis by Direct Combination of H_2 and O_2 in a Microreactor, *Catalysis Today*, *125 (2007) 40 – 47*.

Y. Voloshin, and A. Lawal, Kinetics of Hydrogen Peroxide Reduction by Hydrogen in a Microreactor, *Applied Catalysis A: General*, *353 (2008) 9 – 16*.

Y. Voloshin, J. Manganaro, and A. Lawal, Kinetics and Mechanism of Decomposition of Hydrogen Peroxide over Pd/SiO_2 Catalyst, *Ind. Eng. Chem. Res.*, *47 (2008) 8119 – 8125.*

Y. Voloshin, and A. Lawal, Overall Kinetics of Hydrogen Peroxide Formation by Direct Combination of H_2 and O_2 in a Microreactor, to be submitted to *Chemical Engineering Science*, 2008

J. Adeosun, and A. Lawal, Numerical and Experimental Studies of Flow and Mixing in a T-junction Microchannel Using Residence Time Distribution, submitted to *Chemical Engineering Science*, 2008.

S. Tadepalli, Cataltyst Preparation, Screening, and Microreactor System Evaluation for H_2O_2 Production by Controlled H_2/O_2 Reaction, *Master's thesis*, Stevens Institute of Technology, December 2004.

O. C. Okafor, Optimizing Sol-gel Catalyst Formulation for Direct Synthesis of Hydrogen Peroxide in a Microreactor, *Master's thesis*, Stevens Institute of Technology, May 2006.

N. Joshi, Effect of Processing Conditions, Pre-cursor and Additives on the Catalytic Activity of Sol-gel Catalysts for H_2O_2 sythesis, *Master's thesis*, Stevens Institute of Technology, December 2007.

Y. Voloshin, Microchannel Reactor System for Synthesis of H_2O_2 by Direct Combination of H_2 and O_2, *Ph.D. thesis*, Stevens Institute of Technology, May 2008.

b. Web site or other Internet sites that reflect the results of this project

Feature articles about the project in:
Chemical Engineering Progress,(October 2003, pg. 51)
Inside the Fuel-Cell Industry (10/12 – 10/19/03)

EurekAlert (10/14/03)
News and Articles on Materials Engineering (10/14/03)
Jersey Journal (10/14/03)
Small Times News (12/8/03), and
C&ENews (10/11/04)

c. Networks or collaborations fostered

Stevens Institute of Technology and Karlsruhe Research Center (KRC), a German organization with renowned expertise in the fabrication of metallic multichannel microreactors, signed a Memorandum of Understanding in June 2003 that allowed us to collaborate on microreactor fabrication. As part of the agreement, KRC made available to us on loan, a micromixer (which was incorporated into our experimental set-up), and a multichannel microreactor/heat exchanger. KRC and Stevens Institute of Technology have continued to exchange useful technical information on microreactor systems for chemical synthesis.

Stevens Institute of Technology and Cornell Nanofabrication Facility (CNF) – an NSF Center at Cornell signed a Memorandum of Understanding in August 2005 that enabled Mr. John Adeosun, my graduate student to use the state-of-the-art MEMS facilities at CNF to fabricate two micromixers, one a T-junction mixer and the other Multilaminated/Elongational Flow Micromixer (MEFM-4)**,** both from silicon. The results of his work are reported in Task 3 above.

Our work on microreactors has been widely disseminated, and we have received numerous requests for information on this project and others being carried out at our Center. International Flavors and Fragrances (IFF) approached us in August 2006 to develop a framework for a collaborative effort on the use of microreactors for immiscible liquid-liquid reactions. IFF currently supports a PhD student at Stevens on this collaborative project. GeoSpecialty Chemicals and Stevens are also currently exploring the possibility of a joint project on the use of microreactors for chemical synthesis to be fully sponsored by GeoSpecialty Chemicals.

d. Technologies/Techniques

Microreactor System for Chemical Processing

e. Inventions/Patent Applications, licensing agreements

Provisional Patent Application filed by Stevens and FMC on April 18, 2005
Non-Provisional Patent Application filed by Stevens and FMC on April 18, 2006, but abandoned in September 2008.

f. Other products – *Not Applicable*